Single-cell microfluidic separation and analytical platforms based on biophysical phenotypes

---

A Dissertation

Presented to

The Faculty of the School of Engineering and Applied Science

University of Virginia

In Partial Fulfillment

of the Requirements for the Degree

Doctor of Philosophy

By

Karina Torres Castro

March 2022

APPROVAL SHEET

This

Dissertation

is submitted in partial fulfillment of the requirements for the degree of

Doctor of Philosophy

Author: Karina Torres Castro

This Dissertation has been read and approved by the examination committee:

Advisor: Nathan S. Swami

Chair: Keith A. Williams

Committee Member: James P. Landers

Committee Member: Blanca H. Lapizco-Encinas

Committee Member: Rebecca R. Pompano

Accepted for the School of Engineering and Applied Science

Jennifer L. West, School of Engineering and Applied Science

March 2022

Acknowledgement

My gratitude to my advisor Dr. Nathan S. Swami. Thank you for the opportunity you gave me by accepting me in your group. Thanks for your support, comments and guidance through my journey as PhD student.

Thanks to all my lab mates and colleagues for the great discussions, collaborations and teamwork you have put along these years. I always say that the biggest perk of the Swami's Lab is being part of an amazing group of students that are transparent and willing to work together to achieve our goals. It has been always nice to go out for lunch or dinner with you and talk about many different topics. There has been many great students and postdocs I have overlapped with during my time in this program from whom I have learned a lot. I am sure I will miss some names and I want to apologize in advance for that.

Special thanks to John Moore, Armita Salahi, Vahid Farmehini, Jack Huang, Aditya Rane, Javad Jarmoshti and Carlos Honrado, John McGrath, Walter Varhue, Yi Liu, Rasin Ahmed, Naimish Sardesai and Renny Fernandez.

Thanks to Jun-Han Han, Trey West and Professor Mircea Stan for including me in their 3D micro-cooling exploration project. I had a lot of fun working with your heat exchange application.

Thanks to all the wonderful ECE graduate student council members: Vaibhav Verma, Vinay Iyer and Sadik Toriqul Islam.

To the Peirce-Cottler's lab, Guler's lab and Li's Lab for providing me with valuable samples and for their collaborations.

To my committee members: Keith A. Williams, James P. Landers, Blanca H. Lapizco-Encinas and Rebecca R. Pompano for their questions and comments that helped polishing my work and for their exchanges during this dissertation defense.

Finally, I want to extent my appreciation to my dear friends Esther and Bill that have been an amazing support all these years in Charlottesville, to Tannaz Farrahi for being a fantastic friend of many battles, to Patricia and Carlos that I will be always grateful with, to Sandra and Stephen Cauffman's family for receiving me with open arms and great advice, to Caitlin D. Wylie for being a wonderful mentor, to Paula and Miguel for all the interesting chats and friendship, and so many others that I've had the privilege to meet over these years. To my family, thank you for all your support and kind words that have lifted me in moments of despair. Thanks to the universe for showing me different paths and for all the opportunities of growth that has given me in this endless *"Solve Et Coagula"* journey.

Dedication

For Paola and my parents

The people I admire the most and look up to. You are my constant source of inspiration

Table of Contents

Abstract

The complex functional and structural organization of biosystems leads to a degree of heterogeneity of cellular phenotypes. To parse through this heterogeneity, there is the need for platforms for separation and analysis, with single-cell sensitivity, to associate biological function and disease with particular cellular markers. The current state-of-the-art method for this purpose is based on single-cell analysis by flow cytometry, after fluorescent staining for their characteristic cell surface proteins, which is then used to identify and separate cells based on biochemical characteristics. However, there is an increasing recognition that biological processes, such as prediction of cancer metastasis, stem cell differentiation lineage or different immune cells activation levels that cannot be linked solely to biochemical traits. Hence, there is emerging interest in identifying cells, cellular aggregates and subcellular bodies based on biophysical properties for separation and quantification. These biophysical properties can include cell size distribution, shape, deformability and electrophysiology-based characteristics.

Biomechanical metrics, such as deformability of cells and cellular aggregates, caused by microfluidic constrictions or post structures can allow for stratification of biosystems based on cell size, rigidity and its extracellular matrix properties. Devices for separation and analysis using biomechanical metrics were developed for two distinct applications. The first focused on monitoring biophysical heterogeneity of the integration of pancreatic islets with adipose-derived stems cells (ADSCs), which alters basement membrane and angiogenic factors in the islet, which are important for its transplantation to treat diabetic conditions. Given the heterogeneity in size, shape and extracellular matrix of human islets, we seek to determine if biomechanical metrics of single-islets can be used as a marker to indicate completion of their integration with ADSCs. The second application focused on microfluidic deterministic lateral displacement (DLD) for size-selective separation of macrophages to enrich the activated fraction from heterogeneous samples. This can be used to measure the immunomodulation conditions during macrophage interactions with tissues to reduce inflammations.

Electrophysiology can serve as a subcellular marker to stratify and separate cells by dielectrophoresis (DEP), based on membrane capacitance or interior conductivity characteristics. We seek to integrate on-chip sample preparation and phenotypic assessment functionalities on

DEP separation platforms. Specifically, to reduce cumbersome off-chip operations, we propose to integrate the capability for on-chip swapping of cells from culture media to a low conductivity buffer prior to DEP manipulation, and then back to the culture media following DEP separation. This will be demonstrated using red blood cells.

Chapter 1: Background

1.1 Microfluidics

Fluid mechanics at the micro scale or microfluidics presents opportunities for a myriad of applications, including biomedical devices that measure, characterize and separate different types of bio-particles for further biological studies or for quantification purposes.

The scale of microfluidic applications implies that phenomena, such as, surface tension and viscosity that are usually negligible in macroscale systems in comparison with the flow inertia become important at micro scale (100 μm or less). Scaling laws express the variation of physical quantities with size of the system, while keeping properties such as pressure and temperature constant. The relationship between surface forces and volume forces depends on of the scale of the problem we are aiming to solve. This relationship is expressed: [3]

$$\frac{surface\ forces}{volume\ forces} \propto \frac{l^2}{l^3} = l^3 = \frac{1}{l} \underset{l \to 0}{\longrightarrow} \infty \tag{1}$$

and fluid behavior is modeled by the Navier-Stokes equation:

$$\rho[\partial_t v + (v \cdot \nabla)v] = -\nabla p + n\nabla^2 v + \rho g + \rho_{e1} E_1 \tag{2}$$

Different assumptions are made based on which forces are more significant in the proposed system. From the above relation it is clear that viscous forces dominate as the system becomes smaller. Hence, surface tension and fluid viscosity are the forces that dictate how the system behaves under such circumstances, and inertial forces are negligible in comparison with surface forces, causing a laminar flow regime.

1.2 Laminar Flow regime

In fluid mechanics, there are different flow regimes that encompass different system properties and assumptions. The flow regimes are laminar flow, transitional flow and turbulent flow. These regimes are determined by the Reynolds (Re) number, which is a dimensionless number that compares the two main flow properties of the system; system inertia and viscous forces. When the Re number is small, it means the flow viscosity overcomes the flow inertia and this is known as a laminar flow regime, conversely when the Re number is large this means the flow inertia overwhelms the viscosity of the flow, thus the flow movements are more chaotic and harder to predict, this regime is known as turbulent flow. Intermediate Re numbers are known as the transition regime, wherein the system present characteristics of both laminar and turbulent flow regimes.

For this thesis and the applications that are studied here, we are going to be working only in laminar flow regime since due to the scale of our devices, the flow inertia does not overcome the flow viscosity and the Re numbers are small in magnitude compared to transitional regimes and turbulent flow. For Re<<1 the Stokes equation assumes a new form known as the Poisson equation:

$$-\frac{\partial p^*}{\partial x_i^*} + \frac{\partial^2}{\partial x_j^{*2}} = 0 \tag{3}$$

Equation (3) is more straightforward to solve. If the pressure gradient is increased by a constant then the velocity at every point in the flow is multiplied by that same constant. The flow streamlines do not change therefore, an experiment at low Reynolds numbers can be used to predict all low Re flow behaviors of the system and more importantly, time is eliminated from the equation, thus at low Re numbers the flow is reversible. This property is very useful to predict the motion of particles in the system. [4]

1.3 Inertial microfluidics

Inertial microfluidic methods have been growing due their high sample throughput and clever designs that allow exploiting some inertial effects in microfluidics.

These methods are still under the laminar flow regime, but the conditions of the experiments are done at much higher flow velocities that can achieve a characteristic Re number value of the order of 100 even in microscale systems such as the pertaining lab on a chip devices studied here.[5]

This translates into laminar flow conditions that exhibit some inertial flow forces, which are normally negligible in other microfluidic applications. Here, the Re numbers are closer or much less than 1, as it was mentioned previously, all the flow inertial forces are negligible at conditions in which the $Re<<1$ and this type of flows are known as creeping flows. [6]

In inertial microfluidics the Re number is much higher that typical laminar flow applications in microfluidics, but it is still far from entering a transition flow regime due to the scale of the phenomena (microns) in which the flow is traveling.

The fact that the flow inside the microchannel is traveling at such high velocities doesn't change the laminar flow nature of the flow but lift forces, such as flow shear induced force and wall induced forces become more significant, when they were previously neglected at lower volumetric flows (lower velocities). These forces affect particles since they need to balance these forces in equilibrium positions that can be exploited to sort, enrich and separate particles. [7] Therefore, inertial microfluidics is a branch of its own in microfluidics. Besides being attractive due to their high throughput, inertial microfluidics has another important characteristic, which is being a passive method. There is no need to apply any external forces such as electric fields or acoustics to separate the particles as they separate due to the inertial flow effect.

1.4 Deterministic lateral displacement (DLD)

DLD is a size and deformability-based continuous particle separation method that enables high sample throughput due to its post array extension and deterministic design that allows for passive separation of particles based on the diameter cut-off or critical diameter Dc for which the microstructures are designed.[8]

A set or period of aligned posts that are carefully designed to follow a specific angle separates the flow streamlines and the particles that travel in the flow. The particle hit the posts that are designed with a Dc and spacing for deflecting all the particles that are higher than the Dc, these particles will enter a bump mode or displacement mode in which they will bounce to the next row of posts that is shifted in α angle, so they will continue to displace diagonally across the post array period. The particles that are smaller than the Dc will continue following the flow streamlines surrounding or hugging the posts walls in what is known as the zigzag mode towards the device outlet.[9]

The particles with a diameter larger than Dc will displace a predetermined distance in the x component of the diagonal displacement (hypotenuse) in one array period. Thus, to have a significant displacement on the device that accounts for all the possible starting positions of the particles, it is necessary to calculate the number of periods or post arrays that are needed to achieve a complete separation of the particles according to the designed Dc. [10]

1.5 Computational Fluid Dynamics (CFD)

The analysis of systems involving fluid flow, heat transfer or other associated phenomena by performing computer-based simulations is known as computational fluid dynamics. This powerful technique allows predicting fluid flow conditions in multitude of systems by solving the partial differential (PDEs) equations that govern flows in Cartesian coordinates or other frames of reference. CFD programs use numerical algorithms using grids or meshes known as finite elements

that solve PDEs like Newtonian models for viscous stresses that leads to the stokes equation (2) or other sets of equations that are playing a role in the physics of the problem such as the thermodynamic equations of state or transport phenomena equations.

To build CFD simulations, it is necessary to establish not only a set of equations or physics for the problem in a determined geometry of interest, but it is also necessary to establish correct boundary conditions for the problem so it makes physical sense. For fluid flow in specific, the governing equations represent mathematical statements of the laws of conservation in physics which are the following:

- The mass of fluid is conserved
- The rate of change of momentum equals the sum of the forces on a fluid particle (Newton's second law)
- The rate of change of energy is equal to the sum of the rate of heat addition to and the rate of work done on a fluid particle (First law of thermodynamics)
- The fluid is assumed to be a continuum, this means that the molecular structure of the fluid and the molecular motion of its components its ignored, the fluid is seen as a bulk. [11]

This powerful tool applied in a problem that is properly defined gives accurate results with the flexibility of testing many different conditions to predict possible outcomes for experiments and allows optimizing designs and conditions prior running a real-life experiment.

Depending on of the complexity of the problem, geometries, conditions, physics involved, etc. a lot of computational power can be consumed to solve PDEs in each element of the mesh, thus translating this complexity into a need for larger hardware capacity and computational time that can take many hours (days) to converge into a solution.

A very useful analogy to microfluidic networks is the electric circuit analogy, in which the fluid

flow is seen as the current in a circuit and the pressure drop as electric potential difference or voltage. In electric circuits, the Ohm's law states that the electric current is proportional to voltage and inversely proportional to resistance, the fluid flow analogous to the Ohm's law is the Hagen-Poiseuille law.

1.6 Hagen-Poiseuille Law

The Hagen-Poiseuille Law equation shown below, states that the pressure drop in a microfluidic circuit is proportional to the volumetric flow (Q) and inversely proportional to the hydraulic resistance (R_{hyd}).

$$\Delta p = \frac{8\mu L Q}{\pi R_{hyd}^4} \tag{4}$$

The R_{hyd} depends on the microchannel geometry since it's a relation between the channel crossectional area and the wetted perimeter.

This analogy simplifies greatly the microfluidic devices design, especially when there are several branches and helps to quickly visualize how the flow will behave if there are several channels in series or in parallel following the same rules for adding resistances in series and in parallel in electric circuits.

Even though this simplified approach is a powerful tool to start designing a microfluidic device, it is important to note the system to design must comply with the following assumptions:

- The fluid is non-compressible
- The flow is laminar
- The flow travels through the channel with a constant velocity profile

- There is no heat transfer or diffusion phenomena happening
- There is some error when it is used with non-circular crossectional area channels

The Hagen-Poiseuille's equation assumes that the flow travels with a constant velocity profile (like current on a wire) instead of the characteristic parabolic profile a laminar flow, induce error when other processes are taking place in the microfluidic channel e.g., diffusion of chemical species or heat transfer through the fluid layers. [4]

In conclusion, the Hagen-Poiseuille analogy is very useful for designing microfluidic circuits to predict the flow behavior and establish hydraulic resistances comparisons as long as there are no other forces such as the mentioned above in the channels, at different channel geometries the error can be up to 20% according to empirical relations established in literature for different channel geometries. For more complex systems, where other physical phenomena are taking place or to obtain more accurate results CFD methods are the most reliable source to predict fluidic behavior in microchannels.

1.7 Microfabrication

The miniaturization of electronic devices known as microelectronics and Moore's law scaling for microelectronics sped up the creation and improvement of microfabrication tools that not only have continuously pushed the boundaries of Moore's Law since the late 90s by doubling down the integration density every 18 months in the semiconductors' industry, but it has also enabled the development of microfluidics for biomedical applications, allowing the fabrication of micro molds using different types of photo resists, specially SU-8 due to its variety of aspect ratios, mechanical properties and diverse thicknesses. Micromolds are used in what is known as soft lithography in which the negatives are obtained using bio-compatible materials such as PDMS that are enclosed

to get microscale channels with different geometries for running microfluidics experiments. [12]

1.8 Lab on a Chip and Micro-total analysis systems

Lab on chip (LOC) is defined as all the technologies that involves some type of fabricated structure to perform different types of experiment at the micro or nano scale. These systems can be chemical reactions, biological or physical processes that can be coupled with microfluidics for studying, analyzing or manipulating different conditions or even biological samples. Since this is a very broad concept, lately it has been preferred to use the term micro total analysis systems or μTAS since these systems can be comprised by a myriad different physics for diverse applications. [12]

In the present work our main focus are μTAS specifically applied for analyzing, sorting or separating biological entities such as single cells and cells aggregates. As it has been mentioned before μTAS or LOC platforms have been increasingly used for biomedical research and life sciences as important tools to asses and study biological samples outside humans' body with the advantage of having to require a small volume of sample for point of care applications. The size of these systems makes them attractive due to their portability a potential for in-situ diagnostics. [13]

1.9 Particle Electrokinetics

1.9.1 Dielectrophoresis (DEP)

The term dielectrophoresis (DEP) refers to the movement of particles due to their dielectric properties in a non-uniform AC field. The most common example is a spherical particle, of high conductivity and low permittivity, located between two electrodes and suspended in a low conductivity and high permittivity electrolyte. Starting with a uniform AC field, if the permittivity of the particle is greater than the permittivity of the medium, it means there are more charges

within the interface than outside of the particle, resulting in a difference of charge density on either side of the particle. An induced net dipole across the particle, following the applied field direction, is thus generated. Conversely, if the particle permittivity is less than the medium permittivity, more charges are accumulated on the interface outside and the induced net dipole is now contrary to the field direction. [1]

When a non-uniform AC field is applied, the density of electrical field lines is unbalanced between the poles, meaning that the forces on the induced dipole will also be unbalanced, resulting in particle movement. When the particle permittivity is greater than the medium the dipole is oriented with the field, and the particle moves towards the high field point, this displacement of the particle towards the high field point is known as positive DEP or pDEP and when the particle is oriented against the field, the particle displaces away from the high field points, this displacement is known as negative DEP or nDEP. [2]. DEP forces are currently used to separate different types of particles and as deflecting mechanism under continuous flow conditions [14] [15]

1.10 Mechanical strength measurements of biological tissues

By definition, mechanical strength is a physical condition that a biological tissue must meet to withstand a specified force. In this work, we are looking to define a relative experimental pressure condition in which pancreatic islets or islets of Langerhans can withstand before deforming through a constriction in a microfluidic channel. Thus, establishing the islet stiffness between different samples to classify them according to their relative stiffness level as a means to correlate their stiffness level to literature that predict their engraftment potential. For instance, it has been reported the use on deformation pressure as a possible characterization method for healthy RBCs and RBCs infected with malaria [16]

11.1 Biological samples

1.11.1 Human Pancreatic islets (h-islets)

Human pancreatic islets (h-islets) transplantation is an experimental therapeutic treatment for diabetes type 1 patients. This process consists on extracting the pancreatic islets or cell aggregates from the pancreas of a postmortem donor. These cell aggregates contain a different type of cells, including alpha cells that produce glucagon, beta cells that secrete insulin, the hormone responsible for controlling sugar levels in blood and other cells that secrete other important body regulating hormones.

The extraction of h-islets or h-islet isolation is not efficient, and many valuable islets are lost in the process. After the isolation process, the h-islets need to regain their structure in a culture process that takes approximately 6 days, before being suitable for transplantation into a patient. Therefore, the proposed method is to assess h-islet stiffness by applying pressure in a micro channel designed to deform the islets once their reach their deformability threshold, by using a relative pressure measurement we call bypass pressure. [17]

1.11.2 Adipose Derived Stem Cells (ADSC)

ADSC possess the ability to create new blood vessels and anti-inflammatory properties that are desirable for tissue engraftment in patients. It has been reported that when ADSC are co-cultured with h-islets it increases h-islet engraftment potential in patients. Currently there are ongoing efforts to understand how ADSC promotes implantation and graft survival by characterizing the co-cultured tissue and their engraftment site conditions.[18]. We hypothesize that the co-culturing

of h-islets with ADSC assist in h-islets recovery process thereby producing changes on the h-islet morphology and/or stiffness properties that can be measurable by microfluidic means.

1.11.3 Red Blood Cells (RBC)

Biological samples like liquid biopsies (e.g., blood samples), cell cultures or biological particle suspensions are constituted by heterogeneous cell populations that makes samples more difficult to analyze and study due to the many interactions that these different groups of cells have. Therefore, having pure samples constituted by one type of cell is important for studying a specific cell line to diagnose and develop further treatments that target specific cell types. To start designing systems for separating heterogeneous particles is necessary to first have model particles that be easily compared to real-life experiments. Thus, is common to start with simpler cell systems such as red blood cells (RBC) that are readily available and are well characterized systems that can be easily benchmarked with CFD simulations since their physical and electrical properties have been reported extensively in literature [14].

1.11.4 Macrophages

Macrophages play an important role in tissue homeostasis, inflammation, and host defense. They secrete pattern recognition receptors that sense microbial danger and they promote immune responses to protect the host organism. The interaction between cellular metabolism and macrophage immunity is not limited to answering the energy demands of cells. There is evidence that in response to bacterial sensing, macrophages undergo metabolic adaptations that contribute to the induction of immunity signaling and/or macrophage polarization. Therefore, understanding macrophages response mechanisms to microbial danger is of great interest for the biology

community. The use of strong agents such as lipopolysaccharide (LPS) that activates the macrophages immune response is currently used as a tool to understand such mechanisms.[19]

Chapter 2: Device platforms for isolation and analysis based on biomechanical phenotypes

2.1.1 Introduction

Phenotypic heterogeneity is inherent to cellular systems [20], due to temporal fluctuations in the levels of regulatory proteins, position in the cell cycle and the activation of cell death mechanisms. In this manner, small variations in the proportion of subpopulations [21, 22], can have system-level effects on diseases, tissue regeneration and treatment response. Quantifying the emerging phenotypic heterogeneity of cellular systems and enriching for particular subpopulations are essential steps towards understanding the biosystem and for optimization of therapies. This is usually accomplished by flow cytometry for quantifying the heterogeneity and by fluorescence-activated cell sorting (FACS) of live cells for enrichment of particular populations, but these tools require cell-type specific surface markers, which do not exist or are unreliable for novel pathogenic microbials and certain cancer and stem cells. Specifically, since stem cell transplants cannot be labeled before therapeutic use, their heterogeneity leads to the inability to predict differentiation and fate potential at single-cell sensitivity and to enrich specific subpopulations for controlling the cellular composition of transplants.

Phenotypic analysis to classify cellular populations currently relies on averaged measures, based on metabolite secretion, protein expression or a nucleic acid analysis. These averaged measurements limit the ability to quantify heterogeneity and isolate subpopulations of interest [23]. Cellular biophysical properties, due to biomechanical characteristics that include size, shape and deformability; or electrical characteristics that include electrical size and dielectric polarizability due to membrane capacitance and cytoplasmic conductivity can be used to classify cellular phenotypes in a label-free manner. In this dissertation, we seek to develop microfluidic platforms

that utilize such biophysical properties to separate and analyze for cellular phenotypes of relevance to regeneration and disease therapies.

2.1.2 Device platforms for isolation and analysis based on biomechanical phenotypes

Biomechanical metrics, such deformability of cells and cellular aggregates, caused by microfluidic constrictions or post structures can allow for stratification of biosystems based on cell size, rigidity and its extracellular matrix properties. Devices for separation and analysis using biomechanical metrics will be developed for two distinct applications. The first will focus on monitoring biophysical heterogeneity due to the integration of pancreatic islets with adipose-derived stem cells (ADSC), which alters basement membrane and angiogenic factors in the islet. These alterations are essential to the function of human islets (h-islet) after transplantation. Given the heterogeneity in size, shape and extracellular matrix of h-islets, we seek to develop biomechanical metrics of single-islets for enabling use as a marker to indicate completion of their integration with ADSCs. Separately, in the field of bone regeneration, synthetic bone graft substitutes that are fortified with osteo-inductive progenitor stem cells are emerging as a promising therapy, since they provide the three necessary factors for bone regeneration – mechanical strength, osteo-conductivity and osteo-inductivity. Specifically, adipose derived stem cells (ADSCs) are gaining tremendous attention, since they can be isolated easily, in abundant numbers, using simple and relatively less invasive procedures in comparison to clonal mesenchymal stem cells (clonal MSCs) derived from the bone marrow. However, progress on their utilization for bone regeneration is limited by an incomplete understanding of their heterogeneity and the role that each ADSC subpopulation of varying phenotype plays on their bone forming ability. Consequently, current research with mixed ADSCs possessing a wide size range (10-25 μm for mouse-derived cells) [24] and intracellular granularity have yielded contradictory results on their bone forming ability. Hence, we seek to develop

microfluidic means for size and deformability-based separation of ADSC phenotypes for stratification of their differentiation behavior.

2.2 Quantifying heterogeneity in reorganization of human islets during co-culture with adipose-derived stem cells to enhance vascularization

T1 diabetes (T1D) is a debilitating autoimmune disease that is currently treated by insulin therapies, but these do not offer the fine control needed for regulating the endocrine response and they neglect the multiple functions served by the pancreas. Transplantation of human islets of Langerhans (h-islets) is emerging as a potential therapy [20-22]. However, limitations in donor numbers and variability in quality of islets have led to poor engraftment outcomes, including inadequate revascularization [23,24] and adverse immune responses [25-26] that increase transplant costs. Improved *in vitro* processing to increase the number of functional islets can promote their vascularization and insulin secretion outcomes *in vivo* [27].

The co-transplantation of harvested islets with stem cells [28] or their *in vitro* co-culture prior to transplantation [29,30] is being explored to promote re-growth of the islet basement membrane and enable expression of angiogenic factors to enhance vascularization [31], for improving the functional quality and reducing the variability of the graft. Specifically, islet co-transplantation with mesenchymal stem cells [32] and adipose derived stem cells (ADSCs) [33] promotes islet survival and insulin function of the graft in mice, while reducing the number of islets needed for diabetes reversal, by making the islets more likely to remain viable and vascularize *in vivo* after transplantation [34,35]. Such methods would also reduce the need to harvest islets from multiple organ donors, thereby reducing immune rejection. However, there are no metrics for monitoring the biophysical reorganization on a single-islet basis, which is required due to heterogeneity in islet size, shape and functional outcomes [36]. Such metrics would allow for rapid identification

and separation of functional islets, thereby standardizing assessment of their quality and enabling scale-up of transplant numbers.

Following harvest from the donor pancreas, islets are placed in culture media to allow for morphology change or "plumping" [37], which is characterized by gradual recovery of their rigidity over several days due to *in vitro* remodeling of their basement membrane [38, 40], that promotes their vascularization ability after transplantation [41]. The associated alterations in biomechanical properties of islets correlate with their vascularization potential [42], insulin expression [43] and inflammatory responses [44], post-transplantation. Microfluidic techniques [45] with feature sizes in the range of single cells and multi-cell aggregates, use tangential flows and microscale constrictions to controllably deform biological objects and measure their biomechanical properties. In recent years, several high throughput microfluidic techniques for measuring deformability differences between individual cells have been developed [46,47], wherein pressure driven flow across constricting structures is used to induce particle deformation, as measured by particle transit time, threshold bypass pressure [48], induced hydrodynamic or electrical resistance [49], and particle shape alterations under shear flow [50]. However, multi-cell aggregates are spread over a far broader range of size and shape distributions than individual cells, which poses measurement challenges. Furthermore, the high-pressure differentials usually used for deformability-based cell separation can damage multi-cell aggregates [51] due to the lower yield strength of their intercellular regions versus that of the component cells [52], highlighting the need for alternate analytical methods.

In this work, we seek to develop metrics to monitor the biophysical reorganization dynamics of the multi-cell h-islet ADSC aggregate during co-culture, by comparing on a single aggregate basis, the biomechanical metric determined by microfluidic deformation (**Fig. 2.1 A)** versus from

microscopic observations (**Fig. 2.1 C**). While imaging methods suggest the occurrence of reorganization within each aggregate during the co-culture, they are unable to quantify the alterations in absence of 3D visualization abilities and their measurement throughput is not sufficient for dynamic monitoring. Hence, microfluidic deformability measurements to compute biomechanical opacity of single islets can provide a quantitative and high throughput metric, which can be used together with microscopy and endpoint immunoassays (**Fig. 2.1 B**) of angiogenic and basement membrane factors, to provide multi-modal information on islet basement membrane reorganization dynamics over the co-culture period. Based on bypass pressure measurements on aggregates through microfluidic constrictions (**Fig 2.1 A1-A2**), the biomechanical opacity metric can delineate the completion time for subpopulations with remodeled islet basement membrane characteristics during co-culture. This biophysical metric can eventually be used to quantify and separate the fraction of islets that have reorganized their basement membranes after co-culture with stem cells.

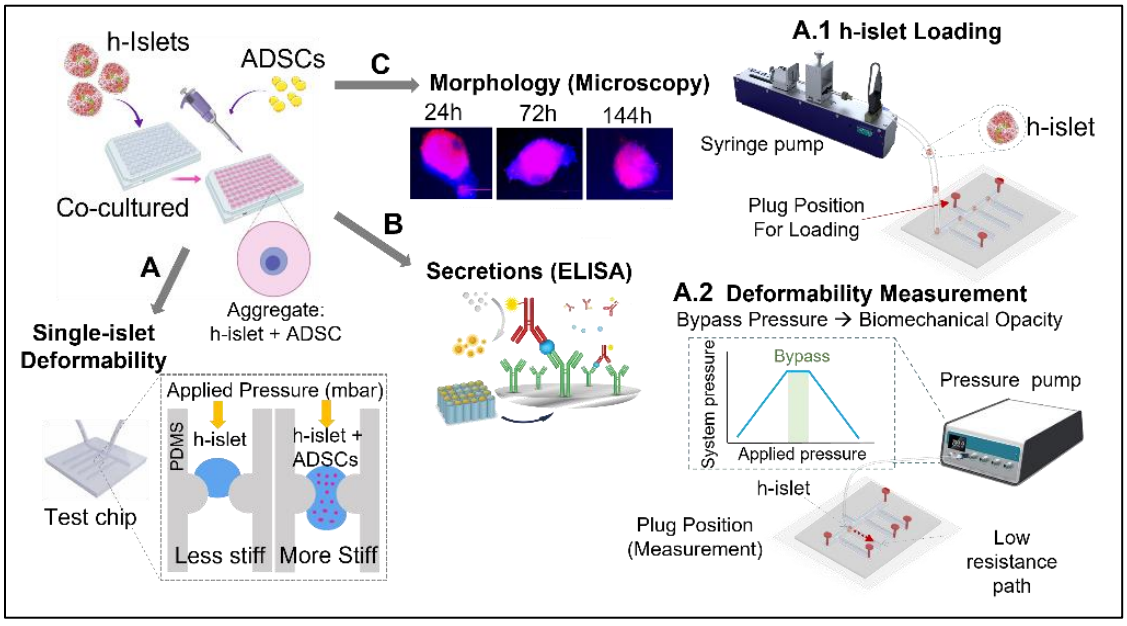

Figure 2.1 Aggregates of h-islets co-cultured with ADSCs are analysed by: **A**. Single islet deformability on microfluidic chip. **B.** Secretions of angiogenic and basement membrane

factors by ELISA. **C.** Fluorescence microscopy to image morphology alterations over culture time. Overview of deformability measurement: **A.1**: h-islets are loaded in the chip. **A.2:** Bypass pressure measurement through 80 μm constriction.

2.3 Experimental Methods

2.3.1 Co-culture of human islets with ADSCs

Adipose-derived stem cells (ADSCs) were expanded at ~5000 cells/cm^2 (Corning; Corning, NY) using Rooster Nourish-MSC medium (RoosterBio; Frederick, MD) until they reached 70% confluency. Cells from passage numbers 3-5 were dissociated and lifted using Accutase (ThermoFisher; Waltham, MA) and used for the experiment. Human pancreatic islets were placed individually in 50 μL human islet medium (CMRL 1066 without phenol red, L-glutamine; Corning; Corning, NY) in ultra-low attachment round bottom 96-well plates (Corning; Corning, NY). ADSCs were suspended in human islet medium at 20k/ml density, and 200 μL of the ADSC suspension was added to each well. ADSCs gradually attached to the outer surface of the islets, and the co-cultures were maintained under standard incubator conditions (5% CO2, 37°C). At different time points over six days (24, 48, 72, 96, 120, and 144 hours), the islets and attached ADSCs were collected for analysis. Control cultures of islets in the absence of ADSCs, as well as ADSCs in the absence of islets were also maintained under the same culture conditions for the duration of the experiment.

2.3.2 Basement Membrane and Angiogenesis Analysis

Conditioned media from co-cultured ADSCs and islets was collected for the analysis of basement membrane and angiogenic factors after 144 hours to compare versus media from ADSCs cultured without islets and from islets cultured without ADSCs as controls. These factors were quantified

using the Proteome Profiler Human Angiogenesis Array Kit (R&D Systems; Minneapolis, MN).

2.3.3 Fabrication of microfluidic device

The microfluidic device (**Fig. 2.1 A**) was fabricated by photolithography of the master (EVG 620 mask aligner), using a photo mask (PhotoSciences) and a negative photoresist (SU-8 2150, MicroChem) for pattern definition. Micro-molding with PDMS or polydimethylsiloxane (Sylgard 184, Dow Corning) was performed using uncured elastomer base to curing agent in the 5:1 ratio and crosslinking at 60 C for 8h to obtain microchannels of 500 μm depth with 80 μm constrictions. After curing, the PDMS chip was released from the master; the PDMS features were diced, and the inlets and outlets were drilled with a biopsy punch. The chip was bonded to a glass cover slip after oxygen plasma treatment (PDC-001 Harrick Plasma cleaner).

2.3.4 Bypass pressure measurements of single-islets

For bypass pressure measurements **(Fig 2.1. A1-A2),** a syringe pump (neMESYS 290N, Cetoni GmbH) was used to load single h-islets into the microfluidic chip and a pressure controller (Fluigent MFCS-EZ) was used to adjust the applied pressure in the channel to pass h-islet through 80 μm constrictions.

2.3.5 Imaging of h-islets for shape and area quantification

A series of videos were taken on each measured h-islet before, during and after passage through the microfluidic constriction, using a CMOS Orca-Flash 4.LT digital camera (Hamamatsu) coupled with a Carl Zeiss inverted microscope (Axio Observer Z.1). Image processing to determine the h-islet particle area measurements were done using the Fiji software from the

National Institute of Health (NIH).

2.3.6 Fluorescence microscopy of h-islet aggregates

Fluorescence images of single aggregates of h-islets after co-culture with ADSCs in well plates were measured using a EVOS FL cell imaging microscope (ThermoFisher Scientific), under a magnification of 20x, using DiI (1,1'-Dioctadecyl- 3,3,3',3'-Tetramethylindocarbocyanine Perchlorate) (Invitrogen), which is lipophilic stain that is specific to ADSCs, and Hoechst 33342 (Bisbenzimide) (ThermoFisher) fluorescent stain that is specific to the h-islet membrane.

2.3.7 Data processing and statistical analysis

One-way ANOVA with Tukey's multiple comparison tests and t-tests with Welch's correction were applied to compare differences between time points and on unpaired samples using GraphPad Prism. A custom-made MATLAB (R2017a) script was used to perform a principal component analysis (PCA) for calculating the 95% confidence ellipses from the obtained data. The covariance matrix was calculated to extract the eigenvectors (principal components) [53] to plot the h-islet area versus bypass pressure under control and ADSC co-culture conditions into confidence ellipses. The largest spread of the data (first principal component) corresponds to the major axis, and the minor axis is the perpendicular component (second principal component) with the second highest variance [54]. The bypass pressure was normalized based on area of the aggregate to compute biomechanical opacity values that were used to visualize the deformability response trends of the h-islets co-cultured with ADSC, in comparison with h-islet controls.

2.4 Results and discussion

2.4.1 Shape-based monitoring of aggregate reorganization

The reorganization dynamics of single h-islet aggregates (h-islet plus ADSCs) was monitored over the co-culture period by fluorescence imaging to assess the integration of ADSCs (pink) with the h-islets (purple), as well as by bright field imaging to follow the shape alterations. From the representative fluorescence images (**Fig. 2.2 A**), while ADSC regions merge with the islet tissue, right from the 24 h data point, the shape evolution towards a spherical morphology occurs more gradually over the 6-day co-culture period.

Based on bright field images of 42 multicell aggregates at each timepoint (24 h, 48 h and 72 h), the co-cultured h-islet plus ADSC aggregates were classified to determine proportions within three distinct morphologies: spherical, tail, and irregular shapes (**Fig. 2.2 B**). While a majority of the co-cultured aggregates exhibit tail morphologies at the 24 h time point, the predominant morphology at the 48 h timepoint is irregular and the aggregates become spherical onwards from the 72 h timepoint. The shape reorganization does not show a dependence on the aggregate size, based on imaging studies (the rows of **Fig. 2.2 A**). Since merging of the ADSC and islet tissue is apparent right from the 24 h co-culture timepoint **(Fig. 2.2 A)**, we use the total area of the multi-cell aggregate for all subsequent normalization within biomechanical studies on co-cultured h-islets.

2.4.2 Biomechanical opacity indicates size-dependence in h-islet reorganization

The biomechanical alterations of h-islets due to basement membrane remodeling during co-culture with ADSCs were quantified based on the bypass pressure level for passage of individual aggregates (h-islet integrated with ADSCs) through 80 μm constrictions (**Fig. 2.1 A1**-**A2**). The plots of bypass pressure for each aggregate versus its measured area (from bright field images) are in **Fig. 2.2 A** (24 h co-culture) and **Fig. 2.2 B** (72 h co-culture). Respective plots are also shown for the control h-islets that were maintained without ADSCs in the same media for the timepoints.

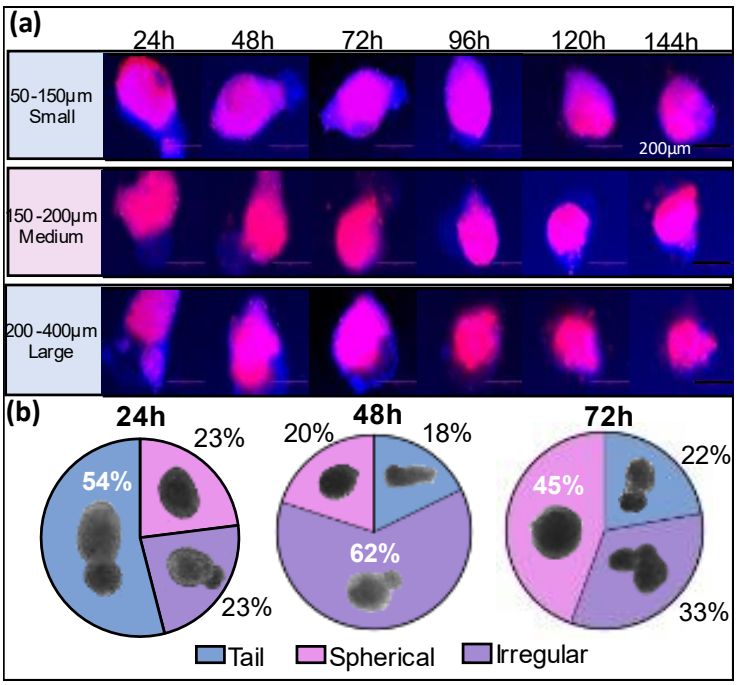

Figure 2.2 Integration and reorganization of h-islets after co-culture with ADSCs. **A.** Representative fluorescence images over 6 days of co-culture; **B.** Brightfield images to quantify shape distributions of 42 islets per culture condition.

The plots include confidence ellipses for the cases of 1σ and 2σ in data spread (σ is standard deviation). Based on this, while the spread in data for "control" islets is not altered after 24 h of co-culture with ADSCs, this spread is significantly lowered after 72 h of co-culture with ADSCs, likely since aggregate reorganization over this co-culture period leads to tightening of their size and stiffness property distributions. Hence, a greater proportion of aggregates has likely reorganized at the 72 h versus the 24 h co-culture timepoint. However, since slope of the data points (major axis of the ellipse) suggests a degree of heterogeneity in reorganization time for each aggregate, we seek to assess the phenotype that can possibly determine the reorganization dynamics of each aggregate. The bypass pressure level for "control" h-islets increases with their area (i.e., positive slope), as expected from volumetric scaling of flow around the aggregate exterior. The trend is similar for h-islet aggregates after ADSC co-culture at the 24 h timepoint, with only a minor slope reduction. However, the bypass pressure becomes invariant with aggregate

area at the 72 h timepoint, as apparent from the near-zero slope. Size-dependent alterations in h-islet reorganization time during the co-culture with ADSCs can possibly explain this slope alteration. If h-islet aggregates below a threshold size reorganize more effectively over the 72 h co-culture period versus those above a threshold size level, and assuming completion of reorganization leads to higher biomechanical stiffness, then the bypass pressure values would be enhanced for the smaller-sized subpopulation versus the larger-sized subpopulation. This size-based heterogeneity in reorganization is not an issue with control h-islets or with 24-h co-cultured h-islet aggregates that have undergone only minimal reorganization, thereby exhibiting a steady rise in bypass pressure with aggregate area. However, size-based heterogeneity in reorganization of co-cultured h-islet aggregates likely sets in at the 48 h (**Appendix: A.1**) and 72 h timepoints, since a subpopulation above a threshold size has not reorganized, thereby leading to an invariant slope of the bypass pressure versus aggregate area plot. The caveat is that there may be size alterations of h-islet aggregates during the reorganization over the co-culture period, which would also alter their bypass pressure. Hence, an ANOVA test was performed to correlate the bypass pressure with the size distribution of the h-islet aggregate, so that we can identify outliers and correlate the two variables (area and bypass pressure). The statistical significance plots over the co-culture time for bypass pressure (**Fig. 2.3 C**) and area of the aggregates (**Fig. 2.3 D**) show that a consideration based solely on exterior size changes over the 24 h to 72 h ADSC co-culture period is not sufficient to explain the large bypass pressure alterations that were observed. For instance, while the bypass pressure alterations between co-cultured aggregates at the 24 h versus 72 h periods show a high degree of statistical significance (green stars in **Fig. 2.3 C**), size alterations for the respective samples show a lower degree of statistical significance ("not significant" or NS in **Fig. 2.3 D**)

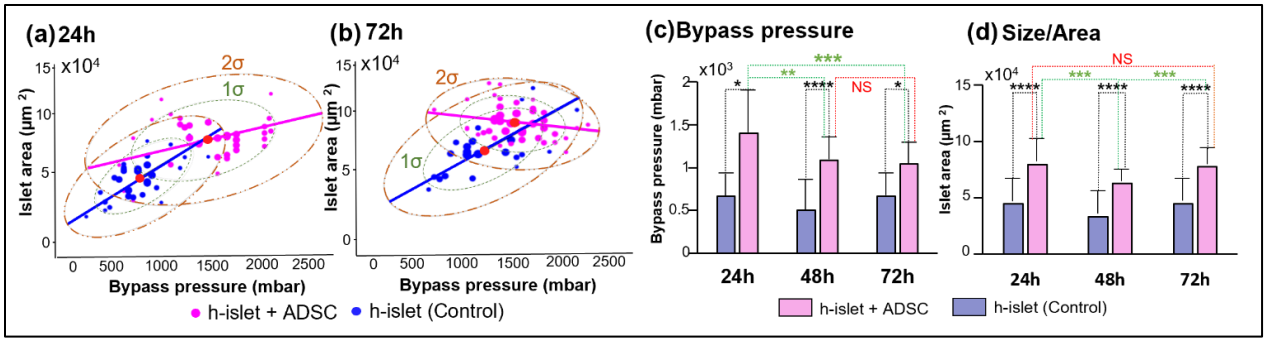

Figure 2.3. Bypass pressure of individual co-cultured h-islet + ADSC aggregates and h-islet controls plotted as h-islet area (μm^2) vs bypass pressure (mbar) after: **A.** 24 h, and **B.** 48 h co-culture (controls in blue and h-islets + ADSC aggregates in pink). The plot at 48 h is in supplementary material (Fig. S1b). One-way ANOVA showing 1σ (inner error ellipse) and 2σ (outer error ellipse) for: **C**. bypass pressure and, **D**. h-islet area, presented as mean SD with 95% CI, followed by a Tukey's multiple comparison test with ****p-value<0.0001, ***p-value<0.001, **p-value<0.01, *p-value<0.05 and NS is not significant. A two tailed t-test with Welch's correction (unpaired samples) was also done for comparing controls with their corresponding h-islets + ADSC for each time point.

To further characterize the interplay of aggregate size and inherent stiffness alterations during h-islet reorganization under ADSC co-culture, on the measured bypass pressure, we computed biomechanical opacity (O) as a size-normalized index, using the average aggregate area at each time point of the sample as the reference for normalization of the bypass pressure values. Hence, the biomechanical opacity versus area plot of **Fig. 2.4 A-C** for co-cultured h-islet aggregates should show near-zero slope. In fact, this is the case for slope of control h-islets after 24 h, 48 h and 72 h with no ADSC co-culture, as well as for islets co-cultured with the ADSCs for 24 h, wherein there is minimal difference in opacity for the control versus co-cultured h-islet populations (**Fig. 2.4 A**). On the other hand, opacity of the co-cultured aggregates starts to exhibit a size-dependent divergence versus that observed for control h-islets, after the 48 h (**Fig. 2.4 B**) and 72 h co-culture timepoints (**Fig. 2.4 C**). Based on this, we delineate the aggregate size at which the divergence in opacity begins to occur for the co-cultured h-islets versus the control islets. The aggregate size threshold for opacity divergence is seen to progressively increase from the 24 h

(**Fig. 2.4 A**) to 48 h (**Fig. 2.4 B**) to 72 h (**Fig. 2.4 C**) co-culture timepoints, per aggregate areas (μm^2 units) of: 6.3×10^4 (**Fig. 2.4 A**), 6.5×10^4 (**Fig. 2.4 B**) and 8.3×10^4 (**Fig. 2.4 C**). Hence, reorganization of the co-cultured h-islet aggregates occurs within 48 h for the smaller islets (those with area $< 6.5 \times 10^4$ μm^2 per Fig. 4b) to reach inherent biomechanical stiffness levels (as measured by opacity) that are greater than those of the control islets, but the larger islets (those with area $> 6.5 \times 10^4$ μm^2) continue to exhibit lower biomechanical stiffness (based on opacity). Similarly, islet aggregate reorganization after 72 h of co-culture is apparent for the population up to a higher size level, i.e., those with an area of 8.3×10^4 μm^2 (**Fig. 2.4 C**). In fact, in comparison to control h-islets, the co-cultured h-islet aggregates with higher biomechanical opacity are always the subpopulation with smaller than threshold size level, and the co-cultured h-islet aggregates showing lower biomechanical stiffness versus control h-islets are always the subpopulation with the larger than threshold size. A comparison of the size distribution of these two subpopulations is shown in **Fig. 2.4 D** at each of the co-culture time points (Day 1 – Day 6). This indicates that while two distinct size-based subpopulations are apparent for the co-cultured aggregates at the 24 h (Day 1), 48 h (Day 2) and 72 h (Day 3) timepoints, the respective subpopulations overlap in size distributions onward from Day 4 to Day 6. Also, reorganization of the co-cultured h-islet aggregates cause their net size to become progressively lowered over the entire culture period (Day 1 – Day 6 in **Fig. 2.4 D**). Since smaller-sized aggregates reorganize more rapidly, the progressively lowered aggregate size likely speeds up the reorganization process, thereby tightening their size and stiffness property distributions, as observed in **Fig. 2.3 A vs. 2.3 B**, due to completion of basement membrane remodeling.

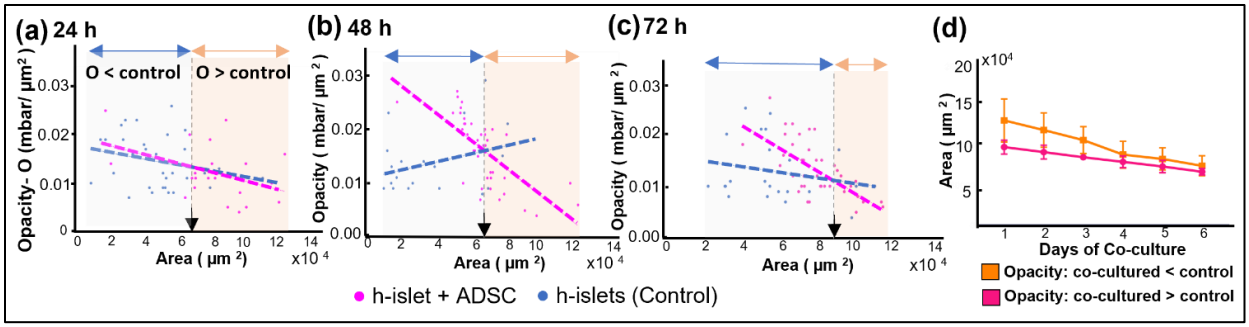

Figure 2.4. Area-normalized bypass pressure expressed as biomechanical opacity (mbar/µm2) plotted in log-scale versus measured area for the h-islet aggregate after ADSC co-culture versus the control (no ADSC in co-culture) after: **A.** 24 h, **B.** 48 h and **C.** 72h of co-culture show two distinct sized subpopulations (vertical dash line): one of smaller area with biomechanical opacity higher than the control and another of larger area with lower biomechanical opacity lower than the control. **D.** Size evolution for these subpopulations of co-cultured aggregates shows that the size differences become progressively smaller over the co-culture period (Day 1 to Day 6), presumably due to the reorganization leading to stiffer islets of smaller area, as suggested by the tighter data spread in Fig. 2.3A vs. Fig. 2.3B

2.4.3 Co-culture enhances secretion of pro-angiogenic and basement membrane-altering factors

After 144 hours (6 days) in culture, h-islets cultured with ADSCs secreted higher levels of pro-angiogenic factors including PDGF, PLGF, FGF-2, and VEGF (**Fig. 2.5 A**) and basement membrane altering factors including MMPs and TIMPs (**Fig. 2.5 B**) in the conditioned media than was secreted by human islets cultured alone (i.e., in the absence of ADCSs) or by ADSCs cultured alone. For example, VEGF secretion by human islets co-cultured with ADSCs was nearly 8-fold higher than VEGF secretion by islets cultured alone. The 5-fold higher level of VEGF secretion by ADSCs versus the respective level from islets cultured alone suggests that co-culture of islets with ADSCs boosts VEGF secretion levels by both islets and ADSCs in a synergistic manner.

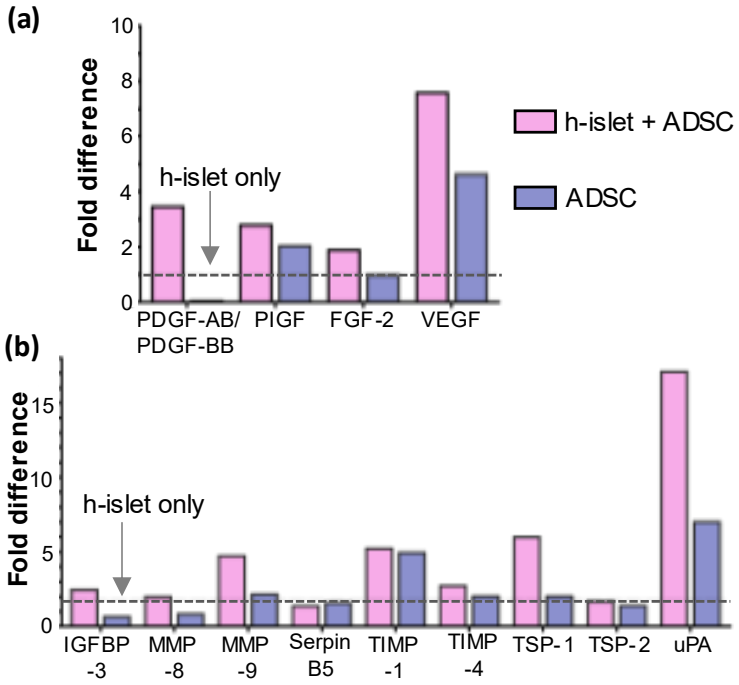

Figure 2.5 A-B. Profiling of conditioned media with ELISA shows that co-culture of human islets with ADSCs (pink bars) for six days (144 hours) increases secretion of matrix modifying proteins versus the respective levels from ADSCs cultured in isolation (blue bars) relative to islets cultured alone (dashed line).

2.5 Conclusions

The reorganization process of h-islet aggregates during their co-culture with ADSCs, which leads to enhanced expression of angiogenic and basement membrane altering factors, was characterized over time on a single-aggregate basis, using imaging and microfluidic biomechanical measurements. Based on fluorescence and bright field images, it is apparent that the co-cultured h-islet aggregates are merged with ADSCs, right from the 24 h co-culture timepoint, but their shape reorganization occurs more slowly and extends over the 6-day co-culture period. The reorganization process causes the co-cultured h-islet aggregates to transition from those predominantly with tails at the 24 h timepoint, to those with irregular shapes at the 48 h timepoint and to those with spherical shapes onward from the 72 h timepoint. The bypass pressure of single aggregates measured as a function of their

area shows that h-islet reorganization over the co-culture period leads to tightening of their size and stiffness property distributions. Furthermore, co-cultured h-islet aggregates below a threshold size level reorganize more effectively to exhibit more substantial increases in biomechanical opacity versus those above a threshold size level that take longer to reorganize and do not exhibit a proportionate rise in biomechanical opacity. While the threshold size level required for more complete h-islet reorganization starts with the smaller sized subpopulation, this size threshold is upshifted over the culture period to include h-islet aggregates of progressively larger sizes. Isolated h-islets of the same size ranges were kept in culture media during the same period of time without ADSC as measurement controls. H-islets co-cultured with ADSCs show two distinct subpopulations: one of higher biomechanical opacity with smaller than a threshold size, and one of lower biomechanical opacity with larger than a threshold size. However, threshold for size differences between the two subpopulations becomes progressively closer over the co-culture period. Hence, h-islet reorganization during ADSC co-culture likely causes basement membrane remodeling to lead to stiffer islets of smaller area that exhibit tighter spreads in their bypass pressure versus size plots. Since the subpopulation of h-islets that exhibit faster reorganization can be identified based on their distinct biomechanical opacity, this metric can potentially be applied to quantify and separate the fraction of h-islet aggregates that have reorganized after ADSC co-culture.

Chapter 3: Multichannel impedance cytometry downstream of microfluidic cell separation by Deterministic Lateral Displacement (DLD)

3.1 Introduction

Biological samples consist of subpopulations of a given cell type [55], since phenotypic heterogeneity is an essential feature of the organization and functioning of biological systems. This feature is most obvious with immune, cancer and stem cells that serve multiple biological functions [56], with competing functional roles of their phenotypic plasticity having an important role in the emergence of several disease [57] and therapeutic outcomes. This highlights the need for effective cell separation systems to understand the role of each cell type and identify specific cellular markers that can be correlated to functional outcomes of interest to disease onset and progression [58,59]. While this is performed effectively by flow cytometry after fluorescent staining [60] or magnetic functionalization [61] of characteristic surface proteins, followed by fluorescent or magnetic activated cell sorting, the sample preparation is time consuming, requires costly chemicals, introduces a degree of selection bias, and needs to be done off-chip, which causes sample dilution and limits the enrichment level possible for fractional subpopulations. Furthermore, identifying cellular surface markers are often not available for key biological functions, such as cancer metastasis [62], stem cell differentiation lineage [63] and immune cell activation [64]. While complementary approaches to identify cell phenotypes based on biophysical differences [65] in size [66], shape [67], deformability [68] and electrical properties [69] are emerging, multiparametric approaches for high dimensional identification of cells will be needed to discern subtle differences in subpopulations from the same cell type [70]. This has led to a recent thrust aimed at integrating multiple microfluidic separation methods on a single platform to

improve the discrimination of biophysical phenotypes and for separating subpopulations of interest [71,72,73]. Integration of on-chip cytometry within these hybrid platforms to monitor phenotypic and separation metrics at single-cell sensitivity, to utilize this information for active control of the deflection of target cells from other cells in heterogeneous samples can vastly improve the sample versatility and discrimination ability of these platforms.

This is especially important within passive microfluidic separation systems, such as those based on deterministic lateral displacement (DLD)[74], that possess the advantages of high throughput and robustness[75], but are usually designed for separations within specific sample types[76]. The ability to design microstructure arrays for steering particles along the displaced versus zig-zag streamlines, with a sharp particle size cutoff, makes the DLD technique ideal for sorting microscale cells of close size [77]. However, target cell types can exhibit wide size distributions, causing their separation ability to be limited by the relative position of particle size cutoff within the distribution of cell sizes. The integration of high throughput biophysical cytometry for in-line measurement and feedback during DLD can enable the systematic design of flow resistances to account for the size distributions of each cell type and also enable active control of separation force fields [78,79] to advance automation, relax device design requirements, and allow for more versatile samples.

We present the microfluidic integration of DLD for size and deformability-based cell separation, with single-cell impedance cytometry [80,81,82] for biophysical analysis on the same chip. Based on the overview layout of the respective sections of this integrated device the DLD separation (**Fig. 3.1 A**), magnified views are presented for the inlets (**Fig. 3.1 B**), the outlets (**Fig. 3.1 C**), and impedance cytometry on-chip (**Fig. 3.1 D**), with off-chip validation of the collected fractions (**Fig. 3.1 E**) to measure impedance magnitude and impedance phase over several simultaneously applied frequencies. While the operating flow rate and sample throughput of DLD and impedance

cytometry have a good degree of overlap, the integration of microfluidic separation upstream of biophysical cytometry presents a unique set of challenges. High throughput microfluidic separation by DLD requires microstructures designed over a large footprint (several square centimeters) and high depth (50-100 μm), while single-cell impedance cytometry at equivalent throughput requires confined geometries for sensitive measurements of the electric field screening by individual cells. This presents challenges associated with microfabrication, balancing of hydrodynamic resistances to allow for matching of volumetric flows and the use of co-flowing particles as internal standards for impedance analysis to normalize signals, account for positional dependence and quantify separation metrics, alongside biophysical analysis of cell phenotypes.

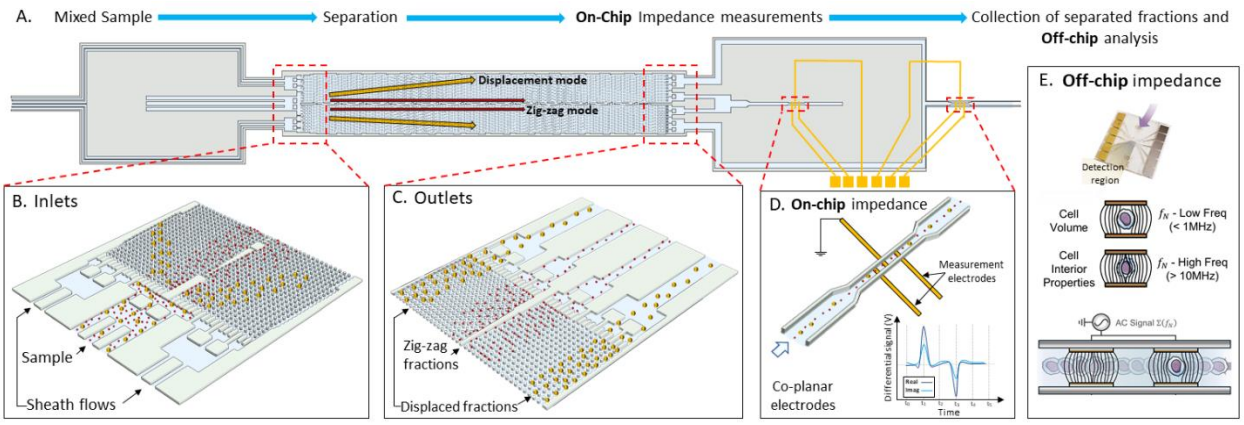

Figure 3.1 Schematic layout of the different sections of the integrated device: **A**. Overview of the workflow for DLD in its two separation modes: displacement mode and zig-zag mode. **B**. Device inlets, wherein mixed samples are injected through the central inlet branches, alongside sheath flows in the lateral inlet branches. **C.** Device outlet, wherein the smaller sized sample fraction is collected at the central channel and the larger sized sample fraction is collected at the lateral channels. **D**. The two on-chip impedance measurement sections are located just prior to the device collection reservoirs for cytometry of the separated fractions in each outlet. **E.** The collected samples of "large" and "small" sized fractions are analyzed by off-chip impedance cytometry.

To realize the application of this hybrid of DLD separation coupled to impedance cytometry to heterogeneous samples for separation and cytometry of subpopulations on a single chip, we

consider size-controlled fractionation of macrophages to enrich for subpopulations in their activated state. Macrophages are immune effector cells that display a high degree of phenotypic plasticity due to their role in several homeostatic functions [83]. Their infiltration at injury sites evokes a cascade of activation and associated inflammatory responses [84], but disease outcomes are determined by the balance of activation responses in their subpopulations [57]. Hence, it is of interest to enrich for subpopulations with activated phenotypes for quantification by cytometry. However, due to their dynamic and stimulus dependent phenotype [85,86], flow cytometry after staining for molecular markers from a specific signaling pathway is often unable to identify the full spectrum of macrophage activation [87], or enable longitudinal studies on activation dynamics for the same set of cells within the sample [88]. Using macrophages (Raw 264.7) stimulated by lipopolysaccharide (LPS) that activates the pro-inflammatory Toll-like receptor 4 (TLR4)[88], the activation state is determined based on impedance magnitude and phase, which is cross-validated based on the Griess assay for secreted nitrite (NO) in media[89]. Due to systematic cell size enlargement of macrophages under progressive activation, akin to that observed during leukocyte activation [90], we explore DLD-based separation for enrichment of activated macrophages, with on-chip impedance cytometry to monitor the size distribution and activation state of the enriched subpopulation. On-chip phenotypic measurement of DLD enrichment is also validated by off-chip cytometry for size based on impedance magnitude and for activation state based on impedance phase. In this manner, enrichment and on-chip quantification of the activated subpopulation can occur from the heterogeneous macrophage sample with a distribution of size and activation states, without dilution and cell viability loss of the enriched macrophage phenotypes, as would be observed with off-chip cytometry of the collected fractions after microfluidic separation.

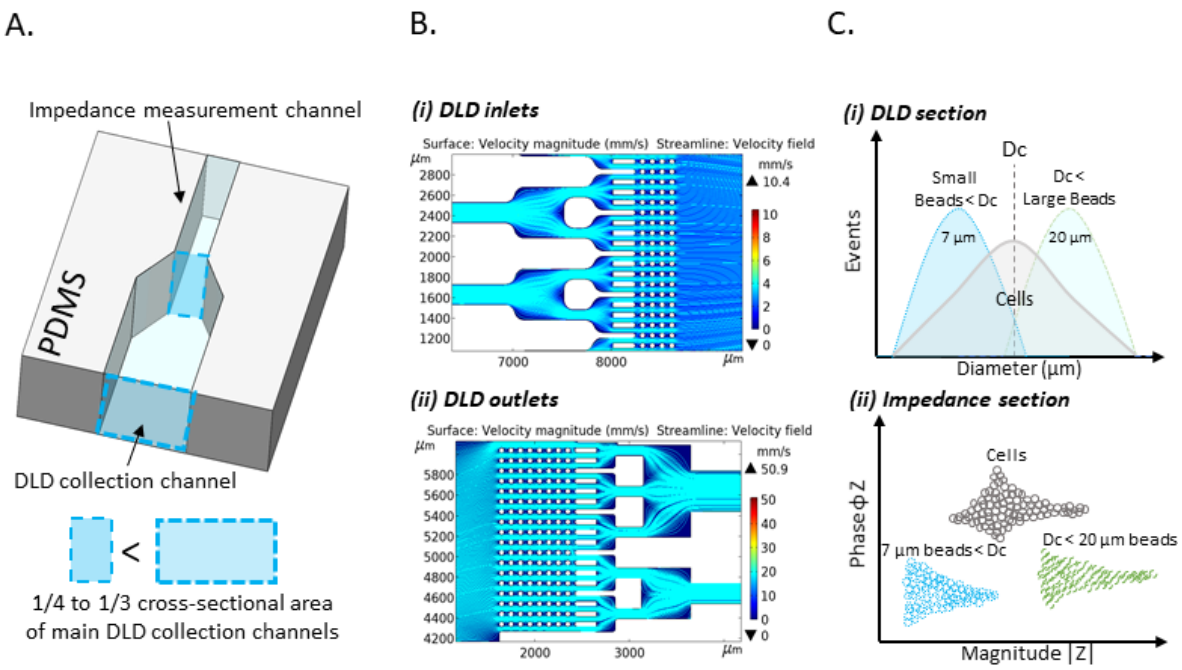

Figure 3.2 Device design and integration. **A.** Matching volumetric flows from the DLD array outlet and the impedance measurement sections. **B**. Balancing hydrodynamic resistances across the DLD array inlets and outlets, using CFD simulations for design validation. **C.** Co-flowing size-controlled beads with cells to establish DLD array separation metrics at each outlet, as well as for gating and normalizing the impedance data to enable comparisons across biological sample runs.

3.2 Device design and integration

Based on the overview presented in **Fig. 3.2**, we consider the specific design, integration, and operation tasks. To confine the detection volume for impedance cytometry while maximizing the throughput for collecting the fractions after DLD separation, the cross-sectional area of the impedance section is fixed at $\frac{1}{4}$ to $\frac{1}{3}$ that of the DLD collection channels (**Fig. 3.2 A**), with the height across all device sections fixed at 50 µm. The DLD designs were conducted following standard empirical relations [91], with edge corrections to prevent Dean flows in each array period section that can disturb laminarity and by shifting the first post in each period to decrease flow disruption when two flows merge. Since laminar flow conditions are needed across the device width for ensuring deterministic displacement of particles at the posts, we balanced the

hydrodynamic resistance at the inlets before the particles reach the DLD separation array. Resistance imbalances would cause the particles to jump across post lanes, thereby obviating particle separation based on displaced or zig-zag motion at the designed critical diameter (D_c) [92]. Similarly, flow resistances must also be balanced at the outlet region from DLD, including the additional section leading to the impedance cytometry measurement region, so that the separated fractions can flow into their respective collection channels without resistance imbalances causing the separated fractions to cross lanes. The CFD simulations in **Fig. 3.2 B** show that the inlet and outlet branches have the same resistance level across the whole width of the device. [92]. These CFD simulations were used to optimize the design of the DLD separation region, while including a section of the channel for inertial focusing of the separated cells along a similar depth streamline [93,94] prior to in-line impedance cytometry, using a coplanar electrode design with automated position correction [95,96]. Since cells in typical biological samples exhibit wide size distributions, co-flowing size-controlled polystyrene beads in a size range that spans the range for cells in the sample (7-20 μm) were used as internal standards to assess separation metrics (**Fig. 3.2 C**) and to carry out the normalization of impedance cytometry data, to enable comparisons across multiple sample sets. In this manner, we can assess the efficacy of cell separation versus that of size-controlled beads and carry out normalization to account for any temporal variations.

The overall integrated device set-up (**Fig. 3.3 A)** includes a 3D printed holder to integrate the microfluidic chip for fluidic, electrical, and optical interfacing; the inlet sample and sheathing flows into the DLD array (**Fig. 3.3 B**); and the impedance measurement section downstream from DLD separation, using a custom designed PCB for automated acquisition and triggering of downstream signals (**Fig. 3.3 C**). Also shown are images of flowing mixed sample into the inlet (**Fig. 3.3 D(i)**), the separated fractions after DLD separation into their respective collection

channels (**Fig. 3D(ii)**) and the on-chip impedance-based cytometry sections (**Fig. 3D(iii)**).

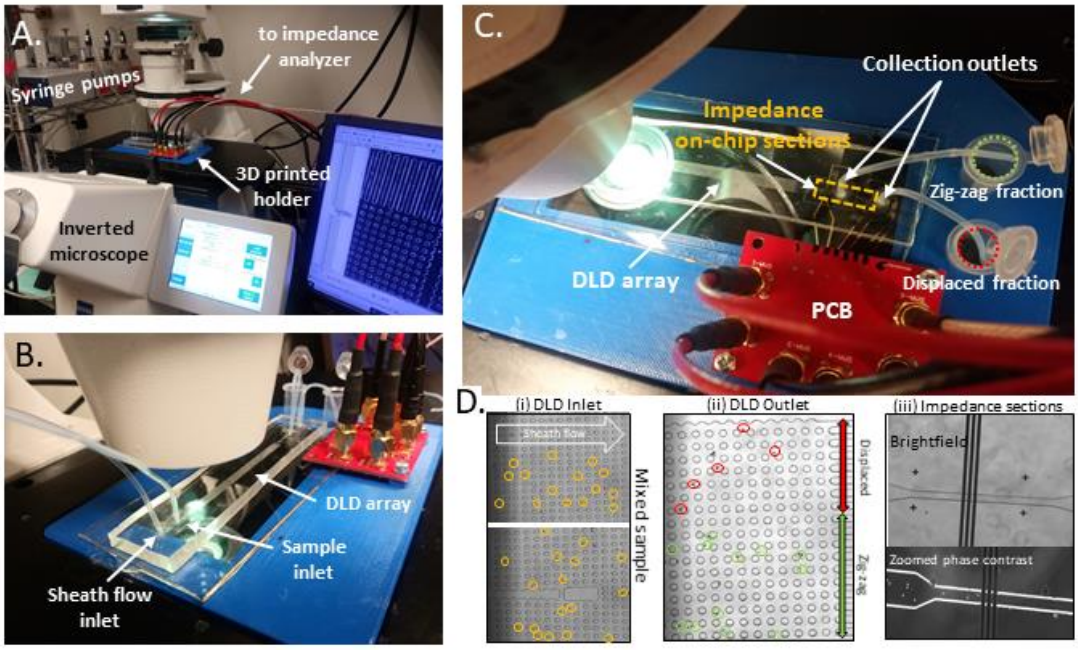

Figure 3.3 Integrated device. **A**. 3D printed holder for fluidic, electrical and optical interfacing of the chip for DLD separation and on-chip impedance measurement. **B.** Close up of the sample and sheathing flows at the inlet. **C.** Top view of PCB connections to the impedance electrodes, as well as collection of DLD separated fractions. **D.** (i) Images of mixed sample flowing into the inlet, (ii) Separated fraction at the end of the DLD array flowing into their respective collection channels and (iii) On-chip impedance measurement section

3.3 Experimental methods

3.3.1 Device Fabrication

The microfluidic device **(Fig. 3.3)** was fabricated by photolithography of the master (EVG 620 mask aligner), using a mylar mask (Cad Art) and a negative photoresist (SU-8 2150, Kayaku) for pattern definition. Micro-molding with PDMS or polydimethylsiloxane (Sylgard 184, Dow Corning) was performed using uncured elastomer base to curing agent in the 10:1 ratio and crosslinking at 65 C for 8h to obtain the device features. After curing, the PDMS chip was released from the master; the PDMS features were diced, and the inlets and outlets were made with a biopsy

punch. The electrodes were patterned with a positive photoresist (AZ 1505, Micro Chemicals) and Ti-Au was deposited into a glass substrate (D263, University Wafer) using electron beam evaporation. Once the Au layer was deposited, the surplus photoresist was removed following a standard lift-off process. The PDMS chip and the glass substrate with Au electrodes were bonded and manually aligned after treating their surfaces with oxygen plasma (Tergeo, Pie Scientific)

3.3.2 Sample Preparation

Macrophages Raw 264.7 cells were obtained from American Type Culture Collection (ATCC) (Manassas, VA) and cultured with Dulbecco's modified Eagle's medium (DMEM, high glucose 4.5 g/L, Gibco, Grand Island, NY) with 10% fetal bovine serum (FBS) (Gibco), 1% penicillin (100 μg/mL), and 1% streptomycin (100 μg/mL) (Gibco) and maintained in 5% CO_2 at 37 °C incubator (Thermo Fisher). The cell seeding density was done using a 24 well plate including: 5×10^5, 2×10^5, and 1×10^5 cells/mL, with 0.5 mL per well, to yield 2×10^6, 1×10^6, and 2×10^5 cells per well after culture in complete growth media overnight and then in serum-free media for 1 day.

For activating macrophages with LPS, a 24-well plate, Raw 264.7 cells were pre-seeded in the complete growth media with a density of 1×10^5 cells/mL (0.5 mL/well) overnight. Cells treated with serum free media were replaced with or without LPS at differing doses and durations.

3.4 Results

3.4.1 Validation of DLD separation by cytometry

The integrated device (DLD with on-chip impedance cytometry) was validated based on its ability to separate standard sized polystyrene beads of differing sizes. Since our DLD separation array was designed for a cutoff of D_C of 11.63 μm, we investigated the separation of 7 μm beads versus 12 μm (**Fig. 3.4 A**), 15 μm (**Fig. 3.4 B**), and 20 μm beads (**Fig. 3.4 C),** by off-chip

forward scattering flow cytometry (FSC) and on-chip impedance cytometry (**Fig. 3.4 D**) to measure proportions in the input (i), zig zag (ii) and displaced outlets for each sample type.

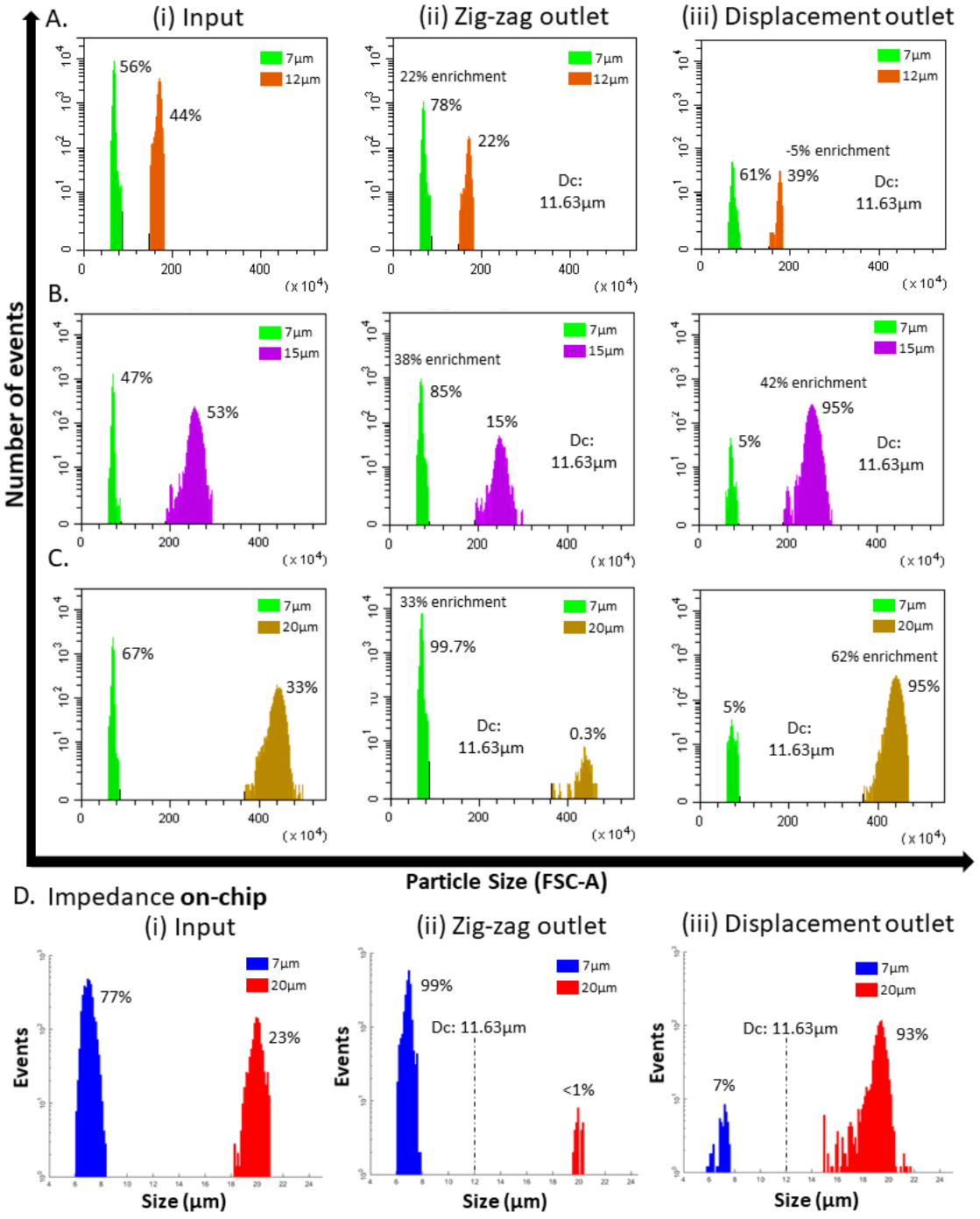

Figure 3.4 Validation for DLD separation of 7 µm beads versus 12 µm, **A.** 15 µm **B.** and 20 µm beads **C.** using off-chip forward scattering flow cytometry (FSC) and on-chip impedance cytometry **D.** showing the analysis for the: (i) input sample; and fractions in the (ii) zig zag outlet, and (iii) displacement outlet.

Based on these results, it is apparent that for a DLD array design for D_C of 11.67 μm, while 7 μm beads exhibit a 22% increase in the zig zag outlet versus the input sample (**Fig. 3.4 A(ii)**), 12 μm beads do not exhibit an increase in the displacement outlet **(Fig. 3.4 A(iii))** due to their proximity to the D_C value. Considering 7 μm versus 12 μm beads, the 7 μm beads exhibit a 38% increase in the zig zag outlet versus the input sample (**Fig. 3.4 B(ii)**) and the 15 μm beads exhibit a 42% increase in the displacement outlet (**Fig. 3.4 B(iii)**), indicating moderate level of separation. Considering 7 μm versus 20 μm beads, the 7 μm beads exhibit a 33% increase in the zig zag outlet versus the input sample (**Fig. 3.4 C(ii)**) and the 20 μm beads exhibit a 62% increase in the displacement outlet (**Fig. 3.4 C(iii)**), indicating good level of separation, especially for the larger sized fraction. Finally, on-chip impedance cytometry confirms the ability to enrich 7 μm beads within the zig zag separated fraction, to ~99% levels from a mixed sample with 20 μm beads, with the latter enriched to a 93% level in the displaced fraction. This benchmarks the size-selective separation abilities of the DLD array, while also validating the on-chip impedance cytometry measurements versus off-chip forward scattering flow cytometry.

3.4.2 Application towards enrichment of activated macrophages

Due to their role within multiple immune functions, the phenotypes of macrophage cells can exhibit a degree of heterogeneity, motivating the need for single-cell measurements. The heterogeneity can influence their activation state, with the net balance between subpopulations being responsible for inflammatory response[57]. Hence, microfluidic methods to separate subpopulations for assessing their activation response can advance the ability to sensitively detect the effect of immunomodulatory drugs on recovery of macrophages from their activated state. Stimulation with lipopolysaccharide (LPS) at 100 ng/mL over a 24 h period is the standard protocol

for macrophage activation. Based on macrophage cell culture after LPS stimulation and trypsinization for impedance cytometry to measure single-cell impedance magnitude (|Z|) and phase parameters (ϕZ) over four frequencies (**Fig. 3.5 A**), it is apparent that macrophage activation causes a progressive increase in cell size with increasing duration of LPS stimulation (**Fig. 3.5 B**), similar to prior work with leukocyte activation[37]. In fact, while the electrical cell size histograms exhibit a degree of overlap, the two-dimensional single-cell data clusters in impedance phase at 0.5 MHz ($\phi Z_{0.5\ MHz}$) versus electrical size (or $\sqrt[3]{|Z|_{0.5\ MHz}}$) exhibit clear differences in the phenotype of untreated cells as the "control" sample versus 24 h LPS treatment as the "activated sample" (**Fig. 3.5 C**), due to downshifting of $\phi Z_{0.5\ MHz}$. The activation is validated based on the standard Griess assay for nitrite in the media (**Fig. 3.5 D**).

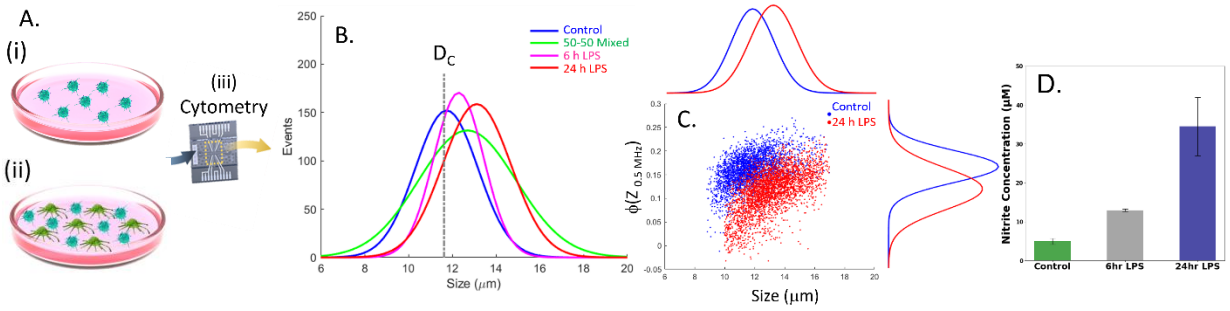

Figure 3.5 Macrophage activation (**A(i)** vs. **A(ii)**) assessed by single-cell impedance cytometry (**A(iii)**) shows progressive alterations in electrical size of cells **B.** as well as downshifting in $\phi Z_{0.5\ MHz}$ with activation **C.** which is validated by Griess assay for secreted nitrite in media **D**.

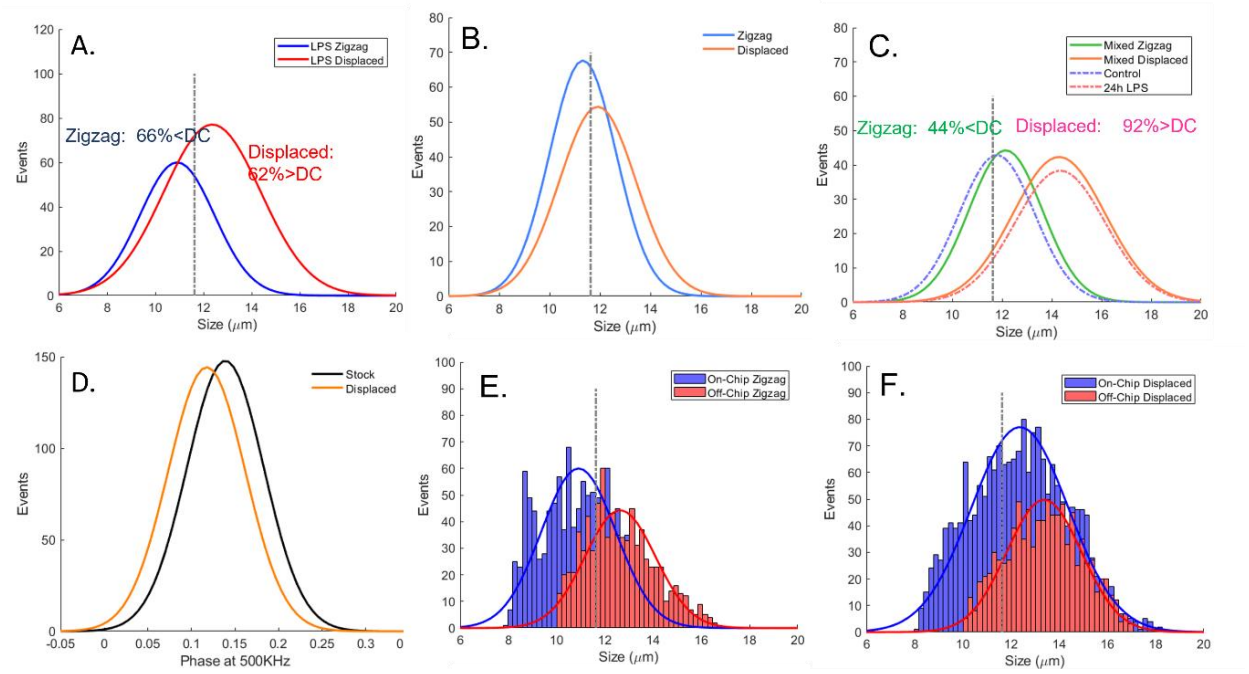

Figure 3.6 Comparison of the DLD separation with on-chip impedance cytometry for different macrophage samples: **A.** 24 h LPS-treated; **B.** Control untreated sample; and **C.** 50-50 mixed sample of A & B, shows improved DLD separation ability of samples **A** and **C** versus **B**, due to the position of D_C versus the mean of the cell size distribution histograms. The displaced fractions from the 50-50 mixed sample show downshifted $\phi Z_{0.5\ MHz}$ levels versus the input sample **D**. indicating activation. The size distribution histograms from on-chip impedance cytometry compare well to those from off-chip impedance cytometry for the zig zag **E.** and displaced fractions **F.** from the 24 h LPS treated sample.

Based on the systematic cell size alterations upon macrophage activation (**Fig. 3.5 B**), we explore the ability to utilize DLD to enrich for the highly activated cells in each sample, with on-chip impedance cytometry utilized to monitor the efficacy of size-based separation and the number of cells in the separated fraction that show downshifting of the impedance phase ($\phi Z_{0.5\ MHz}$), alongside off-chip impedance cytometry to validate the on-chip measurements. To investigate the effects of sample heterogeneity, we consider a mixed macrophage sample with a 50% "control" and 50% "24 h LPS" treated cells, that seeks to simulate the sample after 6 h LPS treatment (**Fig. 3.5 B**). However, while the mixed bead samples of **Fig. 3.4** show sharp size distributions at particular sizes for which a DLD array with a clear cutoff can be designed for separation (D_C=11.63 μm),

the wide size distributions of the respective macrophage samples (**Fig. 3.5 B**) makes it challenging to apply a similar array for DLD separation. This becomes apparent from the overlay of D_C on the respective size distribution histograms (**Fig. 3.5 B**), which show the D_C right on the mean of the histogram for the "control" sample, but shifted by at least one standard deviation from the mean for the 24 h LPS treated sample. Since cell separation towards the DLD displaced versus the zig zag fraction is determined by the product of displacement probability and the cell numbers available to crossover close to D_C, the dominance of the latter number around the histogram mean for the "control" sample shows poorer distinctions in cell size between zig zag versus displaced cells (**Fig. 3.6 B**), whereas this size-based separation is more effective for the "24 h LPS" (**Fig. 3.6 A**) and the "50-50 mixed" samples (**Fig. 3.6 C**). It is noteworthy that after the DLD separation of 24 LPS sample (**Fig. 3.6 A**), 66% of cells within the zig zag fraction are below D_C and 62% of cells within the displaced fraction are above D_C. On the other hand, DLD separation of the "50-50 mixed" sample (**Fig. 3.6 C**) shows 44% of cells within the zig zag fraction are below D_C and 92% of cells within the displaced fraction are above D_C. In fact, after the DLD separation, the size distribution profile for the zig zag fraction resembles that of the "control" sample and for the displaced fraction resembles that of the "24 h LPS" treated sample (dotted curves), which indicates the good separation ability of DLD for this sample. The cells separated in the displaced fraction show downshifted impedance phase levels ($\phi Z_{0.5\ MHz}$) in **Fig. 3.6 D**, similar to that observed for activated macrophages (**Fig. 3.5 C**). The size distributions from impedance performed on-chip versus off-chip show a good degree of overall similarity (**Fig. 3.6 E vs. 3.6 F**), but the data suggests that the smaller sized cells picked up by on-chip cytometry are not present within the off-chip cytometry results. Since continued collection of cells is needed over several hours (at least 2h) to have enough events for off-chip cytometry, it is possible that smaller cells adhere more strongly

to the edges of the collection region versus larger cells, or that cells get enlarged due to continued alterations in activation state or cell swelling under viability loss, therebt causing the reported differences between on-chip and off-chip cytometry. More broadly, this highlights the need for on-chip cytometry for real-time measurement during DLD separation to ascertain the efficacy for choice of the appropriate device (micropost design for D_C and number of lanes for collection of zig zag versus displaced fractions), sample (heterogeneity in cell size distributions to account for day-to-day sample variations), and active modulation conditions (flow resistance control or electric field based steering) to improve separation within complex samples of unknown heterogeneity

3.5 Conclusions

We have developed an integrated device with DLD separation coupled to on-chip impedance cytometry to monitor the separation metrics and phenotypes of the separated fractions. This required the ability to maximize cell collection from DLD separation into a confined channel geometry for high sensitivity impedance cytometry, the balancing of flow resistances across the width of the DLD separation array to main laminarity, and the design of an inertial focusing region for cells to minimize positional alterations across the channel depth. Utilizing co-flowing beads with a distribution of sizes as internal standards for DLD separation and for normalization of the impedance cytometry data, we developed methodologies for effective comparisons across cell samples. This integrated DLD separation with on-chip cytometry device was applied for size-based enrichment of macrophage subpopulations with high degrees of activation, since activation progressively enlarges the electrical cell size. This was applied to samples with a wide size distribution, including the 24 h LPS treated sample and the 50-50 mixed sample with equal

proportion of cells from the untreated control and the 24 h LPS treated sample. Based on this, the displaced fraction after DLD separation showed cell size levels higher than D_C (62% for the 24 h LPS sample and 92% for the 50-50 mixed sample). In fact, size distributions from the latter sample suggest that the zig zag fraction resemble the control sample and from the displaced fraction resemble the 24 h LPS treated sample. The displaced fraction shows consistent downshifting of their impedance phase levels versus the respective input sample, which is characteristic of cells in their activated state. The size distributions from on-chip impedance cytometry compare well to that from off-chip cytometry and we attribute the minor differences due to the inability to effectively collect smaller sized cells. Future work will focus on separation of subpopulation from other samples with wide size distributions, such as stem cells and cancer cells, that exhibit size-based phenotypic cutoffs related to stem cell differentiation lineage or cancer metastasis ability.

Chapter 4: Device integration for electrophysiology-based separation and measurement

4.1 Introduction

The biophysical phenotypes of cells, including size, shape and subcellular characteristics, such as membrane morphology, cytoplasmic complexity and nucleus to cell size can determine its function and lead to heterogeneity. Electrical metrics of the cell physiology (henceforth called electrophysiology) are sensitive indicators of their biophysical properties. For instance, membrane conductance is related to the activation of ion channels, membrane capacitance is related to its morphology, and interior conductivity is altered due to the phenotype of organelles and nucleus to cell size. Using microfluidic structures that create spatial field non-uniformities, cells can be translated by dielectrophoresis (DEP), either towards the high field by positive DEP (pDEP) or away from the high field by negative DEP (nDEP).

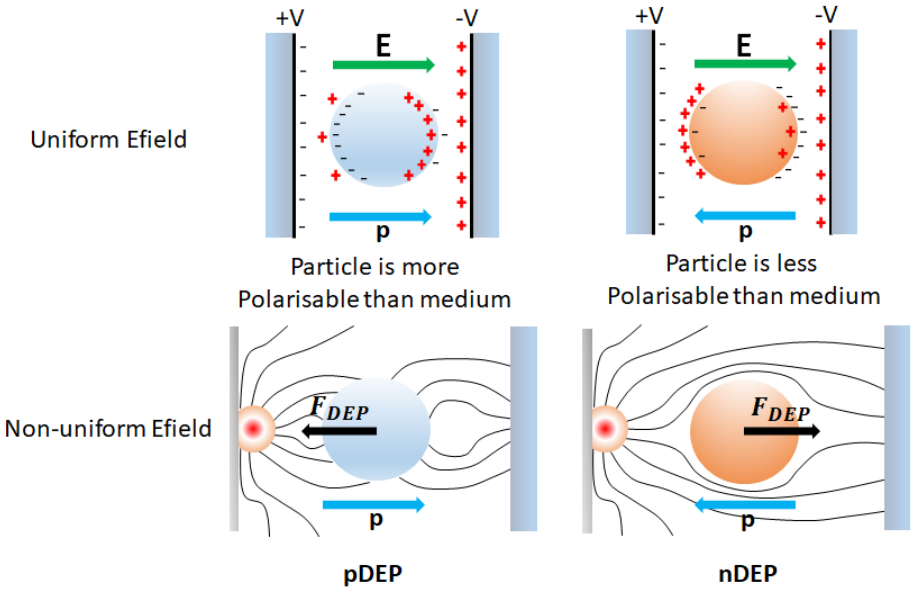

Figure 4.1 Dielectrophoresis (DEP) principle

Dielectrophoresis (DEP) refers to the movement of particles due to relationship of the direction of their net dipole versus that of the applied field. The most common example is a spherical particle of high conductivity located between two electrodes and suspended in a low conductivity and high permittivity electrolyte. Starting with a uniform AC field, if the polarizability of the particle is greater than that of the medium then an interfacial dipole will be formed that is aligned to the field. Under a spatially non-uniform field, this causes pDEP. Conversely, if the polarizability of the particle is less than that of the medium then net dipole is dominated by charges in the medium around the particle, thereby leading its net dipole to be anti-parallel to the field direction [97, 98] as it was mentioned in chapter 1. Under a spatially non-uniform field, this causes pDEP. While the applied electric field is screened completely around the cell at low frequencies to cause DEP separations based on cell size, membrane polarization occurs at successively higher frequencies to enable separations based on electrical capacitance differences that depend on cellular membrane morphology. At even higher frequencies wherein the membrane is short circuited, cytoplasmic conductivity differences drive the separation based on the cellular interior structure.

There are important implications on biological function and disease response that are linked to the degree of phenotypic heterogeneity that cellular systems exhibit [99, 100]. Currently, phenotypic heterogeneity is quantified using fluorescent-activated flow cytometry methods. While this method is highly specific due to binding of cell receptors to fluorescently labeled antibodies and it gives multi-dimensional data on cell phenotypes [101], some drawbacks include its need for costly labeling steps, sample dilution, skilled technicians and rather sophisticated instrumentation. Furthermore, cell receptors are not often well-defined for various types of tumor [102] and stem cells [103]. Finally, since flow cytometry functions as an endpoint assay, it cannot be used repeatedly to analyze the same set of cells for kinetic monitoring of cell phenotype under different

interventions [104]. Hence, there is much interest in alternate methods for biophysical analysis of single-cells, in a label-free manner based on their inherent properties [105].

4.1.1 DEP as a label-free method

Cell membrane capacitance is a label-free phenotype that can serve as a specific metric to identify cells based on their size and morphological characteristics [106]. Recent work has shown that membrane capacitance can serve as a marker to stratify vesicles based on their lipids [107], determine the viability of bacteria [108] and their adherence ability to host cells [109], identify parasite-infected red blood cells (RBCs) [110], quantify the morphological state of tumor cells in their adherent state [111] and predict the lineage of neural stem cells [112]. A common way to measure membrane capacitance is based on determining the dielectrophoretic crossover frequency of cells within media of varying conductivity [113,114,115]. For this purpose, the translation of polarized cells under a spatially non-uniform electric field is followed to determine the frequency at which the cells transition from negative dielectrophoresis (nDEP) or translation against the field gradient due to field screening by the cell, to positive dielectrophoresis (pDEP) or translation along the field gradient due to field termination at the cell [116].

4.1.2 Current DEP methods

DEP crossover frequency measurements are often carried out in a batch-mode using quadrupole or castellated electrode configurations [117], due to their well-defined field gradient direction owing to distinct regions of high field and low field within these device structures. However, for the purpose of effectively quantifying phenotypic heterogeneity, there is a need to measure a large number of events (10^4-10^6 cells) within a short time (< 1 h). Hence, there is a need for continuous-flow device configurations capable of rapidly detecting field screening on single-cells, as they flow past regions of field non-uniformity at high flow rate. A major limitation in this regard is that since

field non-uniformities are usually highly localized (i.e., on the order of magnitude of cell size) for the purpose of enhancing DEP translation, due to its ∇E^2 dependence, the level of DEP translation falls off sharply within a few microns away from the field non-uniformity. Hence, a significant proportion of cells within the device do not often experience large enough alterations in translation for enabling facile distinction of the DEP cross frequency. Furthermore, even if the field non-uniformity were to be enhanced based on sharp features and/or enhanced voltage levels, the time period available for translating cells under DEP can drop off as the flow rate of cells through the device rises. Finally, DEP analysis of higher cell concentration levels has been limited by dipole-induced cell-cell interactions. As a result, DEP analysis has often been limited to relatively low throughput levels (well below 1 μL/min) and low cell number rates ($<10^3$ cells/min), which are often not sufficient to quantify phenotypic heterogeneity with statistical certainty.

Various flow through configurations for DEP analysis and separations have been used to assess cells based on their crossover frequency, including various methods based on planar electrodes, such as cell-levitation by DEP field flow fractionation (DEP-FFF) [118] and cell-deflection based on gradients in media conductivity [119]. In order to address the problem that planar electrodes have a limited spatial extent of field non-uniformity over the device depth, various sidewall electrode configurations have been developed [120], but these are often difficult to fabricate reproducibly. Easier fabrication strategies for sidewall electrodes have been demonstrated in recent work by filling PDMS channels with conducting composites [121], so that hydrodynamic focusing can be used to place cells in the vicinity of the non-uniformity. However, filling of dead-end PDMS channels with conducting composites can cause poor definition of the metal interface to the fluidic channel [122], whereas strategies based on lead-in channels with an inlet and outlet that better define this interface can limit the spacing between the DEP electrodes to > 100 μm, thereby

reducing the field levels. Alternatively, there are various electrode-less strategies based on the field non-uniformity created by insulators, with the field applied by global external electrodes [123,124,125]. However, this configuration restricts the level of applied field, especially at high MHz frequencies, wherein voltage amplifiers exhibit losses [126]. Additionally, since only one set of electrodes can be used per channel in this configuration, the lack of voltage addressability limits the ability to spatially modulate fields for carrying out electrically independent downstream separations.

4.2 Sequential field non-uniformities for high throughput dielectrophoretic separation

Current electrode-based device geometries for DEP extend over a limited depth of the sample channel, thereby reducing the throughput of the manipulated sample (sub-μL/min flow rates and $<10^5$ cells/mL), as reflected in the poor collection efficiency. Furthermore, since cells can start out at varying directions versus the field non-uniformity their deflected streamline is not solely dependent on their electrical physiology. We hypothesized that by creating a set of self-aligned sequential field non-uniformities in the lateral direction of the sample channel width (100 μm), with a field that extends uniformly across the depth direction, the throughput for DEP manipulation can be enhanced to improve collection efficiency. Additionally, flow focused cells under the sequential field non-uniformity can be progressively deflected, with minimal dependence on their starting position, orientation or interaction with neighboring cells, thereby causing separation into a streamline that is solely determined by their electrical physiology, which improves selection purity.

To address these deficiencies, we present a device configuration combining 3D insulator constrictions with a set of addressable planar electrodes so that the net spatial extent of the field non-uniformity exceeds that of a configuration with 3D electrodes extending over the entire

channel depth, which is difficult to fabricate. As a result, hydrodynamically focused cells traversing at high flow rates (>1 μL/min) over a range of streamlines in the vicinity of the field non-uniformity can be deflected by dielectrophoresis at high cell number rates (~10^6 cells/min). This study is focused on presenting the field profiles and particle tracing simulations for this so-called dynamic-DEP (Dy-DEP) device configuration to enable its comparison to the equivalent device with 3D electrodes, as well as present its application towards determining the crossover frequency of red blood cells (RBCs) based on spatially distinct streamlines for nDEP, pDEP and no DEP over a range of media conductivities. Based on independent validation of the determined membrane capacitance of RBCs for device operation at high flow rates and high cell number rates, we envision the application of this device configuration in future work for the purpose quantifying phenotypic heterogeneity.

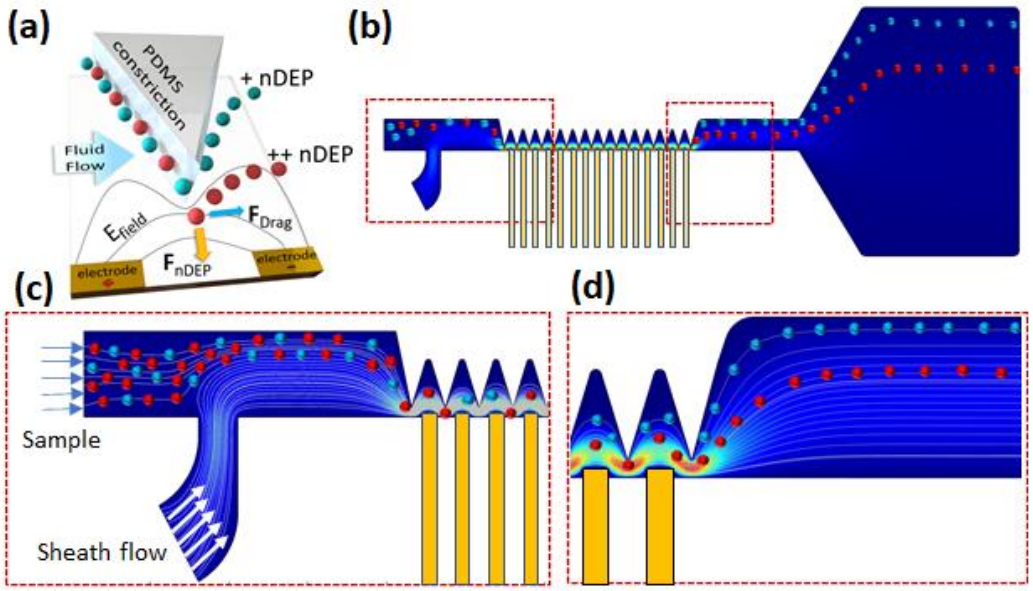

Figure 4.2 Schematic of microfluidic device for dynamic dielectrophoresis (Dy-DEP): **A**. Functioning principle based on balance of nDEP versus drag forces; **B.** overall chip design; **C.** focusing effect of the sheath flow pushes cells in the sample away from electrodes and towards the constriction regions of the device; **D.** example differences in fluid flow streamlines of cell types with differing DEP response.

Figure 4.2 shows a schematic of the overall microfluidic Dy-DEP device and its operating principle for separating cells into differing streamlines based on magnitude and direction of DEP response. Per Fig. 4.1 a, our overall objective is to develop a device that can deflect each cell traversing the field non-uniformity regions created by consecutive insulator constriction tips, due to a balance of dielectrophoretic trapping force (F_{nDEP} away from tip or F_{pDEP} towards the tip) versus the drag force (F_{drag}), so that cells can be separated along differing streamlines based on their dielectrophoresis levels (Fig. 4.1 b). For this purpose, the sample with cells is focused along the streamlines close to the channel wall using a sheathing flow of much higher flow rate (3x of sample flow rate), so that each cell in the sample has the opportunity to interact with the high field points at the constriction tips. Under this spatial field non-uniformity, cells experience dielectrophoretic translation based on a magnitude and direction that depends on the frequency dispersion of their polarization response versus that of the surrounding media. In the situation wherein F_{DEP} (pDEP or nDEP) just exceeds F_{drag}, the cells undergo translation across flow streamlines to continue along the particular streamline wherein the net DEP and drag force are equal. While Fig. 4.1 d shows the schematic for separation of streamlines based on nDEP level, our subsequent results demonstrate separation of the cell streamlines based on their DEP behavior; i.e., pDEP, no DEP at crossover frequency (f_{xo}) and nDEP level, while the high net flow rate of the cells (sample plus sheathing flow rate of 1.68 μL/min) ensures continuous particle deflection with no DEP trapping across the length of the device. Table 1 lists the distinguishing characteristics of the current study versus prior work. While the prior work has been focused on engineering separations using dilute cell samples operated at a low enough flow rate to ensure a significant time period for action of the DEP force, our work is focused on high throughput cell analysis to determine frequency and media conductivity ranges for different levels of nDEP, no DEP at crossover, and pDEP, due to cell

deflection across streamlines to characteristic positions based on their DEP behavior. The reported device is validated using red blood cells (RBCs) obtained from human blood samples diluted to concentration levels of 2.25×10^8 cells/mL for demonstrating DEP analysis at a throughput of $1.1x10^5$ cells/min, so that the determined spectra and membrane capacitance can be compared to prior work. Hence, the device is particularly suited for the purpose of high throughput characterization of the DEP dispersion behavior to stratify phenotypic heterogeneity of a particular sample based on their DEP crossover frequency, without the need for significant dilution.

Table 4.1 Distinguishing characteristics of device in current study versus prior work

Citation	**Device**	**Sample Type (DEP type)**	**Initial Conc. (# per mL) †**	**Flow rate (µl/min)∗**	**Frequency**	**Media σ_m (S/m) ††**	**Throughput (cells/min)**
[127]	X pattern insulating structure with 3 types of electrodes: planar, dual-planar and 3D electrodes	Live *vs.* dead HeLa cells (pDEP level)	1×10^7	0.54	1 kHz	0.00176	5×10^3 – 4×10^4
[119]	Diagonal top-bottom planar electrodes in channel under a conductivity gradient	Live *vs.* dead yeast cells (crossover)	5×10^6	3	100kHz-10MHz	0.0093-0.047	1.5×10^4
[128]	Planar slanted electrodes with sheathing flow to focus sample on sidewalls	Platelets from diluted whole blood (nDEP level)	5×10^8	2.5	1 MHz	0.05	1.32×10^6
[129]	Planar electrodes with asymmetric orifices to generate the non-uniform field on sheath flow focused sample	Live *vs.* dead yeast cells (pDEP level)	Not reported	0.225	1kHz-10MHz	5.5×10^{-6}	Not reported
[118]	DEP-FFF in channel with planar	Various types of cells (nDEP level)	1×10^6	20 (diluted sample)	5-60 kHz	0.01-0.05	10^4 – 10^5

	interdigitated electrodes						
[121,122]	3D AgPDMS electrodes along channel with sheath flow focusing of sample	Live *vs.* dead yeast cells, as well as beads (pDEP level)	10^7-10^6	0.1 (S) + 0.9 (F) §	0.1-1 MHz	0.02-0.05	Up to 10^3§ (using highest sample level)
[130]	Set of recessed planar electrodes with sheath flow focusing of sample	Platelets from RBC & WBC (pDEP level)	~10^8	0.02 (S) + 0.08 (F)§	0.1 MHz	5×10^{-4}	< 2.5×10^3§ (using highest sample level)
[131]	3D ionic electrodes create funnel shaped field non-uniformity (pDEP level)	Various cell types and viability	0.5×10^6	0.83 (S) + 4.17 (F)	10 kHz – 1 MHz	10^{-3}-10^{-4}	4.1×10^3
[132]	Serpentine channel for inertial focusing with interdigitated planar electrodes and sample focus by sheath flow	Size-based separation of polystyrene beads (pDEP level)	1.4-8.5 $\times 10^5$	100 (S) + 200 (F)	0.1-30 MHz	1.5 – 2.4 $\times 10^{-4}$	1.4 – 8.5 $\times 10^4$
Current device	DEP-induced deflection of flow streamlines at 3D insulator constrictions with focused sample	RBCs from whole blood (nDEP level, crossover & pDEP)	2.25×10^8	0.48 (S) + 1.20 (F)	10 kHz -10 MHz	0.0017 to 0.0525	$1.1x10^5$

† - Initial sample concentration of cells; ∗ - S=sample and F=focus flow; †† - σ_m is media conductivity; § - estimated

4.3 Experimental and Theoretical Methods

4.3.1 Microfluidic device fabrication and assembly

The device was microfabricated by standard photolithography methods using SU-8® photoresist (2025, MicroChem) and a mask aligner (EVG 620, EV Group) to generate a patterned master. Following this, PDMS (SylgardTM 184, Dow Corning) was cast into the master and crosslinked

at 60°C overnight. PDMS chips were then cut and a biopsy punch was used to create the inlets and outlets. Separately, electrodes were patterned on a glass wafer (University Wafer) by first patterning an underlying resist (AZ-1512, MicroChem) followed by electron beam deposition of an overlayer of Au (100 nm) over a Ti adhesion layer (5 nm), so that the lift-off technique with acetone can be used to remove excess resist to pattern Au on glass. The glass wafer was diced (DISCO DAD 3240, Kiru-Kezuru-Migaku Technologies) to obtain microchips with the patterned electrode features on glass. Following this, the electrode features were aligned to the PDMS channel features using a stereoscope and clamped for bonding under a low energy plasma system (Tergeo, Pie Scientific) for 30s and 20 W power. The channel depth was 30μm and the constriction gaps were designed to be 60 μm, with at least 30 μm spacing between the respective electrode edge and constriction tip along the y-axis (i.e., space for flow passage was at least 5-times the size of RBCs), as obtained using a stereomicroscope for alignment of the PDMS channel to electrodes on the glass chip (<± 5 μm misalignment). The likelihood of channel clogging due to trapping of sample particles between the constriction tip and electrode edge was lowered by using a sheath flow to focus the sample particles close to the channel wall neighboring the constriction. Since aggregates of PDMS posed a bigger risk to clogging, we included an array of posts just before the region of sample entry into the microchannel to filter such aggregates that were in the several ten-micron size range, thereby avoiding their transport to the constricted region of the channel for preventing clogging. The microfluidic device was assembled into a 3D printed holder (FDM) with an embedded custom PCB (Printed Circuit Board) for the required electrical connections to the electrodes.

4.3.2 Microfluidic device operation

Syringe pumps (Nemesys, Cetoni GmbH) were used for driving the sample and focusing flow through the chip. Electric fields were applied using a signal generator (33220A LXI, Agilent technologies) coupled to an amplifier (A400DI, FLC Electronics) to deliver the final peak-to-peak voltage (~60 V_{pp}). Dielectrophoretic deflection of cells was imaged on an inverted microscope (Axio Observer 7, Zeiss) with a CMOS camera (Orca flash 4.0 V2, Hamamatsu). Post processing of the images was accomplished with an open-source image processing software (Fiji, National Institute of Health).

4.3.3 Biological sample preparation

The biological samples for these studies were a stock solution of human red blood cells (hRBCs) (Malaria Lab, University of Virginia) in albumin (HSA, Sigma Aldrich) diluted to a concentration level of 2.25×10^8 cells/ml. The sample was spun down for 5 min at 1000 rpm (5430 centrifuge, Eppendorf) and washed twice with DEP buffer (8% Sucrose, 1% BSA & 1X PBS for the higher media conductivities), so that the net media conductivity could be adjusted to: 17 μS/cm, 150 μS/cm and 525 μS/cm, as per three independent measurements using a conductivity meter (LAQUAtwin, Horiba).

4.3.4 Electric field simulations and fits to the shell dielectric model

Computational Fluid Dynamic (CFD) simulations were conducted for the purpose of device design and optimization, using the COMSOL Multiphysics software (COMSOL Inc.), to simulate field profiles, flow streamlines and particle transport under the force fields. The DEP response of model

RBCs was performed using custom MATLAB code [133, 134], and verified using the MyDEP package [135].

4.4 Results and discussion

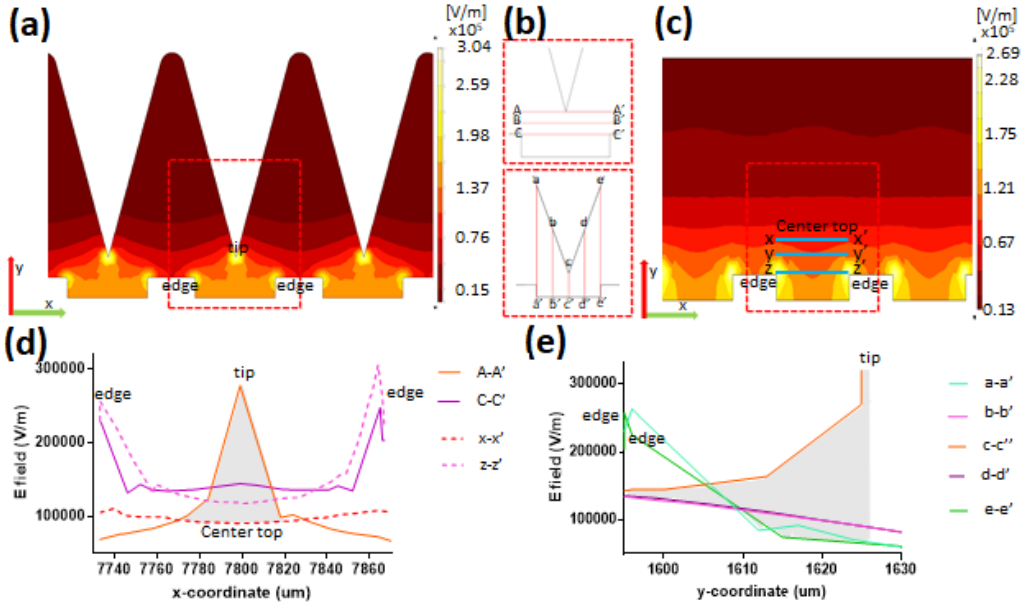

Figure 4.3 2D simulations of the electric field (V/m) profiles for: **A.** constriction channel of Dy-DEP design versus **C.** channel design with electrodes only. The field profiles for the two devices across the probe-lines per **B.** horizontal probe-lines (top), vertical probe-lines (bottom) are shown in **D.** for E-field norm variation in the x-coordinate for the 3D constriction channel: A-A', B-B', C-C' versus on the equivalent straight channel with electrodes: a-a', b-b', c-c'. **E.** E-field norm variation in the y-coordinate, per the inset for the E-field variation on the tip (C-C').

In order to assess the microfluidic device with 3D constrictions energized by planar electrodes, as presented in this work (**Fig. 4.3 A**), we present its comparison to an equivalent device comprising a straight channel with 3D electrodes that has been widely studied for dielectrophoretic deflections in prior work [120, 136], but is difficult to fabricate. Focusing on simulation of the field profiles along the red boxed region of interest in **Fig. 4.3 A** and **4.3 C,** we plot the field profiles for the two device types across the indicated probe-lines of Fig. **4.3 B** to quantify variations along the x-coordinate (**Fig. 4.3 D**) and y-coordinate (**Fig. 4.3 E**). Based on this, it is apparent that the 3D

constriction design presents greater spatial extent of the high field region than obtained for the straight channel design with the electrodes. As a result, the chance for traversing cells to interact with the field non-uniformity is increased at a number of flow streamlines, whereas for the case of the straight channel with electrodes, the E-field profile is strongly damped in the region between the electrodes, which significantly reduces the effective area for high field. The plot of the E-field norm variation along the y-coordinate shows that the effect of the high E-field due to the constriction tip is expanded to cover the area between electrodes in the y axis. Hence, coupling of the 3D constriction with the planar electrode leads to an enhanced region of high field in **x** and **y** directions, so that it is comparable or higher than the extent of the high field region obtained for the straight channel device with 3D electrodes. As a result, we anticipate that cells interact with the field non-uniformity, not only at the constriction tips, but also over a more extended area than obtained in the case of the straight channel with electrodes.

Comparison of the 3D field profiles of the design in current work of 3D constrictions coupled to planar electrodes (Fig. 4.4a) versus the straight channel design with 3D electrodes (Fig. 4.4 b) further illustrates the above inference. It is apparent that the design of the current work interacts with the field from the planar electrodes to result in a 3D spatial field distribution across the device depth, with an enhanced E-field magnitude versus that created by 3D electrodes in the straight channel. Furthermore, since the 3D constrictions are spread over an array of wide area, a wider microchannel with a higher sample volume can be used and cells over a larger number of fluid streamlines are able to interact with the field non-uniformity, thereby enhancing the throughput of cells analyzed (i.e., higher analyzed cells per min).

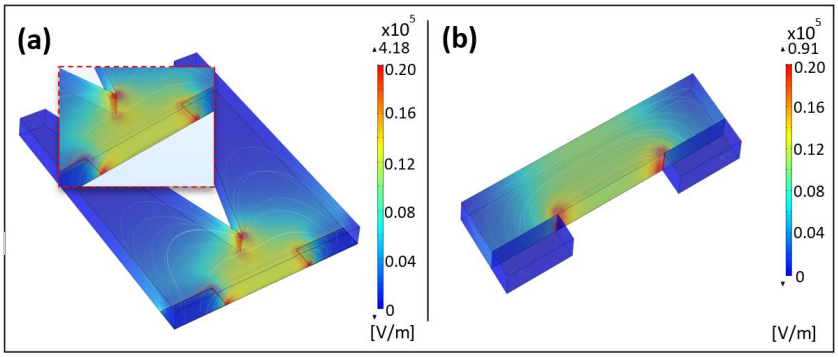

Figure 4.4. 3D simulations of the Electric field norm (V/m) distribution in: **A.** Dy-DEP design with 3D constrictions coupled to planar electrodes (see inset for 3D E-field distribution between the planar electrodes and the constriction tip) compared to **B.** the equivalent straight channel design with 3D electrodes. The colors are adjusted for equivalent field levels to present the relative differences in field extent, but **A.** extends to a higher level of maximum field versus **B.**

With the finalized device design, simulations were performed to optimize flow rates and number of constrictions by tracking the movement of particles under the force fields in the device of the current work (**Fig. 4.5**.). Simulations (COMSOL) were used to determine the minimum ratio of sheath flow to sample flow required to focus cells to within 100 μm of the upper channel wall, so that upon further focusing in the constriction region due to enhanced velocity, the particles would pass along streamlines that were within a distance of ~20 μm from the constriction tip. This distance to set the limit for particle streamline from the constriction tip was based on the simulated high field region that is indicated as shaded in Fig. **4.5 B** and its inset. Using this minimum ratio of sheath flow to sample flow of 3, the maximum net flow rate level at which cells would continue to be deflected from their streamlines by dielectrophoresis was experimentally determined to be 1.68 μL/min. This sheath flow to sample flow level and the net flow rate level were subsequently used to study the dynamic dielectrophoretic deflection of human red blood cells (RBCs) at various media conductivity and frequency conditions of the applied field. As an example, the separation of RBCs (colored red in **Fig. 4.5** and approximated to model cell of 5 μm radius) from platelets

(colored blue in Fig. 4.5 and approximated to model cells of 1.8 μm radius) can be used to optimize the device design and operating conditions. In the absence of applied voltage (Fig. 4.5a), there is no separation of streamlines and the respective cells appear further scattered in the subsequent flow expansion region. On the other hand, in the presence of an applied voltage (Fig. 4.5b; 50 V_{pp} at 100 kHz within media of conductivity of 550 μS/cm), the far higher nDEP level on RBCs *versus* that on platelets causes a separation of their respective streamlines to a spatial extent of ~100 μm, with a further spatial separation to ~755 μm within the subsequent flow expansion region. Furthermore, it is apparent that the cells are progressively deflected over each of the consecutive field non-uniformities, for up to 16 constrictions.

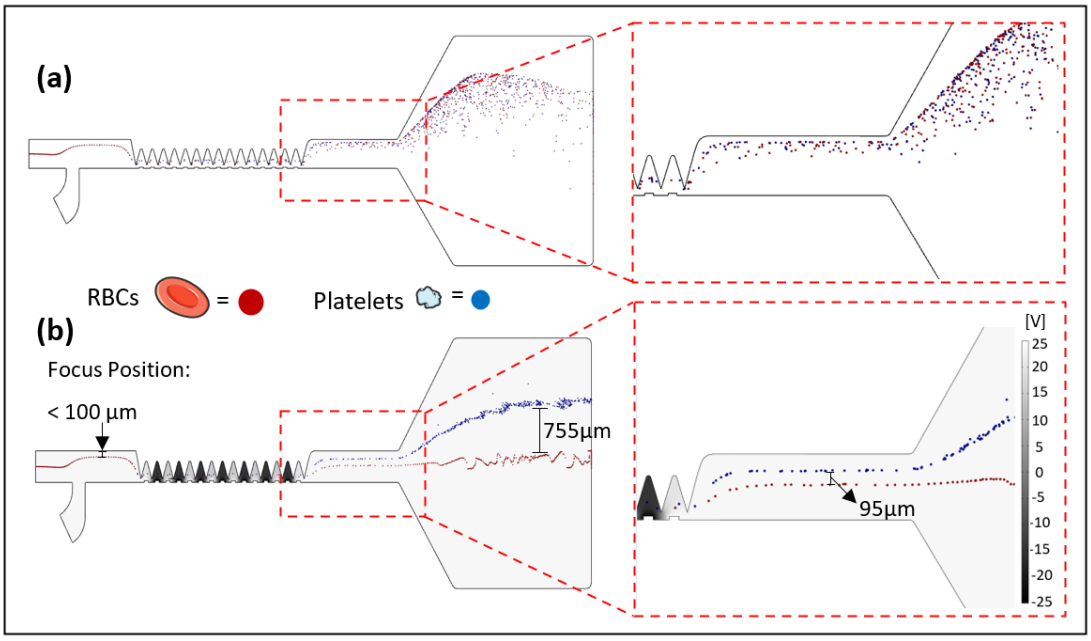

Figure 4.5 Particle tracing simulations with model cell types for optimizing design and operating conditions for the separation of RBCs (red of 5 μm) versus platelets (blue of 1.8 μm). **A.** No applied Voltage (no DEP) causes the undeflected cells to be scattered at the outlet (right inset). **B.** Applied Voltage (50 V_{pp}) shows significantly higher nDEP deflection of RBCs versus platelets (at 100 kHz with a media conductivity of 550 μS/cm), causing spatial separation in their flow streamlines (per inset).

4.4.1 Measurement of flow trajectories of dielectrophoretic deflected RBCs

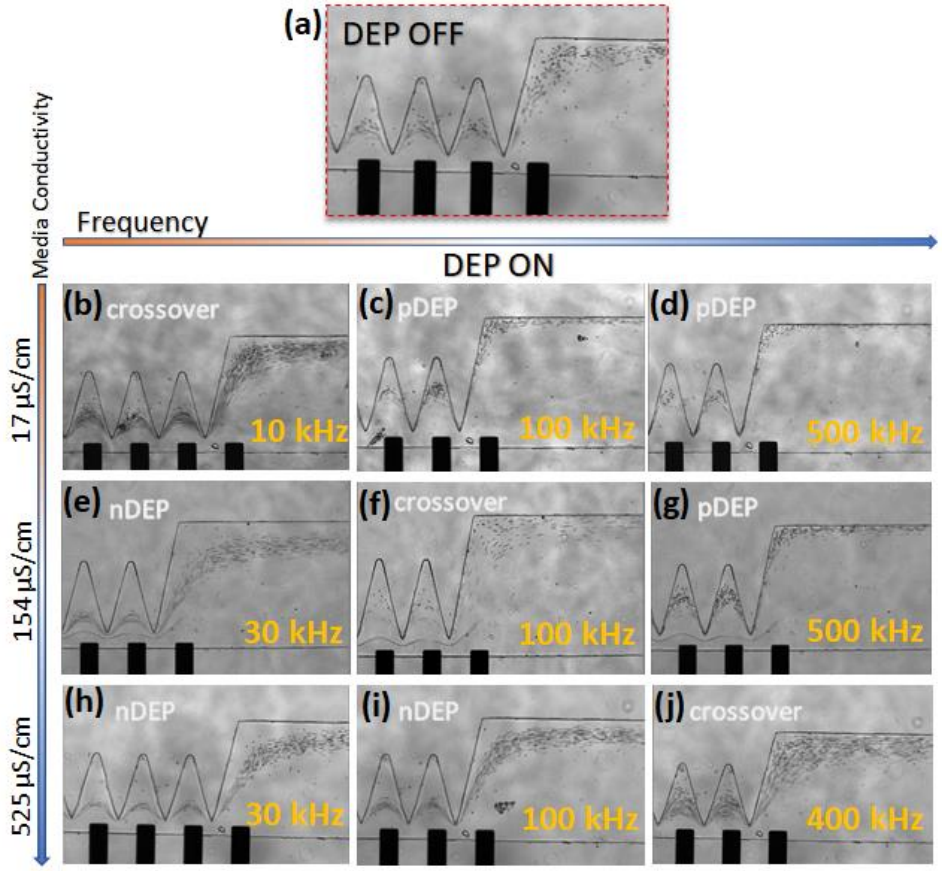

Figure 4.6 Effect of dielectrophoretic translation on flow trajectories of human red blood cells (hRBCs) at a sample concentration of 2.25×10^8 cells/mL at a total flow rate of 1.68 µL/min (sample flow of 0.48 µL/min plus focusing sheath flow of 1.2 µL/min) for measurement at a throughput of $1.1x10^5$ cells/min.: **A.** No applied voltage**. (B-J)** with applied voltages of ~60 V_{pp} across 150 µm spaced electrodes at indicated media conductivities (vertical axis) and frequencies (horizontal axis), with the DEP level and direction indicated by labels.

To demonstrate the ability of the device to easily distinguish DEP translation direction and level in a high throughput (large number of cells per minute) and dynamical (high-flow rate) manner based on deflected particle streamlines, we use a sample of human red blood cells (RBCs) obtained from diluted human blood to a starting concentration of: 2.25×10^8 cells/mL. Using a total flow rate 1.68 µL/min, obtained due to sample flow at 0.48 µL/min that is focused using a sheathing flow of 1.2 µL/min, we study the ability to measure dielectrophoretic deflections of varying level

and direction, at a throughput of $1.1x10^5$ cells/min at a voltage of ~60 V_{pp} applied across planar electrodes (spaced 150 μm) over a 10 kHz to 1 MHz frequency range and within media of conductivity levels of 17 μS/cm, 154 μS/cm and 525 μS/cm (**Fig. 4.6**). Based on the broad distribution of RBCs obtained under no field conditions (**Fig. 4.6 A**), pDEP behavior at high frequencies of the applied field (500 kHz) within media of low conductivity (17 μS/cm) causes the RBCs to be focused right at the edge of the channel wall (**Fig. 4.6 D**). As the frequency of applied field is lowered to 100 kHz, the pDEP focusing close to channel wall continues to be apparent **(Fig. 4.6 C**), down to 10 kHz frequency of applied field wherein crossover begins to be apparent based on broader dispersion of cells across streamlines (**Fig. 4.6 B**). At the higher media conductivity of 154 μS/cm, nDEP is apparent at 30 kHz of applied field based on focusing of RBCs away from edge of the channel wall (**Fig. 4.6 E**), whereas crossover is apparent at 100 kHz of applied field based on the dispersed RBC streamlines (**Fig. 4.6 F**) and pDEP is apparent at even higher frequencies of 500 kHz based on focusing of RBCs close to edge of the channel wall (**Fig. 4.6 G**). Finally, at the highest media conductivity used in this work (525 μS/cm), nDEP is apparent at the lower frequencies of 30 kHz (Fig.4.6 h) and 100 kHz (Fig. 4.6 i), based on focusing of RBCs at a critical distance away from edge of the channel wall, right up until a frequency of 400 kHz wherein crossover is apparent based on the dispersed RBC streamlines (Fig. 4.6 j). It is noteworthy that in order for flowing particles to experience significant levels of pDEP trapping due to the electrodes, they would need to traverse in a streamline within 10 μm of the electrode edge in the y-direction, per the simulations of Fig. 4,6 c. This situation is avoided by the sheath flow to focus the sample particles to within ~20 μm from the constriction tip, which places the particles at greater than 10 μm from the electrode edge along the y-axis. Furthermore, when the electrodes are at a frequency corresponding to pDEP behavior, the particles are pulled towards the constriction,

thereby pushing the particles further away from the electrodes to avoid pDEP trapping. When the electrodes are at a frequency corresponding to nDEP behavior, the particles can be deflected closer to the electrodes, but the frequency level used ensures no pDEP trapping at the electrodes. For the case of operating the device at the crossover frequency wherein particle dispersions are at their maximum level, the images in Fig. 4.6 b, 4.6 f and 4.6 j show that particle streamlines are at least 20 μm away from the electrodes, thereby avoiding any significant level of pDEP trapping. Finally, due to the high flow rates used in this study, the time period for pDEP at the electrodes is further reduced to obviate pDEP trapping.

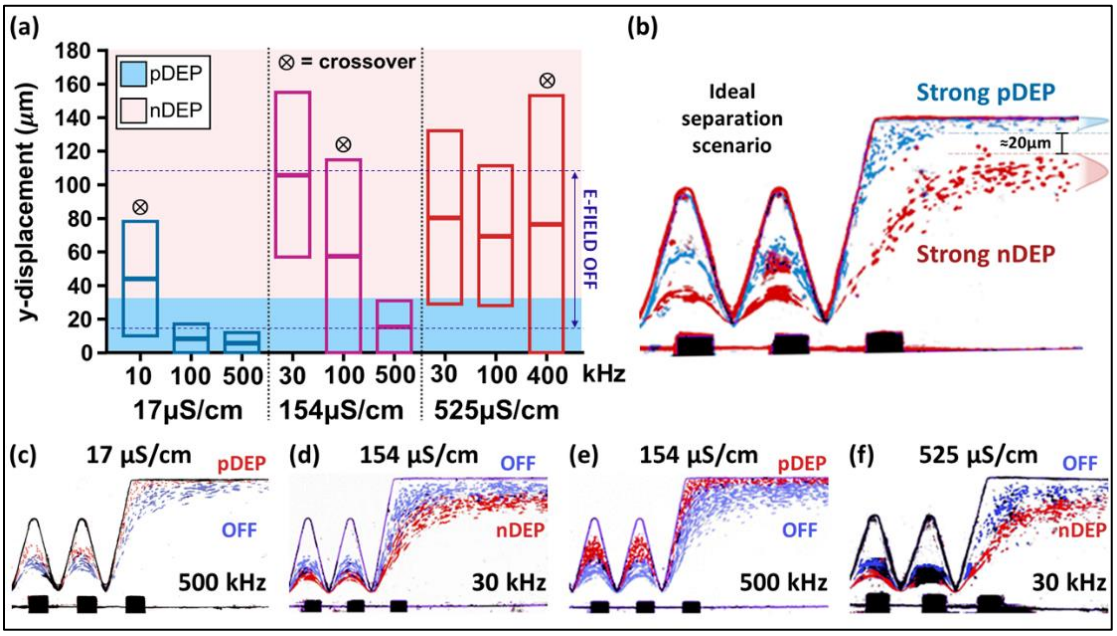

Figure 4.7. Intensity threshold plots obtained from phase contrast microscopy images are used to assess the ability to discern differences in dielectrophoresis level and direction based on the flow streamlines: **A.** summary data box plot with range of histograms in displaced position of traversing RBCs from edge of channel wall (y-direction) under the conditions from Fig 5, including: **B.** pDEP versus nDEP deflection is clearly distinguished based on lateral separations in streamlines of > 20 μm at 154 μS/cm and ~40 μm comparing pDEP at 17 μS/cm to nDEP at 154 μS/cm; **C.** strong pDEP causes focusing of RBCs to within 15 μm of wall edge versus the highly dispersed profile under no DEP; **D.** weak nDEP focuses RBCs at least 60 μm away from wall edge, and **E.** weak pDEP focuses RBCs to within 30 μm off the wall edge, in comparison to the highly dispersed profile under no DEP; **F.** strong nDEP is also distinguished well versus no DEP behavior. For comparison, the displacement range for the FIELD OFF condition is also indicated as an arrow in **A.** (95% confidence level).

To quantify the flow trajectories of RBCs, we applied an image threshold method to assess the ability to distinguish direction of DEP deflection and its relative level based on position of the cells. The summary data of Fig. 6a is a box plot of the histogram range in position of traversing RBCs from edge of channel wall (y-direction) under the conditions investigated within **Fig 4.7** For the ideal case of RBCs deflected under pDEP versus under nDEP, the respective histograms can be clearly distinguished based on lateral separations in streamlines of > 20 μm (**Fig. 4.7 B**). The strong pDEP behavior at media of low conductivity (17 μS/cm) causes the RBCs to be focused to within 15 μm of wall edge versus the highly dispersed profile under no DEP (**Fig. 4.7 C**). At intermediate media conductivity (154 μS/cm), weak nDEP at 30 kHz focuses RBCs to be at least 60 μm away from wall edge (**Fig. 4.7 D**), and weak pDEP at 500 kHz focuses RBCs to within 30 μm of the wall edge (**Fig. 4.7 E**), in comparison to the respective highly dispersed profiles under no DEP. Similarly, at higher media conductivity (525 μS/cm), strong nDEP is also distinguished well versus no DEP behavior. Based on the quantification presented here and the quantitative limits set for displaced RBC streamlines from the channel wall edge (**Appendix: A.2**), we infer that pDEP, nDEP and crossover behavior of single-cells can be discerned based on their deflected streamlines. The crossover frequency levels for the RBCs at the three measured media conductivity levels that is obtained from the current Dy-DEP device are validated by comparing the calculated membrane capacitance (C_{mem}) and dielectrophoretic dispersion versus that obtained in prior work [118, 136], as presented in Appendix **Table A.3** and the computer dispersion in **Fig. A.4**. The computed C_{mem} of 11.7 ± 1.2 mF/m^2 is close to the ~10 mF/m^2 reported in prior work and the crossover values match to the computed dispersion based on established dielectric properties of RBCs using the MyDEP program.

4.5.1 Optimized lateral non-uniformities device results and conclusions

The electrode fabrication steps were simplified using a co-fabrication technique using Field's Metal electrodes. It was validated using 2 different samples of altered electrophysiology: healthy RBCs (h-RBCs) and fixed RBCs (f-RBCs) with glutaraldehyde to modify the RBCs membrane capacitance to obtain different DEP responses at the same frequency and media conductivity conditions. While h-RBCs show strong nDEP at 40kHz, with a mean lateral displacement of 21 μm (p value of 7.1 x 10-5) from their starting position along the channel wall adjoining the field non-uniformity, the crossover frequency was reached at 200kHz, as apparent from a mean lateral displacement of 6.4 μm (p value of 0.003) from their starting position (**Fig. 4.8 A** & **4.8 B**). On the other hand, f-RBCs show nDEP over this measured frequency range, with mean lateral displacement levels of ~40 μm in the 40-200 kHz range. Fixation of RBCs is known to lower ion mobility at the cell membrane to significantly lower the membrane capacitance of f-RBCs, which likely increases their crossover to well-beyond 200 kHz and explains the nDEP observations presented herein. Based on deflected distances determined from the three images for each set, a mean deflection distance and standard deviation was calculated for the f-RBCs and h-RBCs at 40 kHz and at 200 kHz. From the determined mean and standard deviation of the positional data, a normal probability density function was used to compare the normalized deflected events under nDEP and pDEP of h-RBCs and f-RBCs at the respective frequencies, per **Fig. 4.8 A** and **4.8 B.** Based on this, it is clear that while the Gaussian functions for net positions of h-RBCs and f-RBCs strongly overlap at 40 kHz due to their strong nDEP behavior (**Fig. 4.8 B**), the respective Gaussian functions show a high degree of separation at 200 kHz, with h-RBCs continuing to exhibit pDEP and f-RBCs continuing to exhibit strong nDEP. Hence, a collection gate can be set at 34 μm from the channel wall adjoining the orifices for obtaining h-RBCs at a separation purity of 88% on one

side and f-RBCs on the other side at a separation purity of 91.5%. To visually present this data, color correction images of h-RBCs (blue) and f-RBCs (red) from selected frames under DEP deflection were stacked to simulate a heterogeneous sample of h-RBCs and f-RBCs at 40 kHz **Fig. 4.8 D** and 200 kHz **Fig. 4.8 E**. This was used to validate their separation in a mixed sample (50-50) of healthy RBC and fixed RBCs per **Figure 4.9**

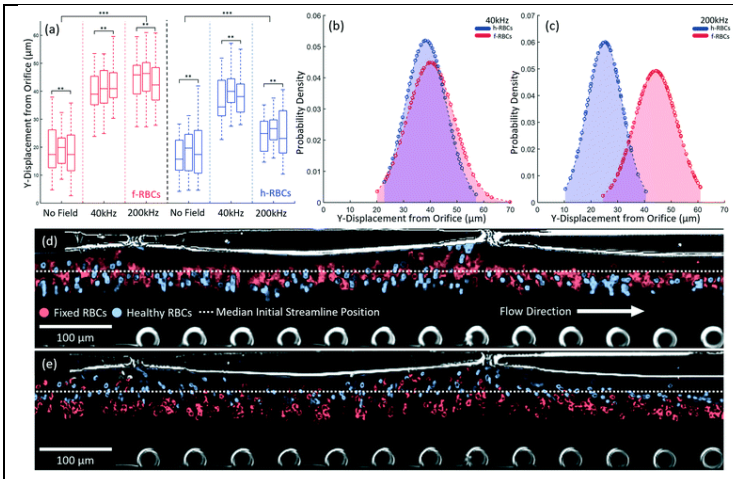

Figure 4.8. Experimental results **A.** RBCs focused in the device with no applied E-field (**B, C, D**) Frequency sweep at low medium conductivity of 17µS/cm) (**E, F, G**) at 154µS/cm (**H, I, J**) at high medium conductivity 525µS/cm [137]

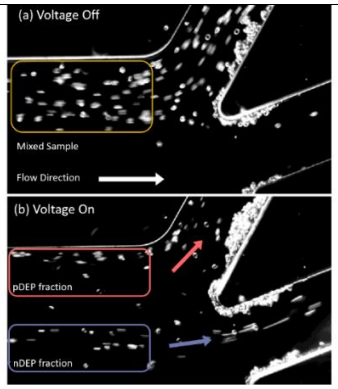

Figure 4.9. Cell streamlines at the collection channels before **A.** and after **B.** DEP separation, shows a low membrane capacitance fraction (presumably f-RBCs) exhibiting nDEP and a high membrane capacitance fraction (presumably h-RBCs) exhibiting pDEP (100 Vpp at 300 kHz, at a sample flow rate of 3.6 µl/min). [137]

4.5 Conclusions

We presented a microfluidic device capable of high throughput dynamical analysis to determine the dielectrophoretic translation level and direction of single-cells over a wide frequency range based on their deflected flow streamlines. Using electric field simulations, the device with 3D insulator constrictions that is energized by a set of planar electrodes is shown to have a spatial extent of field that exceeds the equivalent straight channel device with 3D electrodes. Hence, cells focused along streamlines in the vicinity of the constriction region and traversing through the device at high flow rates have a high likelihood of experiencing significant levels of deflection due to varying levels of pDEP and nDEP, as confirmed by simulations of particle tracking using a set of 16 high field points. Based on measurements of particle deflection on such a device using human red blood cells at a high initial concentration, we show the ability to distinguish between strong nDEP versus strong pDEP; weak nDEP versus no DEP at the crossover frequency; and weak pDEP versus no DEP at the crossover frequency. The quantification ability of the current Dy-DEP device was validated by comparing the obtained membrane capacitance (C_{mem}) and dielectrophoretic dispersion to that obtained within prior the work. Hence, based on the ability to discern dielectrophoresis-induced deflections in cell streamlines at a high flow rate and a high sample concentration, we suggest that the device can be used to determine the dielectrophoretic dispersion of a sample of cells at a high throughput, single-cell sensitivity and with no need for significant sample dilution. It is noteworthy that since each traversing cell is individually displaced based on its electrical phenotype and measured based on the position of its deflected flow streamlines, the reported method does not average across the population and is capable of quantifying the DEP frequency dispersion of single-cells. Furthermore, since cells are focused away from the electrodes

and traverse through the consecutive high-field regions of the device at high flow rate (i.e. just milliseconds at high field points), we suggest that their viability is likely not adversely affected by the field. Future work is focused on validating viability effects on the cells within the device, determining the upper limit of cell concentration for DEP analysis in the device and measuring ability to quantify heterogeneity in the cell capacitance phenotype.

Chapter 5: Integration of sample preparation and monitoring with dielectrophoretic separation

5.1 Introduction

For effective DEP trapping, cells in the biological sample must be transferred into a low conductivity media and the recovered cells need to be transferred back into culture media for storage. To reduce the time that sensitive biological cells spend outside of their optimal cell culture media, we seek to develop an on-chip sample preparation and monitoring system integrated to the DEP cell recovery platform.

The dielectrophoretic trapping force (F_{DEP}) for manipulating flowing cells depends on: **(i)** hydrodynamic radius of the cell (a); **(ii)** the product of the electric field (E) to its spatial non-uniformity (∇E) that is represented as: ∇E^2; and **(iii)** the so-called dielectric contrast, which at low frequency (<10 MHz) depends on the difference between conductivity of cell (σ_{cyto}) and that of the suspending media (σ_m). Based on this, **Fig. 5.1 A** shows that the optimal range of σ_m for strong pDEP is <0.1 S/m and for strong nDEP is >2 S/m, with the interceding region of 0.1-2 S/m serving to enhance contrast or the σ_{cyto} to σ_m difference, for distinguishing between different cell types (**B** vs. **C** in **Fig. 5.1**. In fact, as shown in **Fig. 5.1 B**, a low σ_m level of 0.01 S/m ensures high pDEP, but all cell types show high pDEP, with no ability to distinguish them based on their cytoplasmic conductivity (σ_{cyto}). Hence, by adjusting to an optimal σ_m level (e.g., 0.35 S/m in **Fig. 5.1 C**), cells of differing σ_{cyto} levels can be distinguished from each other based on DEP level and direction. However, this means that the σ_m level needs to be altered for cells from ~1.5 S/m in their culture media at to a level in the 0.05-0.5 S/m range that is tailored based on the type of cells in each sample type from which the separations are needed.

Hence, for selective DEP enrichment of rare cells of interest from heterogeneous samples, there is a need for sample preparation, wherein abundant background cells (e.g., blood cells for biopsies) are removed and conductivity of the sample media is lowered to enhance dielectric contrast for tailoring separations to each sample type.

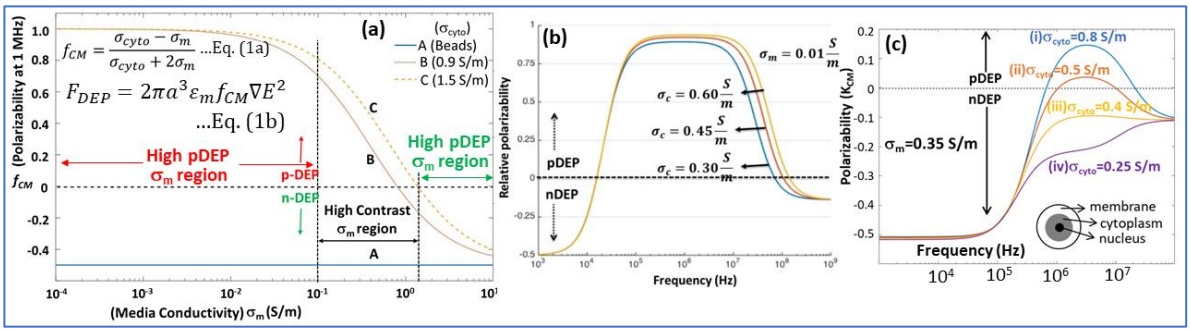

Figure 5.1 A. Most cells show pDEP at σ_m<0.01 S/m and nDEP at σ_m>2 S/m. This is also apparent in the frequency response **B.** Hence an optimal σ_m level is needed to separate cells based on σ_{cyto} levels **C.**

Currently all of this sample preparation is done off-chip, which is problematic since these additional pre- and post-sorting protocols increase the time spent by sensitive cells outside of their culture media. As shown in **Fig. 5.2 A**, in comparison to mouse embryonic fibroblasts in culture media, while after 1 h there is no significant alteration in % cell survival when swapped into 0.1 S/m diluted PBS media that is optimized with additives for the altered osmolarity due to buffer change, the survival falls steadily with time and more steeply with lowering of media conductivity. Furthermore, for embryonic stem cells, this buffer switch causes a drop in fold-expansion of cells with exposure time in the low conductivity media. It is also noteworthy that the proposed on-chip monitoring protocols (see below on details) will improve reproducibility & consistency of sample procedures.

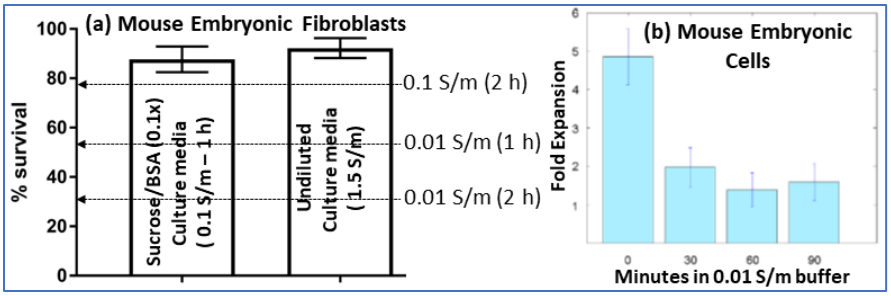

Figure 5.2 Effect of exposure to low conductivity buffers over time on: **A.** % cell survival [138]; **B.** n-fold cell expansion [139]

This highlights the need to conduct the buffer switch in a rapid manner and couple this exercise with optimization protocols to ensure cell survival and maintenance of cell functionality in the DEP buffer. Additionally, the manual operation used in current off-chip protocols reduces system consistency, while dependence on a trained operator raises costs and increases reagent wastage.

We proposed to integrate the developed DEP device with a sample conductivity media dilution stage while keeping the sample of interest focused at the center of the device to decrease sample loss while the sample flows to the DEP sorting step, the proposed device concept is shown in Figure 5.3. As further work, a set of electrodes could be fabricated at the end of the DEP stage to monitor the sample output by performing impedance measurements on chip.

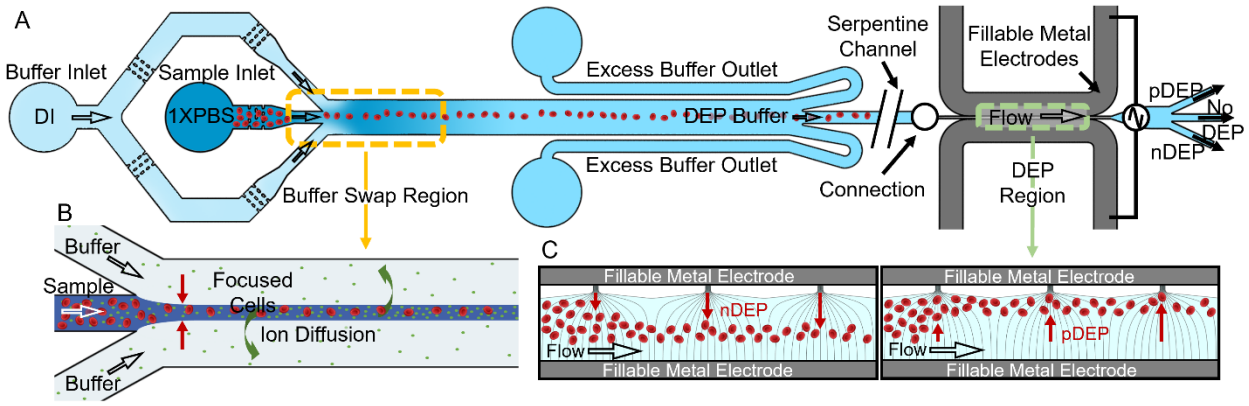

Figure 5.3 Device integration of sample buffer switch stage and DEP sample deflection **A.** CFD simulation of mixing length at inlet **B.** Sample focusing (red) streamlines and sheath flows (gray) at the end of the sample switch stage **C.** Particle tracing simulation to validate sample focusing and **D.** Sample focusing at the of the device.

Diffusion occurs over a mixing length (L_{mix}), per **Fig. 5.4 A**, as defined in Eq. 5 of **Fig. 5.4 B.** Based on this, L_{mix} depends on the Peclet number (Pe) that is defined in **Figure 5.4 B**, the ratio of the square of input sample flow to total net flow after adding the sheathing flow rates, channel width (w), channel height (h) and the convection time (τ_{conv}) that is dependent on the average particle velocity. Each of these factors were varied, initially using simulations to identify the promising candidate design parameters for device fabrication and experimental validation.

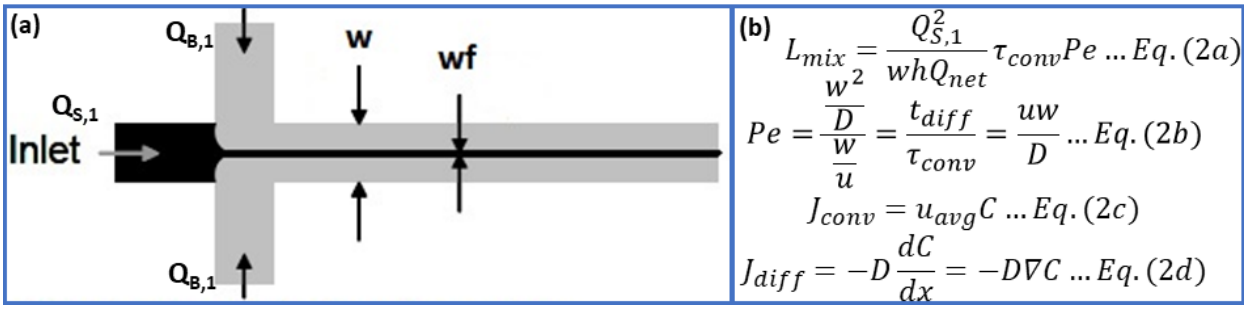

Figure 5.4 A. Design parameters and **B.** equations for flow simulations

The continuity equation (Eq. 5) and Fick's law (Eq. 6) are used to set-up the differential equations that are solved based on the appropriate finite element meshing method.

$$\nabla . J_i + u . \nabla c_i = R_i \text{ (reaction rate = 0)} \quad (5)$$

$$\text{with } J_i = -D_i \nabla c_i \quad (6)$$

Here: J_i stands for diffusion flux, D_i is the diffusion coefficient, c_i is the initial concentration that is defined in the boundary conditions at the inlets, and u is the velocity that is calculated using the creeping/laminar flow module coupled with the transport of diluted species module in COMSOL. Based on this, we simulated the velocity profiles and ion concentration were used to estimate L_{mix} for optimizing particular device geometries and flow conditions.

Microfluidic media dilution strategies from prior reports [140, 141] are likely to also dilute cells

in the sample, while inertial strategies to enhance mixing for media dilution [142] would also alter cell streamlines to cause their flow dispersion and reduce sample collection in the exchanged buffer. Other strategies utilize acoustophoresis [143] or dielectrophoresis [144] for flow focusing of cells in the sample, so that the suspending media can be exchanged by cascaded ion diffusion. However, they are limited by alterations in the respective trapping force as a function of exchanged media properties [145] and by the increasing cell-to-cell interactions that occur during focusing of concentrated samples. Also, media exchange in these prior strategies was not integrated in-line to downstream operations, such as DEP, which requires specific ranges of flow rate and media conductivity. Instead, we present a single-stage microfluidic strategy (**Fig. 5.3** and **Appendix A.5**) of small footprint (~4 x 2 cm) that couples flow focusing of cells at the center of a straight channel by tangential flows, with ion diffusion at the edges for enabling on-chip media swap for cells from their culture media to ~100-fold lower conductivity media, while adjusting hydrodynamic resistances at the outlet to minimize flow dispersion for collecting majority of cells from the original biological sample and to modulate the flow rate of cells for enabling in-line DEP deflection downstream. Specifically, red blood cells (RBCs) in the input sample (3.3×10^8 cells/mL) are transferred from a media of 1x PBS (phosphate buffered saline) at ~15000 μS/cm conductivity to a buffer with a media conductivity of ~175 μS/cm and the collected sample exhibits minimal dilution (10^8 cells/mL). In this manner, the media conductivity and flow rate of the collected sample are validated to support in-line negative dielectrophoresis (nDEP) at 30 kHz and positive dielectrophoresis (pDEP) at 1 MHz, by using a set of sequential field non-uniformities in the downstream microchannel for flowthrough DEP [146]. Based on this platform, we envision the ability for on-chip automation [147] and integration of sample preparation in-line with DEP sorting to reduce user intervention and stress on cells, as well as for monitoring of cell media

properties, as well as their numbers, velocity, viability and position in the microchannel, as may be required for tailoring DEP separations for different degrees of cellular heterogeneity within the biological sample of interest.

5.2 Experimental Methods

5.2.1 Device Design

A single-layer PDMS microfluidic device was designed to focus the cell streamline at the device inlet via high flow rate tangential flows containing the DEP buffer. This promotes diffusion-based ion mixing across the respective flow streams of the long straight channel (2 cm in length, 1500 μm in width and 50 μm in depth) that is designed for high laminarity to minimize dispersion of cell streamlines, so that cells can be exchanged from the sample media of high conductivity to that of low conductivity media, as required for downstream DEP deflection (**Fig. 5.3**). The collection region for cells in the swapped low conductivity buffer consists of a central sample outlet that is designed with a hydrodynamic resistance that is much higher than that of the two flanking excess buffer outlets, as accomplished by the central outlet leading to a serpentine channel that is 99 times the length of the two flanking excess buffer outlets. This reduces the velocity and flow dispersion of the cell streamlines exiting at the channel center from the buffer swap stage, while ensuring that the excess buffer is removed at high flow rate from the flanking outlets. In this manner, the cells in the sample can be collected without dilution and at modulated velocities that support downstream DEP deflection at the desired separation throughput. The collected cells after the buffer swap pass onwards from the serpentine channel to an adjoining microchannel for in-line dynamic DEP at the same flow rate, through connective tubing between the sample outlet of the buffer swap stage and the sample inlet of the DEP stage. Since the central outlet from the buffer swap region has a serpentine length (~85 cm) that is much greater than that of the DEP region

(~1.5 cm), the latter region does not have a significant upstream effect on the hydrodynamic resistance balance from the buffer swap region. The media conductivity after the buffer swap stage was determined using a conductivity meter based on three independent runs for swapping cells from 1x PBS to the low conductivity buffer required for DEP.

5.2.2 Device Simulation

The device design and flow conditions were optimized using COMSOL Multiphysics® 5.6 package. We used the microfluidics module to solve the Navier-Stokes equations for the laminar regime. We specified the volumetric flow rates of the inlets to 0.99 µl/s for the sheath flow and 0.01 µl/s for the sample. The boundary conditions of non-slip for the wall and atmospheric pressure in the outlets were applied. Concentration profiles were obtained by coupling the fluid flow module with the transport of diluted species interface to solve Fick's Law diffusion equation. The initial sample concentration was set to 157mM of Na^+ (the most abundant ion in Phosphate Buffer Saline (PBS)) and close to 0 (0.0001 mM) to simulate deionized water in the sheath flows. Concentration profiles were plotted using probe lines at different locations in the device after the sheath and sample flow joined in the main channel.

5.2.3 Device Fabrication

The device was fabricated using standard single layer patterning of SU-8 resist by photolithography on 4" silicon wafer to a 50 µm depth. A 5:1 PDMS base to PDMS crosslinker was used to micromold using the SU-8 pattern as a master mold. The PDMS and the SU8 master were cured at 60°C for 12 hours, followed by demolding and oxygen plasma bonding of the released PDMS channel layer to a glass slide. Another PDMS channel layer with the pattern for the dynamic DEP device was fabricated in a similar manner and bonded to the same glass slide. Field's metal (vendor) was filled into the so-called electrode channels of the DEP device that

adjoin the sample channel, with the device was submerged in a 65 °C water bath to maintain Field's metal as a liquid. After electrode channel filling, the chip was cooled to room temperature to solidify the liquid metal and fabricate three-dimensional side wall electrodes across the sample channel for creating sequential field non-uniformities to initiate DEP.

5.2.4 Microfluidic Operation

Red blood cells (RBCs) from stock solution of blood type A+ human RBCs (Valley Biomedical, Winchester, VA) were suspended in RPMI 1640 HEPES (Sigma Aldrich, St. Louis, MO), supplemented with 0.5% Albumax II Lipid-Rich BSA (Sigma) and 50mg/L hypoxanthine (Thermo Fisher Scientific) for storage and dilution, as needed. This RBC sample at a concentration level of 3.88×10^8 cells/mL in 1X PBS was swapped into a media of lower conductivity by using tangential flow of a media composed of 8% sucrose in DI water. A syringe pump and a pressure microfluidic flow controller were used to drive the sample and buffer/focus flows, respectively. A flow rate sensor coupled with the microfluidic flow controller was used to monitor the exiting sample flow rate. The sample media conductivity prior to buffer swap and after the buffer swap was measured with a conductivity meter (LAQUAtwin, Horiba) after periodic collection. An AC function generator integrated with a high frequency amplifier was used to deliver 80 V_{pp} to the electrodes for initiating DEP over the 30 kHz to 1 MHz range [148], under dynamic flow conditions. Cell streamlines in the microchannel were imaged within the buffer swap and DEP stages of the chip using a CMOS camera connected to an inverted microscope (Zeiss Observer). The output RBC sample from the buffer swap stage was routed for in-line observation of DEP response at the same flow rate and media conductivity conditions.

5.3 Results

5.3.1 Optimizing the Mixing Length for Buffer Swap

The chief design challenge is ensuring a sufficient mixing length for dilution of ions in the sample media to the media conductivity required for DEP, by diffusion of ions from sample to the adjoining tangential flows, while reducing flow dispersion of focused cells from the sample streamline into the tangential flow streamlines that can cause sample loss into the excess buffer outlet. For this purpose, computational fluid dynamic simulations of the design were performed using COMSOL to parametrize the channel geometry (length, width, and architecture) and flow rates to ensure sufficient time for ions to diffuse away from the sample media into the tangential flow streamlines, while maintaining the focused cell streamline at the channel center with minimal dispersion. Based on simulated concentration profiles (**Fig. 5.5 A & B**) and flow streamlines (**Fig. 5.5 C**), the equilibration of ion concentration to levels of 5 mol/m^3 is apparent over the channel width, onward from a diffusion length of 3000 μm from the sample input interface to the tangential flow. Table 1 summarizes the flow rate and the sample media conditions prior to and after the buffer swap stage. Based on this, the media conductivity level prior to the buffer swap stage of: 14150 ± 21 μS/cm (3 independent measurements) can be diluted ~100-fold after the buffer swap stage to: 173.3 ± 1.7 μS/cm (3 independent measurements), using ~200-fold higher flow rate for the sheathing flow (~129 μL/min) versus the sample flow (0.6 μL/min). The resulting outlet from the buffer swap stage is optimized for minimal loss of cells (~10^8 cell/mL in collected sample) and has a flow rate of 1.8 μL/min, which will be validated subsequently for their DEP behavior.

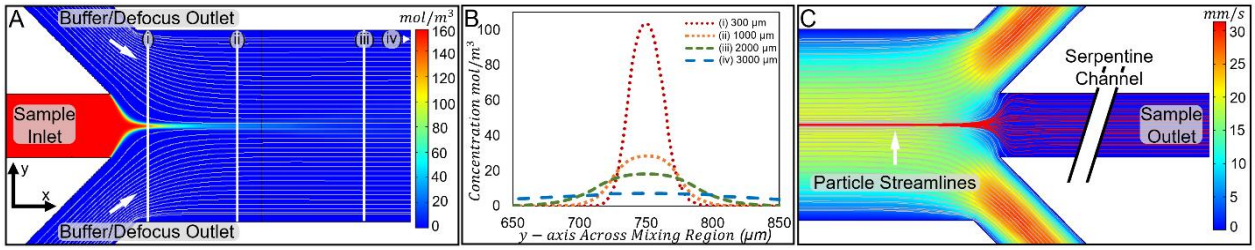

Figure 5.5 Simulations of the buffer swap stage to show: **A**. ion concentration profiles due to diffusion from sample media to tangential flow media. **B.** ion concentration profiles across width of the microchannel along progressive mixing lengths from sample inlet: (i) 300 μm, (ii) 1000 μm, (iii) 2000 μm, and (iv) 3000 μm, per lines in A. **C.** streamlines for cells (red) and buffer (shaded) show differences in flow velocity of the central versus flanking outlets from the buffer swap stage, due to the excess hydrodynamic resistance from the serpentine channel after the central outlet.

Table 5.1 Flow rate and media conductivity at the inlet and outlet of the buffer swap stage. The last row of the buffer conductivity is the average and standard deviation of n=3 measurements.

Flow rate (μL/min)			Buffer Conductivity (μS/cm)	
Sample Inlet	Sheath Inlet	Sample Outlet	Initial	Final
0.6	129	1.8	14150	173
0.6	130.2	1.8	14180	177
0.6	130.2	1.8	14130	176
Collected sample ~10^8 cells/mL			Mean + SD (n=3)	
			14153±21	175.3±1.7

5.3.2 Optimizing outlet hydrodynamic resistance for reducing sample loss

Flow dispersion of the focused cell streamline over this minimum required mixing length was simulated using the particle tracing module, so that the flow conditions can be optimized to enable ion diffusion, while maintaining a low Stokes number (<0.1) to ensure that the particles follow their flow streamlines (**Fig. 5.5 C**). First, the flow rate ratios (tangential to sample flow rate) and width of the buffer swap region are designed to ensure that the focused streamline just exceeds the

size of individual cells in the sample, so that the cell streamline at the channel center maintains laminarity and does not cross streamlines under the tangential flow that is used to promote ion diffusion. Second, to ensure that the cells follow the streamline towards the central collection outlet rather than exhibiting deviation into the flanking outlets that are designed for collection of excess buffers, the hydrodynamic resistance for each outlet branch was modulated. Specifically, the outlet from the central collection region leads to a serpentine channel of 99 times greater length versus that of the flanking channels, thereby vastly increasing the hydrodynamic resistance of the central outlet versus the flanking channels. Hence, the net flow rate of the focused cell streamline is reduced at the outlet, while excess buffer from ion diffusion to cause the media conductivity alteration can be removed at high flow rate through the flanking channels (see flow velocity profiles of central versus flanking outlets in **Fig. 5.5 C**). As a result, the cell streamline passes with minimal flow dispersion for collection at the central outlet, at a modulated flow rate (only 3-fold higher than input sample flow rate) that supports dielectrophoretic deflection. The results (**Table 5.1**) confirm that about a third of the cells in the input sample were collected, as verified by hemocytometer runs on regularly drawn samples, thereby confirming minimal sample loss. The device overview (**Fig. 5.6 A**) shows that the focused cells entering the buffer swap region (**Fig 5.6 (i)**) retain their focus across the mixing length, to enter the central collection channel (**Fig. 5.6 (ii)**) with minimal cell loss due to flow defocusing

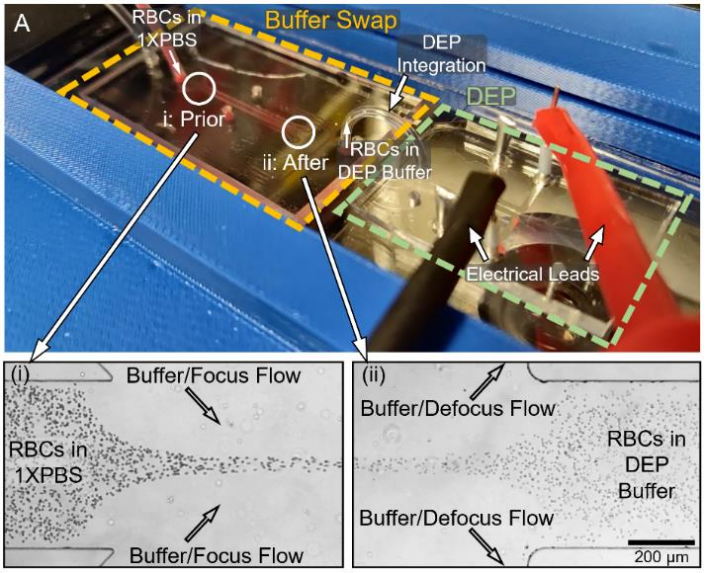

Figure 5.6. A. Setup for the buffer swap stage connected to the DEP stage. Microscope images of: **(i)** RBCs suspended in 1x PBS (14150 µS/cm) entering the buffer swap region at 0.6 µL/min; and **(ii)** exiting as RBCs in the swapped buffer (173 µS/cm) at 1.8 µL/min.

5.3.3 Validation for inline dielectrophoretic deflection

Based on this optimized design for the buffer swap, the measured outlet flow rates (~1.8 µL/min) and diluted media conductivities (~175 µS/cm) (**Table 5.1**) are validated to establish the ability to cause in-line dielectrophoresis, per the flow schematic of the device (**Fig. 5.7 A**) and images of the field non-uniformity (**Fig. 5.7 B**) and 3D structure of the electrode interface with the sample channel (**Fig 5.7 C**). Per the comparison before (**Fig. 5.8 A**) and after the electric field at 30 kHz (Fig. 5.8 B), nDEP is apparent based on translation of the cell streamline away from the high field region (see arrows in **Fig. 5.8 B**). Similarly, after the electric field at 1 MHz (**Fig. 5.8 C**), pDEP is apparent based on translation of the cell streamline towards the high field region (see arrows). It is noteworthy that the current device lacks a tangential flow after the buffer swap stage to focus the cells with respect to the field non-uniformity for enabling sequential DEP deflection. Hence,

the nDEP and pDEP deflection are not as clearly apparent as in our prior work [149] that used focusing flows, but lacked the buffer swap stage.

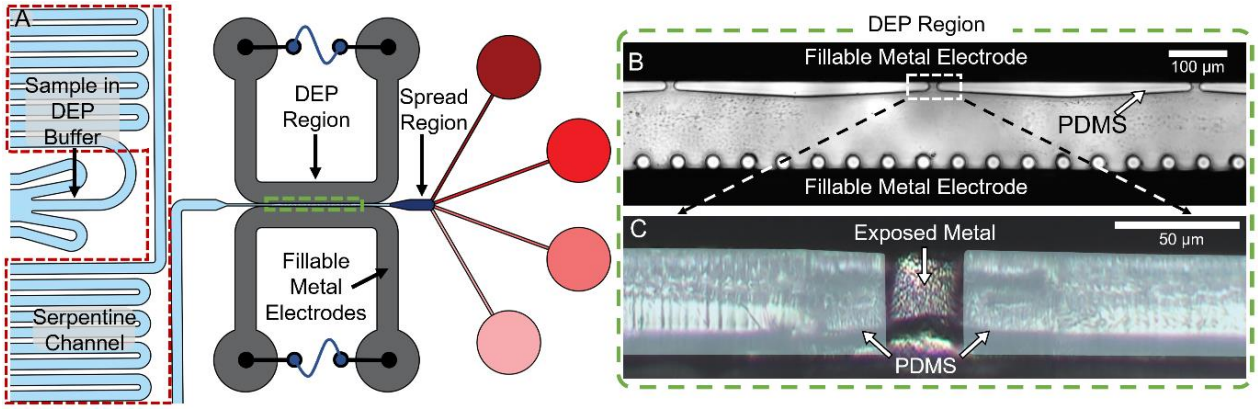

Figure 5.7 A. Connection from buffer swap region to the DEP device region through serpentine channel to modulate hydrodynamic resistance. **B.** Sequential field non-uniformities due to electrodes architecture across sample channel. **C.** Expanded view of the orifice region (dashed white box) showing the 3D electrode interface in the sample channel.

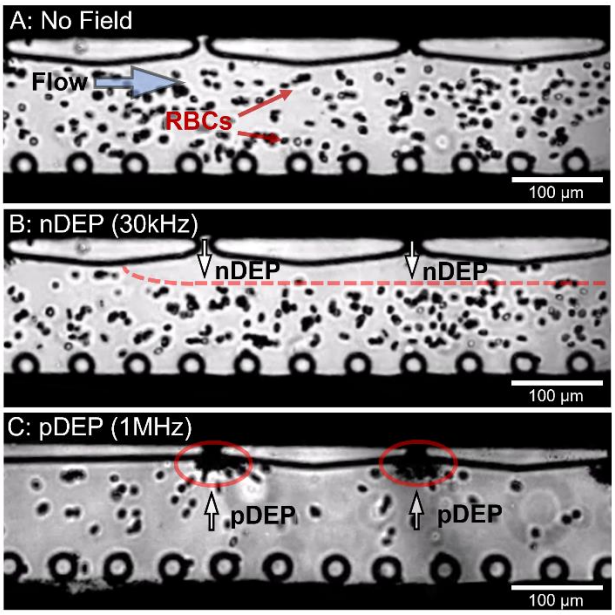

Figure 5.8. Downstream flowthrough dielectrophoresis (DEP) of red blood cells after outflow from the buffer swap stage at 1.8 µL/min in media of ~175 µS/cm conductivity for deflection per streamlines in Fig. 1C. **A.** Initial streamline of dispersed RBCs prior to DEP deflection. **B.** nDEP at 30 kHz for translation away from the high field region (see arrows). **C.** pDEP at 1 MHz for translation towards the high field region (see arrows).

5.4 Conclusions

To address the need for swapping biological cells from their culture media into a media with a conductivity level that is optimized for dielectrophoretic manipulation and vice versa post-dielectrophoretic separation, we present a microfluidic device with a buffer swap stage that is connected in-line to a downstream dielectrophoretic stage. The microfluidic design and flow conditions were optimized using flow and particle tracing simulations for enabling ion diffusion from sample stream into tangential flows, while appropriately increasing the hydrodynamic resistance of the outlet collection channel versus that of the flanking excess buffer outlet channels, to minimize the flow dispersion of cells to enhance their collection and modulate their flow rate to support downstream DEP. As a result, RBCs entering the buffer swap stage at of 3.88×10^8 cells/ml at 0.6 μl/min in 1X PBS media (14150 μS/cm) can be diluted ~100-fold in media conductivity after the buffer swap stage (~175 μS/cm), using ~200-fold higher flow rate for the sheathing flow (~129 μl/min) versus the sample flow. The sample outlet from the buffer swap stage with $\sim 10^8$ cells/mL has a media conductivity of ~175 μS/cm and a flow rate of 1.8 μl/min, which is validated in-line for downstream nDEP at 30 kHz and pDEP at 1 MHz. Follow-up work will seek to integrate the buffer swap stage on a single chip, prior to and after DEP, and include inline monitoring to characterize the outlet sample media conductivity, cell numbers, cell velocity, and cell viability, and the position of their streamlines for enabling effective DEP separations

There is some sample loss due to the pressure imbalance that is produced by connecting the DEP stage as a separate module leading to approximately a third of sample loss. To optimize the device resistance, an integrated device approach where the hydrodynamic resistances in the BSD outlet stage are optimized for a downstream DEP section while reducing the sample linear velocities,

thus the particles drag force don't overcome the DEP force. As it was mentioned before, DEP deflection is less effective without sample focusing (due to its limited electric field extent) after the BSD stage. Therefore, a fully integrated device has to take into account the flow focusing in the DEP stage in order to improve the hydrodynamic balance upstream to prevent sample loss in the BSD section while keeping the sample focused to allow sample media diffusion through the less conductive focusing flows and effectively achieve a less conductive sample medium for DEP deflection downstream.

For monolithically integrate the BSD section to the DEP deflection section it is necessary to optimize the hydrodynamic resistance between focusing flows in BSD section and the sample flow; considering the extra length the DEP section adds to the system. Therefore, affecting the upstream resistance that could lead to even greater sample dispersion (sample loss) at the BSD outlets. In Addition, we need to improve sample focusing downstream to enhance the sample interaction with the high field points produced by the sequential non-uniformities in the DEP section. Adding focusing flows also translate in a resistance increase of the sample flow due to the constraining effect the focusing flow (of flows) exert into the sample flow streamlines. Thus, it is important to establish a dynamic fluid flow operational range for the downstream sheath flow (or sheath flows) that push the samples close enough to the high electric field points while maintaining minimum sample dispersion in the BSD section upstream.

To design such devices a set of CFD simulations were done to optimize all these variables while decreasing sample loss and slowing the sample linear velocity prior to the DEP section to avoid that the particles drag force overcome the DEP deflection force as it shown in Figure 5.9

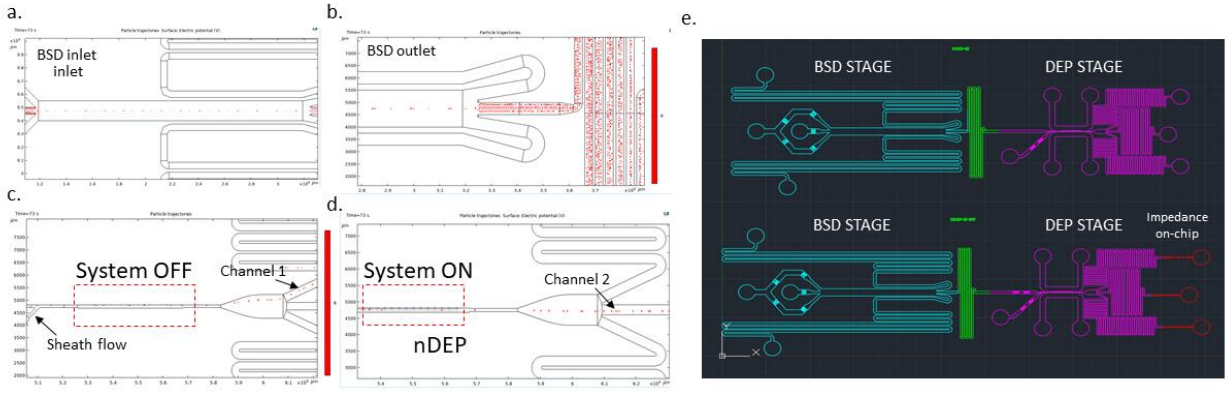

Figure 5.9 CFD simulations for integrated device optimization. **A.** BSD section sample focusing conditions as previously reported. **B.** BSD outlet section showing no particles dispersion. (c) Downstream DEP section with focusing sheath flow with no applied voltage (NO DEP). **D.** same conditions as **C.** with applied 80 Vpp showing nDEP deflection in outlet channel 2. **E.** optimized device mask top view for nDEP deflection.

To validate our device design, we ran RBCs with in integrated BSD plus DEP device and varied the focusing flow in the downstream DEP section to see the effect upstream for sample dispersion and changed the focusing flows in the BSD section to establish how wide the focused sample can be before starting to lose sample on the lateral channels as shown in Figure 5.10.

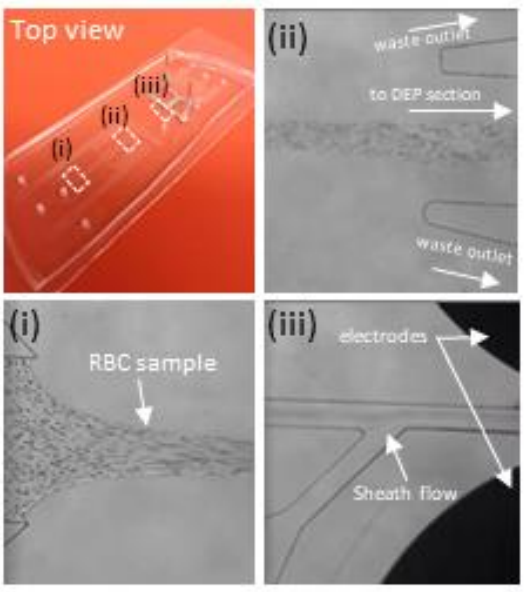

Figure 5.10 Integrated Buffer Swap device with DEP section top view. **(i)** RBCs focused in the BSD section inlet. **(ii)** RBC sample flow still focused in the BSD section outlet with no apparent sample dispersion and **(iii)** Downstream DEP section sheath flow at same BSD conditions.

We validated the device hydrodynamic resistance balance using the previously reported BSD operation conditions and varying the downstream sheath flow (DEP section) from 0.03 μl/s to 0.1 μl/s and didn't observe sample loss while running the experiment with the tested conditions, demonstrating that the new integrated design has significantly improved our prior work by decreasing sample dispersion in the BSD section therefore reducing sample loss in our integrated design. Further work is needed to validate sample conductivities off-chip and nDEP deflection of RBCs, before integrating in-line monitoring of media conductivity and impedance measurement of different electric footprint samples as mentioned in the future work section of this dissertation

Conclusion

In this dissertation a set of devices were designed and fabricated for different experimental applications for either sample characterization, or separation of different biological samples of interest by exploiting their biomechanical properties as it was shown in chapter 2, with an indirect method of assessing human islets rigidity changes during co-culturing time with adipose derived stem cells (ADSC). Our biomechanical method is in principle nondestructive for human islets and we identified a biomechanical trend in h-islet reorganization during ADSC co-culture likely due to their basement membrane remodeling that led to stiffer islets of smaller area that exhibit tighter spreads in their bypass pressure versus size plots. This subpopulation of h-islets that can be identified based on their distinct biomechanical opacity. This metric can potentially be applied to quantify and separate the fraction of h-islet aggregates that have reorganized after ADSC co-culture in the future.

In chapter 3, a DLD device was designed with in-line quantification (on-chip cytometry) of displaced samples and ziz-zag samples. We enriched macrophage subpopulations for a LPS treated macrophages vs control that possess a wide size distribution. This integrated DLD separation with on-chip cytometry device was applied for size-based enrichment of macrophage subpopulations with high degrees of activation. We benchmarked our on-chip data with impedance off-chip data and obtained very similar results. In-line quantification of separated samples is a promising tool for reducing the exposure time of cells outside their ideal culture conditions, it saves time in centrifugation and washing steps required to quantify cells by common methods and mitigates sample loss during the aforementioned steps.

By studying the electric field spatial extent and how to increment the ∇E^2 strength using computational fluid dynamics (CFD), in chapter 4, an array of sharp high field non-uniformities

was designed to create a 3D spatial electric field coupled with standard co-planar electrodes. We demonstrated by CFD and experimental means using samples of RBCs and applying AC-DEP to deflect the sample in the designed microchannel. The sample deflection was quantified by measuring sample streamline shifts using different media conductivities and applied frequencies to attract or repel the sample in a continuous fluid flow mode by exerting DEP force. Further optimization of the device was also shown by using a co-fabrication technique for 3D electrodes that created high electric field points across the whole depth of the device increasing the device throughput and deflecting RBCs and fixed RBCs to different streamlines at the same media conductivity and applied frequency. The samples were collected and quantified by off-chip impedance.

Finally, in chapter 5 a buffer swap device (BSD) was developed for decreasing sample media conductivity while keeping the sample focused for downstream DEP deflection. First, the two separated devices were connected externally to show the device principle and validate that the BSD stage effectively decreased the sample medium conductivity and that DEP deflection is possible as continuous flow operation. Secondly, the BSD section was integrated and optimized monolithically using CFD to minimize sample dispersion in the BSD section outlets to prevent sample loss and to balance the hydrodynamic resistances in the integrated device to prevent that the particles drag force don't overcome the DEP force downstream. A qualitative experiment using RBCs was done to validate the sample loss reduction and the hydrodynamic resistance operational range for the DEP section focusing flow without observable cell dispersion in the BSD section outlets.

Future work

6.1. On-chip electrode integration for monitoring of media conductivity after buffer swap

For on-chip monitoring of the media conductivity after the buffer swap by impedance sensing, the microchannel should be integrated with sidewall electrodes that extend over the channel depth. Current planar electrode strategies have a limited spatial extent over channel depth and are not well suited to detecting media conductions under microfluidic flow focusing or diffusional dilution. Co-fabrication strategies, wherein a liquified metal electrode (Field's metal) is filled in an electrode channel that is self-aligned to a sample channel, is often used to create sidewall electrodes in a microchannel [149]. However, it is challenging to construct sidewall electrodes over a length of ~100 μm, since capillary pinning of the liquid metal to confine its filling to the electrode channel by using post structures at the boundary creates a non-uniform topography, which is not well-suited to impedance sensing. We developed a novel method to restrict the liquid metal filling to the electrode channel by creating a depth confined architecture **(Fig. 6.1)**. The chief design challenge involved optimizing the step height between the electrode and sample channels of the device **(Fig. 6.1 a)** such that the sensing area is maximized while maintaining a uniform topography over the length of the sensing area **(Fig. 6.1 b)**. Based on the experimentally optimized heights of h_1:100 μm and h_2: 50 μm **(Fig. 6.1 c)**, the liquid Field's metal is confined in the electrode channel during the filling step, thereby creating an uninterrupted ~300 μm long sidewall electrode that spans the entire depth (50 μm) of the sample channel,

This creates a sidewall electrode of uniform topography over lengths on the order of ≥100 μm, thereby making it suitable for electrochemical sensing and impedance measurements. The uniform topography also enables facile electrodeposition of gold, which is better suited to long term sensing. The depth confined geometry was fabricated from multilayer SU8 on silicon followed by PDMS micromolding. The mold was

plasma bonded to a glass coverslip and liquid Field's metal was filled into the electrode channels at 65 °C and allowed to solidify at room temperature. In-channel gold electrodeposition on Field's metal was done in a deposition solution comprised of: (34.7mM KAu $(CN)_2$, 0.208 M citric acid, and 0.177 M Ammonium citrate dibasic) followed by in-channel EC sensing of ferrocyanide with cyclic voltammetry wherein Pt counter electrode and Ag/AgCl reference electrodes were submerged in the macro reservoirs at the inlet and outlet of the sample channel. Integration of on-chip media monitoring after buffer swap stage will be validated for dynamic media conductivity monitoring as a function of flow ratios for sample input (Q2) to diluting buffer (Q1).

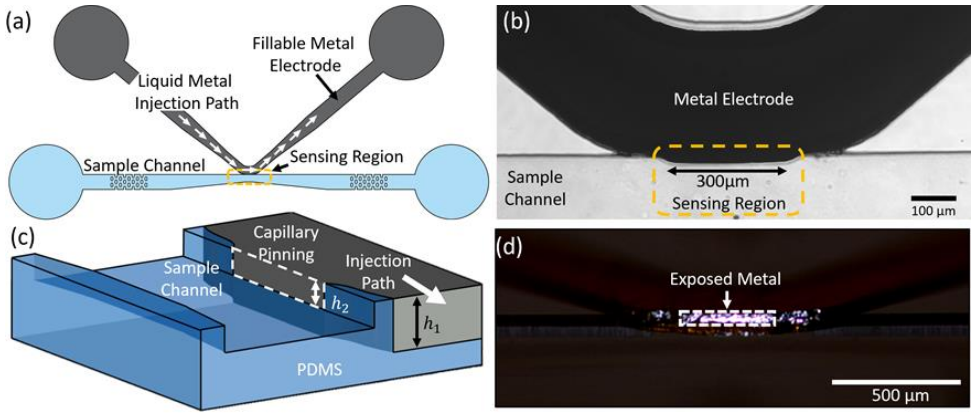

Figure 6.1 (a) Top-down view of the depth confined device (b) Inverted microscope image of sensing region (c) isometric view of the step height and sensing region (d) Crossectional view of the exposed metal sidewall in channel

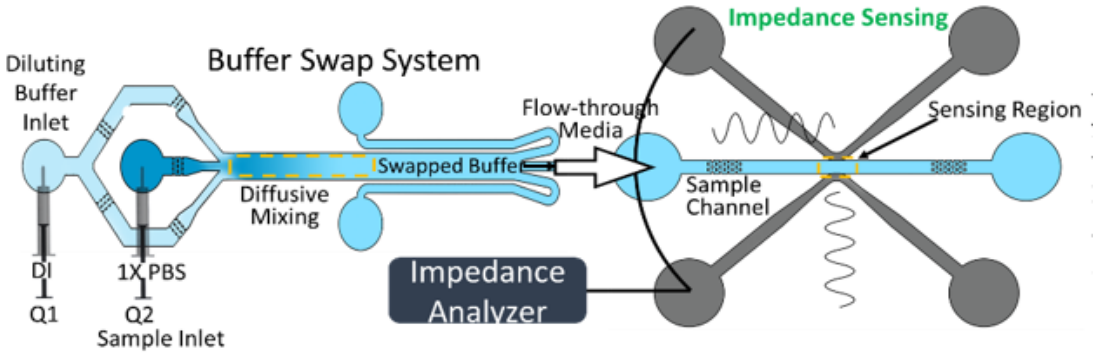

Figure 6.1.2 Integration of on-chip media monitoring after buffer swap stage per validation in (i) for dynamic media conductivity monitoring as a function of flow ratios for sample input (Q2) to diluting buffer (Q1)

6.2 Integrated buffer switch, DEP separation PLUS on-chip monitoring

The next steps are focused on integration of the stages of buffer swap, DEP separation and sample monitoring by impedance cytometry for off-chip validation per **Fig. 6.2**, as elaborated in design stages: (i) without, which is already designed and optimized to reduce sample loss and (ii) with on-chip impedance monitoring.

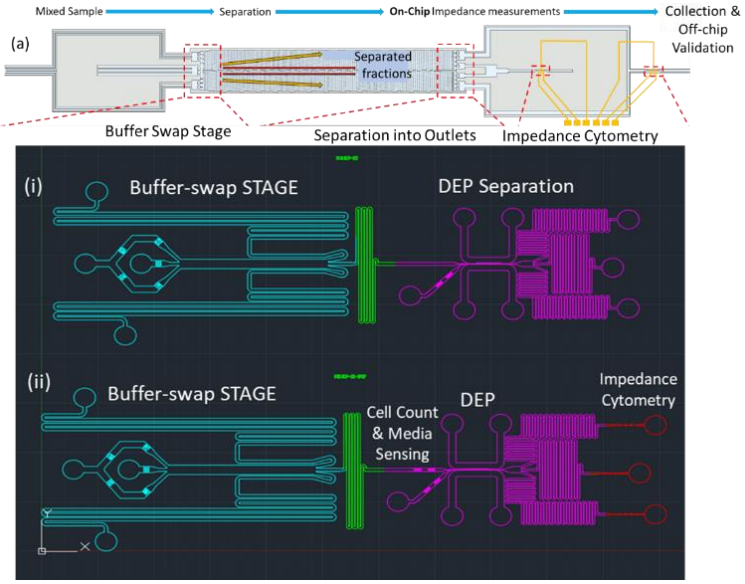

Figure 6.2: (a) Overview of integrated buffer swap, DEP separation and sample monitoring by impedance cytometry for off-chip validation. Design stages: (i) without and (ii) with on-chip monitoring.

Design strategies for follow-up work are underway for integrating the buffer swap stage, DEP separation stage and in-line monitoring operations to characterize the outlet sample media conductivity, cell numbers, cell velocity, cell viability, and the position of cell streamlines for tailoring the sample towards effective DEP separations. More broadly, this strategy can be applied to sensing of flow-controlled processes in microchannels.

List of publications

Journals

- *Multichannel impedance cytometry downstream of microfluidic cell separation by deterministic lateral displacement.*
  Karina Torres-Castro, Javad Jarmoshti, Li Xiao, Aditya Rane, Armita Salahi, Grace Oh, Li Jin, Xudong Li, XuHai Huang, Federica Caselli, Carlos Honrado & Nathan S. Swami. ***(Submitted)***

- *Biophysical quantification of reorganization dynamics of human pancreatic islets during co-culture with adipose-derive stem cells.*
  Karina Torres-Castro, Mohammad S. Azimi, Walter B. Varhue, Carlos Honrado, Shayn M. Pierce & Nathan S. Swami. (***Under peer-review*****)**

- *On-chip microfluidic buffer swap of biological samples in-line with downstream dielectrophoresis*
  XuHai Huang*, **Karina Torres-Castro***, Walter B. Varhue, Aditya Rane, Ahmed Rasin & Nathan S. Swami***.** ***Accepted in ELECTROPHORESIS,*** **Wiley (*2022) DOI:10.1002/els.2021100304***
  *: Equal Contributors

- *Self-aligned sequential lateral field non-uniformities over channel depth for high throughput dielectrophoretic cell deflection.*
  XuHai Huang, **Karina Torres-Castro**, Walter B. Varhue, Armita Salahi, Ahmed Rasin, Carlos Honrado, Audrey Brown, Jennifer Guler & Nathan S. Swami**.** ***Lab on a Chip,*** **RSC *(Lab on a Chip HOT Articles 2021--Inside front cover)***

- *High-throughput dynamical analysis of dielectrophoretic frequency dispersion of single cells based on deflected flow streamlines.*
  Karina Torres-Castro, Carlos Honrado, Walter B. Varhue, Vahid Farmehini & Nathan S. Swami. ***Analytical and Bioanalytical Chemistry,*** **Springer (2020),** ***Selected in Forefront cover***

- *Combined electrokinetic manipulations of pathogenic bacterial samples in low-cost fabricated dielectrophoretic devices*.
  Alejandro Martinez-Brenes, **Karina Torres-Castro**, Richard Marin-Benavides, Katherine Acuña-Umaña, Christopher Espinoza-Araya, Raquel Ramírez-Carranza, Gabriela González-Espinoza, Norman Rojas-Campos, Caterina Guzmán-Verri, Giovanni Sáenz-Arce & Leonardo Lesser-Rojas. **AIP Advances (2019)**

Conference Proceedings

- *Microfluidic Cooling for 3D-IC with 3D Printing Package.*
  Jun-Han Han, **Karina Torres-Castro**, Robert E. West, Walter B. Varhue, Nathan S. Swami & Mircea Stan. IEEE SOI-3D-Subthreshold Microelectronics Technology Unified (S3S)

- *Power and Thermal Modeling of In-3D-Memory Computing.*
  Jun-Han Han, Robert E. West, **Karina Torres-Castro**, Nathan S. Swami, Samira Khan & Mircea Stan. 2021 International Symposium on Devices, Circuits and Systems (ISDCS)

- *Thermal Analysis of Microfluidic cooling in Processing-in-3D-Stacked Memory.*
  Jun-Han Han, **Karina Torres-Castro**, Robert E. West, Nathan S. Swami & Mircea Stan. 2021 22nd International Conference on Thermal, Mechanical and Multi-Physics Simulation and Experiments in Microelectronics and Microsystems (EuroSimE)

Patent

- *On-chip microfluidic buffer swap of biological samples in-line with downstream dielectrophoresis and related method thereof.*
  N.S. SWAMI, X. Huang, **K. Torres-Castro**, W. Varhue
  US Patent App. 63/308,717

Bibliography

[1] Hywel Morgan and Nicolas G. Green. AC Electrokinetics: colloids and nanoparticles. Research Studies Press LTD., 2003.

[2] Ronald Pethig. Dielectrophoresis Theory, Methodology and Biological Applications. John Wiley & Sons, first edition, 2017.

[3] Henrik Bruus. Theoretical Microfluidics. Condensed matter physics. Oxford University Press, 2009.

[4] Nam-Trung Nguyen and Steven T. Wereley. Fundamentals and Applications of Microfluidics. Integrated Microsystems, 2006.

[5] Segré, G. and Silberberg, A. (1961) 'Radial particle displacements in Poiseuille flow of suspensions', Nature, 189(4760), pp. 209–210. doi: 10.1038/189209a0.

[6] Di Carlo, D. et al. (2007) 'Continuous inertial focusing, ordering, and separation of particles in microchannels.', Proceedings of the National Academy of Sciences of the United States of America, 104(48), pp. 18892–18897. doi: 10.1073/pnas.0704958104.

[7] Di Carlo, D. (2009) 'Inertial microfluidics.', Lab on a chip, 9(21), pp. 3038–3046. doi: 10.1039/b912547g.

[8] Jian Zhou, Prithviraj Mukherjee, Hua Gao, Qiyue Luan, and Ian Papautsky. Label-free microfluidic sorting of microparticles. APL Bioengineering, 3(4):041504, 2019.

[9] Axel Hochstetter, Rohan Vernekar, Robert H. Austin, Holger Becker, Jason P. Beech, Dmitry A. Fedosov, Gerhard Gompper, Sung-Cheol Kim, Joshua T. Smith, Gustavo Stolovitzky, Jonas O. Tegenfeldt, Benjamin H. Wunsch, Kerwin K. Zeming, Timm Krüger, and David W. Inglis. Deterministic Lateral Displacement: Challenges and Perspectives. ACS Nano, 14(9):10784– 10795, 2020.

[10] McGrath, J., Jimenez, M. and Bridle, H. (2014) 'D-eterministic lateral displacement for particle separation: a review', Lab Chip. Royal Society of Chemistry, 14(21), pp. 4139–4158. doi: 10.1039/C4LC00939H.

[11] H. K. Versteeg and W. Malalasekera. An Introduction to Computational Fluid Dynamics. Pearson Education Limited, 2007.

[12] Neda Azizipour, Rahi Avazpour, Derek H. Rosenzweig, Mohamad Sawan, and Abdellah Ajji. Evolution of Biochip Technology: A Review from Lab-on-a-Chip to Organ-on-a-Chip. Micro-machines, 2020.

[13] Darwin R. Reyes, Dimitri Lossifidis, Pierre-Alain Auroux, and Andreas Manz. Micro Total Analysis Systems. 1. Introduction, Theory, and Technology. Anal. Chem, 74(12):2623–2636, 2002.

[14] Karina Torres-Castro, Carlos Honrado, Walter B. Varhue, Vahid Farmehini, and Nathan S. Swami. High-Througput dynamical analysis of dielectrophoretic frequency dispersion of single cells based on deflected flow streamlines. Analytical and Bioanalytical Chemistry, 412:3847– 3857, 2020.

[15] Xuhai Huang, Karina Torres-Castro, Walter Varhue, Armita Salahi, Ahmed Rasin, Carlos Honrado, Audrey Brown, Jeniffer Guler and Nathan S. Swami. Self-aligned sequential lateral field non-uniformities over channel depth for high throughput dielectrophoretic cell deflection. Lab Chip, (5)21, 835-843, 2021

[16] Marie-Eve Myrand-Lapierre, Xiaoyan Deng, Richard R. Ang, Kerryn Matthews, Aline T. Santoso and Hongshen Ma. Multiplexed fluidic plunger mechanish for the measurement of red blood cell deformability. Lab Chip, 5(15), 159-167, 2015

[17] Walter B. Varhue, Linda Langman, Molly Kelly-Goss, Morgan Lataillade, Kenneth L. Brayman, Shayn Peirce-Cottler, and Nathan S. Swami. Deformability-based microfluidic separation of pancreatic islets from exocrine acinar tissue for transplant applications. Lab Chip, 17(21):3682– 3691, 2017.

[18] Yu Na Lee, Hye-Jin Yi, Yang Hee Kim, Song Lee, Jooyun Oh, Teruo Okano, In Kyong Shim and Song Cheol Kim. Evaluations of Multi-Layered Pancreatic Islets and Adipose-Derived Stem Cell Sheets Transplanted on Various Sites for Diabetes Treatment. Cells 2020, 9,1999, https://doi.org/10.3390/cells9091999

[19] Gael Galli and Maya Saleh. Immunometabolism of Macrophages in Bacterial Infections. Front.

Cell. Infect. Microbiol. 10:607650. doi:10.3389/fcimb.2020.607650

[20] Langer, R. In Islet transplantation: lessons learned since the Edmonton breakthrough, Transplantation proceedings, Elsevier: 2010; pp 1421-1424.

[21] Ricordi, C.; Strom, T. B., Clinical islet transplantation: advances and immunological challenges. Nature reviews. Immunology 2004, 4 (4), 259.

[22] Bottino, R.; Knoll, M. F.; Knoll, C. A.; Bertera, S.; Trucco, M. M., The future of islet transplantation is now. Frontiers in medicine 2018, 5, 202.

[23] Heuser, M.; Wolf, B.; Vollmar, B.; Menger, M. D., Exocrine contamination of isolated islets of Langerhans deteriorates the process of revascularization after free transplantation. Transplantation 2000, 69 (5), 756-761.

[24] Bowers, D.T., Song, W., Wang, L.H., Ma, M., Engineering the vasculature for islet transplantation. Acta Biomaterialia 2019, 95, pp.131-151.

[25] Coronel, M.M., Martin, K.E., Hunckler, M.D., Barber, G., O'Neill, E.B., Medina, J.D., Opri, E., McClain, C.A., Batra, L., Weaver, J.D., Lim, H.S., Qiu, P., Botchwey, E.A., Yolcu, E.S., Shirwan, H., Garcia, A.J. Immunotherapy via PD-L1–presenting biomaterials leads to long-term islet graft survival. Science Advances 2020, 6(35), eaba5573.

[26] Ichii, H.; Pileggi, A.; Molano, R. D.; Baidal, D. A.; Khan, A.; Kuroda, Y.; Inverardi, L.; Goss, J. A.; Alejandro, R.; Ricordi, C., Rescue purification maximizes the use of human islet preparations for transplantation. American journal of transplantation 2005, 5 (1), 21-30.

[27] Shapiro, A. J.; Pokrywczynska, M.; Ricordi, C., Clinical pancreatic islet transplantation. Nature Reviews Endocrinology 2017, 13 (5), 268-277.

[28] Ito, T.; Itakura, S.; Todorov, I.; Rawson, J.; Asari, S.; Shintaku, J.; Nair, I.; Ferreri, K.; Kandeel, F.; Mullen, Y., Mesenchymal stem cell and islet co-transplantation promotes graft revascularization and function. Transplantation 2010, 89 (12), 1438-1445.

[29] Yu, S. P.; Wei, Z.; Wei, L., Preconditioning strategy in stem cell transplantation therapy. Translational stroke research 2013, 4 (1), 76-88.

[30] Rackham, C. L.; Dhadda, P. K.; Chagastelles, P. C.; Simpson, S. J. S.; Dattani, A. A.; Bowe, J. E.; Jones, P. M.; King, A. J. F., Pre-culturing islets with mesenchymal stromal cells using a direct contact configuration is beneficial for transplantation outcome in diabetic mice. Cytotherapy 2013, 15 (4), 449-459.

[31] Kang, S.; Park, H. S.; Jo, A.; Hong, S. H.; Lee, H. N.; Lee, Y. Y.; Park, J. S.; Jung, H. S.; Chung, S. S.; Park, K. S., Endothelial progenitor cell cotransplantation enhances islet engraftment by rapid revascularization. Diabetes 2012, 61 (4), 866-876.

[32] Hayward, J. A.; Ellis, C. E.; Seeberger, K.; Lee, T.; Salama, B.; Mulet-Sierra, A.; Kuppan, P.; Adesida, A.; Korbutt, G. S., Cotransplantation of mesenchymal stem cells with neonatal porcine islets improve graft function in diabetic mice. Diabetes 2017, 66 (5), 1312-1321.

[33] Ohmura, Y.; Tanemura, M.; Kawaguchi, N.; Machida, T.; Tanida, T.; Deguchi, T.; Wada, H.; Kobayashi, S.; Marubashi, S.; Eguchi, H., Combined transplantation of pancreatic islets and adipose tissue-derived stem cells enhances the survival and insulin function of islet grafts in diabetic mice. Transplantation 2010, 90 (12), 1366-1373.

[34] Hematti, P.; Kim, J.; Stein, A. P.; Kaufman, D., Potential role of mesenchymal stromal cells in pancreatic islet transplantation. Transplantation reviews 2013, 27 (1), 21-29.

[35] Hubber, E. L.; Rackham, C. L.; Jones, P. M., Protecting islet functional viability using mesenchymal stromal cells. Stem cells translational medicine 2021.

[36] Nourmohammadzadeh, M., Xing, Y., Lee, J.W., Bochenek, M.A., Mendoza-Elias, J.E., McGarrigle, J.J., Marchese, E., Chun-Chieh, Y., Eddington, D.T., Oberholzer, J. and Wang, Y. A microfluidic array for real-time live-cell imaging of human and rodent pancreatic islets. Lab Chip 2016, 16(8), 1466-1472.

[37] Kin, T.; Senior, P.; O'Gorman, D.; Richer, B.; Salam, A.; Shapiro, A. M. J., Risk factors for islet loss during culture prior to transplantation. Transplant International 2008, 21 (11), 1029-1035.

[38] Stendahl, J. C.; Kaufman, D. B.; Stupp, S. I., Extracellular matrix in pancreatic islets: relevance to scaffold design and transplantation. Cell transplantation 2009, 18 (1), 1-12.

[39] Wang, R. N.; Paraskevas, S.; Rosenberg, L., Characterization of integrin expression in islets isolated from hamster, canine, porcine, and human pancreas. Journal of Histochemistry & Cytochemistry 1999, 47 (4), 499-506.

[40] Smink, A. M.; de Vos, P., Therapeutic strategies for modulating the extracellular matrix to improve pancreatic islet function and survival after transplantation. Current diabetes reports 2018, 18 (7), 1-7.

[41] Irving-Rodgers, H.; Choong, F. J.; Hummitzsch, K.; Parish, C.; Rodgers, R.; Simeonovic, C., Pancreatic islet basement membrane loss and remodeling after mouse islet isolation and transplantation: impact for allograft rejection. Cell transplantation 2014, 23 (1), 59-72.

[42] LaValley, D. J.; Reinhart-King, C. A., Matrix stiffening in the formation of blood vessels. Advances in Regenerative Biology 2014, 1 (1), 25247.

[43] Nyitray, C. E.; Chavez, M. G.; Desai, T. A., Compliant 3D microenvironment improves β-cell cluster insulin expression through mechanosensing and β-catenin signaling. Tissue Eng Pt A 2014, 20 (13-14), 1888-1895.

[44] Nagy, N.; de la Zerda, A.; Kaber, G.; Johnson, P. Y.; Hu, K. H.; Kratochvil, M. J.; Yadava, K.; Zhao, W.; Cui, Y.; Navarro, G., Hyaluronan content governs tissue stiffness in pancreatic islet inflammation. Journal of Biological Chemistry 2018, 293 (2), 567-578.

[45] Luan, Q.; Macaraniag, C.; Zhou, J.; Papautsky, I., Microfluidic systems for hydrodynamic trapping of cells and clusters. Biomicrofluidics 2020, 14 (3), 031502.

[46] Zheng, Y.; Nguyen, J.; Wei, Y.; Sun, Y., Recent advances in microfluidic techniques for single-cell biophysical characterization. Lab on a Chip 2013, 13 (13), 2464-2483.

[47] Qi, D.; Hoelzle, D.; Rowat, A., Probing single cells using flow in microfluidic devices. The European Physical Journal Special Topics 2012, 204 (1), 85-101.

[48] Myrand-Lapierre, M.-E.; Deng, X.; Ang, R. R.; Matthews, K.; Santoso, A. T.; Ma, H., Multiplexed fluidic plunger mechanism for the measurement of red blood cell deformability. Lab on a Chip 2015, 15 (1), 159-167.

[49] Zheng, Y.; Nguyen, J.; Wang, C.; Sun, Y., Electrical measurement of red blood cell deformability on a microfluidic device. Lab on a Chip 2013, 13 (16), 3275-3283.

[50] Otto, O.; Rosendahl, P.; Mietke, A.; Golfier, S.; Herold, C.; Klaue, D.; Girardo, S.; Pagliara, S.; Ekpenyong, A.; Jacobi, A., Real-time deformability cytometry: on-the-fly cell mechanical phenotyping. Nature methods 2015, 12 (3), 199-202.

[51] Varhue, W. B.; Langman, L.; Kelly-Goss, M.; Lataillade, M.; Brayman, K. L.; Peirce-Cottler, S.; Swami, N. S., Deformability-based microfluidic separation of pancreatic islets from exocrine acinar tissue for transplant applications. Lab on a Chip 2017, 17 (21), 3682-3691.

[52] Baraniak, P. R.; Cooke, M. T.; Saeed, R.; Kinney, M. A.; Fridley, K. M.; McDevitt, T. C., Stiffening of human mesenchymal stem cell spheroid microenvironments induced by incorporation of gelatin microparticles. Journal of the mechanical behavior of biomedical materials 2012, 11, 63-71.

[53] Wold, S.; Esbensen, K.; Gelaldi, P., Principal Component Analysis. Chemometrics and Laboratory Systems 1987, 2, 37-52.

[54] Ringnér, M., What is principal component analysis? Nat. Biotechnol. 2008, 28, 303-304.

[55] Perkins, T. J.; Swain, P. S., Strategies for cellular decision-making. Molecular systems biology 2009, 5 (1).

[56] Satija, R.; Shalek, A. K., Heterogeneity in immune responses: from populations to single cells. Trends in immunology 2014, 35 (5), 219-229.

[57] Jin, L.; Xiao, L.; Ding, M.; Pan, A.; Balian, G.; Sung, S.-S. J.; Li, X. J., Heterogeneous macrophages contribute to the pathology of disc herniation induced radiculopathy. The Spine Journal 2021.

[58] Klepárník, K.; Foret, F., Recent advances in the development of single cell analysis—A review. Analytica chimica acta 2013, 800, 12-21.

[59] Cros, J.; Raffenne, J.; Couvelard, A.; Poté, N., Tumor heterogeneity in pancreatic adenocarcinoma. Pathobiology 2018, 85 (1-2), 64-71.

[60] Wlodkowic, D.; Skommer, J.; Darzynkiewicz, Z., Cytometry in cell necrobiology revisited.

Recent advances and new vistas. Cytometry Part A 2010, 77 (7), 591-606.

[61] Grützkau, A.; Radbruch, A., Small but mighty: How the MACS®-technology based on nanosized superparamagnetic particles has helped to analyze the immune system within the last 20 years. Cytometry Part A 2010, 77 (7), 643-647.

[62] McGrath, J.; Honrado, C.; Moore, J.; Adair, S.; Varhue, W.; Salahi, A.; Farmehini, V.; Goudreau, B.; Nagdas, S.; Blais, E., Electrophysiology-based stratification of pancreatic tumorigenicity by label-free single-cell impedance cytometry. Analytica Chimica Acta 2020, 1101, 90-98.

[63] Yale, A. R.; Nourse, J. L.; Lee, K. R.; Ahmed, S. N.; Arulmoli, J.; Jiang, A. Y.; McDonnell, L. P.; Botten, G. A.; Lee, A. P.; Monuki, E. S., Cell surface N-glycans influence electrophysiological properties and fate potential of neural stem cells. Stem cell reports 2018, 11 (4), 869-882.

[64] Petchakup, C.; Tay, H. M.; Li, K. H. H.; Hou, H. W., Integrated inertial-impedance cytometry for rapid label-free leukocyte isolation and profiling of neutrophil extracellular traps (NETs). Lab on a Chip 2019, 19 (10), 1736-1746.

[65] Zhou, J.; Mukherjee, P.; Gao, H.; Luan, Q.; Papautsky, I., Label-free microfluidic sorting of microparticles. APL bioengineering 2019, 3 (4), 041504.

[66] Luan, Q.; Macaraniag, C.; Zhou, J.; Papautsky, I., Microfluidic systems for hydrodynamic trapping of cells and clusters. Biomicrofluidics 2020, 14 (3), 031502.

[67] Honrado, C.; Adair, S. J.; Moore, J. H.; Salahi, A.; Bauer, T. W.; Swami, N. S., Apoptotic Bodies in the Pancreatic Tumor Cell Culture Media Enable Label-Free Drug Sensitivity Assessment by Impedance Cytometry. Advanced Biology 2021, 2100438.

[68] Varhue, W. B.; Langman, L.; Kelly-Goss, M.; Lataillade, M.; Brayman, K. L.; Peirce-Cottler, S.; Swami, N. S., Deformability-based microfluidic separation of pancreatic islets from exocrine acinar tissue for transplant applications. Lab on a Chip 2017, 17 (21), 3682-3691.

[69] Rohani, A.; Moore, J. H.; Su, Y.-H.; Stagnaro, V.; Warren, C.; Swami, N. S., Single-cell electro-phenotyping for rapid assessment of Clostridium difficile heterogeneity under vancomycin treatment at sub-MIC (minimum inhibitory concentration) levels. Sensors and Actuators B: Chemical 2018,

276, 472-480.

[70] Lee, K. C.; Guck, J.; Goda, K.; Tsia, K. K., Toward deep biophysical cytometry: prospects and challenges. Trends in Biotechnology 2021.

[71] Yan, S.; Zhang, J.; Yuan, D.; Li, W., Hybrid microfluidics combined with active and passive approaches for continuous cell separation. Electrophoresis 2017, 38 (2), 238-249.

[72] Karabacak, N. M.; Spuhler, P. S.; Fachin, F.; Lim, E. J.; Pai, V.; Ozkumur, E.; Martel, J. M.; Kojic, N.; Smith, K.; Chen, P.-i., Microfluidic, marker-free isolation of circulating tumor cells from blood samples. Nature protocols 2014, 9 (3), 694-710.

[73] Fachin, F.; Spuhler, P.; Martel-Foley, J. M.; Edd, J. F.; Barber, T. A.; Walsh, J.; Karabacak, M.; Pai, V.; Yu, M.; Smith, K., Monolithic chip for high-throughput blood cell depletion to sort rare circulating tumor cells. Scientific reports 2017, 7 (1), 1-11.

[74] Hochstetter, A.; Vernekar, R.; Austin, R. H.; Becker, H.; Beech, J. P.; Fedosov, D. A.; Gompper, G.; Kim, S.-C.; Smith, J. T.; Stolovitzky, G., Deterministic lateral displacement: Challenges and perspectives. ACS nano 2020, 14 (9), 10784-10795.

[75] Huang, L. R.; Cox, E. C.; Austin, R. H.; Sturm, J. C., Continuous particle separation through deterministic lateral displacement. Science 2004, 304 (5673), 987-990.

[76] McGrath, J.; Jimenez, M.; Bridle, H., Deterministic lateral displacement for particle separation: a review. Lab on a Chip 2014, 14 (21), 4139-4158.

[77] Morton, K. J.; Loutherback, K.; Inglis, D. W.; Tsui, O. K.; Sturm, J. C.; Chou, S. Y.; Austin, R. H., Crossing microfluidic streamlines to lyse, label and wash cells. Lab on a Chip 2008, 8 (9), 1448-1453.

[78] Calero, V.; Garcia-Sanchez, P.; Honrado, C.; Ramos, A.; Morgan, H., AC electrokinetic biased deterministic lateral displacement for tunable particle separation. Lab on a Chip 2019, 19 (8), 1386-1396.

[79] Tatsumi, K.; Kawano, K.; Shintani, H.; Nakabe, K., Particle timing control and alignment in microchannel flow by applying periodic force control using dielectrophoretic force. Analytical

Chemistry 2019, 91 (10), 6462-6470.

[80] Cheung, K. C.; Di Berardino, M.; Schade-Kampmann, G.; Hebeisen, M.; Pierzchalski, A.; Bocsi, J.; Mittag, A.; Tárnok, A., Microfluidic impedance-based flow cytometry. Cytometry part A 2010, 77 (7), 648-666.

[81] Sun, T.; Morgan, H., Single-cell microfluidic impedance cytometry: a review. Microfluidics and Nanofluidics 2010, 8 (4), 423-443.

[82] Honrado, C.; Bisegna, P.; Swami, N. S.; Caselli, F., Single-cell microfluidic impedance cytometry: From raw signals to cell phenotypes using data analytics. Lab on a Chip 2021, 21 (1), 22-54.

[83] Mosser, D. M.; Edwards, J. P., Exploring the full spectrum of macrophage activation. Nature reviews immunology 2008, 8 (12), 958-969.

[84] Kawaguchi, S.; Yamashita, T.; Katahira, G.-i.; Yokozawa, H.; Torigoe, T.; Sato, N., Chemokine profile of herniated intervertebral discs infiltrated with monocytes and macrophages. Spine 2002, 27 (14), 1511-1516.

[85] Lu, Y.; Xue, Q.; Eisele, M. R.; Sulistijo, E. S.; Brower, K.; Han, L.; Amir, E.-a. D.; Pe'er, D.; Miller-Jensen, K.; Fan, R., Highly multiplexed profiling of single-cell effector functions reveals deep functional heterogeneity in response to pathogenic ligands. Proceedings of the National Academy of Sciences 2015, 112 (7), E607-E615.

[86] An, H.; Yu, Y.; Zhang, M.; Xu, H.; Qi, R.; Yan, X.; Liu, S.; Wang, W.; Guo, Z.; Guo, J., Involvement of ERK, p38 and NF-κB signal transduction in regulation of TLR2, TLR4 and TLR9 gene expression induced by lipopolysaccharide in mouse dendritic cells. Immunology 2002, 106 (1), 38-45.

[87] Vogel, D. Y.; Glim, J. E.; Stavenuiter, A. W.; Breur, M.; Heijnen, P.; Amor, S.; Dijkstra, C. D.; Beelen, R. H., Human macrophage polarization in vitro: maturation and activation methods compared. Immunobiology 2014, 219 (9), 695-703.

[88] Gordonov, S.; Hwang, M. K.; Wells, A.; Gertler, F. B.; Lauffenburger, D. A.; Bathe, M., Time

series modeling of live-cell shape dynamics for image-based phenotypic profiling. Integrative Biology 2016, 8 (1), 73-90.

[89] Jacobs, A.; Ignarro, L., LPS-induced expression of IFN-β mediates the timing of iNOS induction in RAW 264.7 macrophages. J Biol Chem 2001, 276, 47950-47957.

[90] Petchakup, C.; Hutchinson, P. E.; Tay, H. M.; Leong, S. Y.; Li, K. H. H.; Hou, H. W., Label-free quantitative lymphocyte activation profiling using microfluidic impedance cytometry. Sensors and Actuators B: Chemical 2021, 339, 129864.

[91] Inglis, D. W., Efficient microfluidic particle separation arrays. Applied Physics Letters 2009, 94 (1), 013510.

[92] Axel Hochstetter, Rohan Vernekar, Robert H. Austin, Holger Becker, Jason P. Beech, Dmitry A. Fedosov, Gerhard Gompper, Sung-Cheol Kim, Joshua T. Smith, Gustavo Stolovitzky, Jonas O. Tegenfeldt, Benjamin H. Wunsch, Kerwin K. Zeming, Timm Krüger, and David W. Inglis. Deterministic Lateral Displacement: Challenges and Perspectives. ACS Nano 2020 14 (9), 10784-10795. DOI: 10.1021/acsnano.0c05186

[93] Di Carlo, D.; Irimia, D.; Tompkins, R. G.; Toner, M., Continuous inertial focusing, ordering,and separation of particles in microchannels. Proceedings of the National Academy of Sciences 2007, 104 (48), 18892-18897.

[94] Di Carlo, D., Inertial microfluidics. Lab on a Chip 2009, 9 (21), 3038-3046.

[95] Spencer, D.; Morgan, H., Positional dependence of particles in microfludic impedance cytometry. Lab on a Chip 2011, 11 (7), 1234-1239.

[96] Errico, V.; De Ninno, A.; Bertani, F. R.; Businaro, L.; Bisegna, P.; Caselli, F., Mitigating positional dependence in coplanar electrode Coulter-type microfluidic devices. Sensors and Actuators B: Chemical 2017, 247, 580-586.

[97] Morgan, H.; Green, N.G., AC Electrokinetics: Colloids and nanoparticles. Research Studies Press LTD, UK, 2003.

[98] Martínez-Brenes, A.; Torres-Castro, K.; Marín-Benavides, M.; Acuña-Umaña, K.; Espinoza-

Araya, C.; Ramírez-Carranza, R.; González-Espinoza, G.; Rojas-Campos, N.; Guzmán-Verri, C.; Sáenz-Arce, G.; Lesser-Rojas, L., Combined electrokinetic manipulations of pathogenic bacterial simples in low cost fabricated dielectrophoretic devices. AIP Advances, 2019, 9(11), 115303.

[99] Perkins, T.J, P.S. Swain. Strategies for cellular decision-making. Mol Syst Biol. 2009;5(1):326

[100] Klepárník, K, F. Foret. Recent advances in the development of single cell analysis—A review. Anal Chim Acta. 2013;800:12-21.

[101] Adan, A., G. Alizada, Y. Kiraz, Y. Baran, A. Nalbant. Flow cytometry: basic principles and applications. Crit Rev Biotechnol. 2017;37(2):163-176.

[102] Grover, P., A. Cummins, T. Price, I. Roberts-Thomson, J. Hardingham. Circulating tumour cells: the evolving concept and the inadequacy of their enrichment by EpCAM-based methodology for basic and clinical cancer research. Ann Oncol. 2014;25(8):1506-1516.

[103] Mitchell, J.B., K. McIntosh, S. Zvonic, S. Garrett, Z.E. Floyd, A. Kloster, Y. Di Halvorsen, R.W. Storms, B. Goh, G. Kilroy. Immunophenotype of human adipose-derived cells: temporal changes in stromal-associated and stem cell–associated markers. Stem cells, 2006;24(2):376-385.

[104] Wlodkowic, D., J. Skommer, Z. Darzynkiewicz. Cytometry in cell necrobiology revisited. Recent advances and new vistas. Cytom A. 2010;77(7):591-606.

[105] Lee, W.C., H. Shi, Z. Poon, L.M. Nyan, T. Kaushik, G. Shivashankar, J.K. Chan, C.T. Lim, J. Han, K.J. Van Vliet. Multivariate biophysical markers predictive of mesenchymal stromal cell multipotency. PNAS. 2014;111(42):E4409-E4418.

[106] Gascoyne, P.R., S. Shim, J. Noshari, F.F. Becker, K. Stemke-Hale. Correlations between the dielectric properties and exterior morphology of cells revealed by dielectrophoretic field-flow fractionation. Electrophoresis. 2013;34(7):1042-1050.

[107] Moore, J.H., W.B. Varhue, Y.-H. Su, S.S. Linton, V. Farmehini, T.E. Fox, G.L. Matters, M. Kester, N.S. Swami. Conductance-Based Biophysical Distinction and Microfluidic Enrichment of Nanovesicles Derived from Pancreatic Tumor Cells of Varying Invasiveness. Anal Chem. 2019;91(16):10424-10431.

[108] Elitas, M., R. Martinez-Duarte, N. Dhar, J.D. McKinney, P. Renaud. Dielectrophoresis-based purification of antibiotic-treated bacterial subpopulations. Lab Chip. 2014;14(11):1850-1857.

[109] Su, Y.-H., A. Rohani, C.A. Warren, N.S. Swami. Tracking Inhibitory alterations during interstrain clostridium difficile interactions by monitoring cell envelope capacitance. ACS Infect Dis. 2016;2(8):544-551.

[110] Honrado, C., L. Ciuffreda, D. Spencer, L. Ranford-Cartwright, H. Morgan. Dielectric characterization of Plasmodium falciparum-infected red blood cells using microfluidic impedance cytometry. J R Soc Interface. 2018;15(147):20180416

[111] Gascoyne, P, S. Shim. Isolation of circulating tumor cells by dielectrophoresis. Cancers. 2014;6(1):545-579.

[112] Yale, A.R., J.L. Nourse, K.R. Lee, S.N. Ahmed, J. Arulmoli, A.Y. Jiang, L.P. McDonnell, G.A. Botten, A.P. Lee, E.S. Monuki. Cell surface N-glycans influence electrophysiological properties and fate potential of neural stem cells. Stem Cell Rep. 2018;11(4):869-882.

[113] Pohl, H.A, J.S. Crane. Dielectrophoresis of cells. Biophys J. 1971;11(9):711-727.

[114] Jones, T.B. Electromechanics of particles. Cambridge: Cambridge University Press; 2005.

[115] Morgan, H, N.G. Green. AC electrokinetics. Philadelphia: Research Studies Press; 2003.

[116] Fernandez, R.E., A. Rohani, V. Farmehini, N.S. Swami. Microbial analysis in dielectrophoretic microfluidic systems. Anal Chim Acta. 2017;966:11-33.

[117] Gagnon, Z.R. Cellular dielectrophoresis: applications to the characterization, manipulation, separation and patterning of cells. Electrophoresis. 2011;32(18):2466-2487.

[118] Wang, X.-B., J. Yang, Y. Huang, J. Vykoukal, F.F. Becker, P.R. Gascoyne. Cell separation by dielectrophoretic field-flow-fractionation. Anal Chem. 2000;72(4):832-839.

[119] Vahey, M.D, J. Voldman. High-throughput cell and particle characterization using isodielectric separation. Anal Chem. 2009; 81(7):2446-2455.

[120] Wang, L., J. Lu, S.A. Marchenko, E.S. Monuki, L.A. Flanagan, A.P. Lee. Dual frequency dielectrophoresis with interdigitated sidewall electrodes for microfluidic flow-through separation of

beads and cells. Electrophoresis. 2009;30(5):782-791.

[121] Lewpiriyawong, N., C. Yang, Y.C. Lam. Continuous sorting and separation of microparticles by size using AC dielectrophoresis in a PDMS microfluidic device with 3-D conducting PDMS composite electrodes. Electrophoresis. 2010;31(15):2622-2631.

[122] Lewpiriyawong, N., K. Kandaswamy, C. Yang, V. Ivanov, R. Stocker. Microfluidic characterization and continuous separation of cells and particles using conducting poly (dimethyl siloxane) electrode induced alternating current-dielectrophoresis. Anal Chem. 2011;83(24):9579-9585.

[123] Lapizco-Encinas, B.H, B.A. Simmons, E.B. Cummings, Y. Fintschenko. Insulator-based dielectrophoresis for the selective concentration and separation of live bacteria in water. Electrophoresis. 2004;25(10-11):1695-1704.

[124] Bhattacharya, S., T.-C. Chao, N. Ariyasinghe, Y. Ruiz, D. Lake, R. Ros, A. Ros. Selective trapping of single mammalian breast cancer cells by insulator-based dielectrophoresis. Anal Bioanal Chem. 2014; 406(7):1855-1865.

[125] Su, Y.-H., M. Tsegaye, W. Varhue, K.-T. Liao, L.S. Abebe, J.A. Smith, R.L. Guerrant, N.S. Swami. Quantitative dielectrophoretic tracking for characterization and separation of persistent subpopulations of Cryptosporidium parvum. Analyst. 2014;139(1):66-73.

[126] Farmehini, V., A. Rohani, Y.-H. Su, N.S. Swami. A wide-bandwidth power amplifier for frequency-selective insulator-based dielectrophoresis. Lab Chip. 2014;14(21):4183-4187.

[127] Huang, C.-T., C.-H. Weng, C.-P. Jen. Three-dimensional cellular focusing utilizing a combination of insulator-based and metallic dielectrophoresis. Biomicrofluidics. 2011;5(4):044101

[128] Pommer, M.S., Y. Zhang, N. Keerthi, D. Chen, J.A. Thomson, C.D. Meinhart, H.T. Soh. Dielectrophoretic separation of platelets from diluted whole blood in microfluidic channels. Electrophoresis. 2008; 29(6):1213-1218.

[129] Zhao, K., Larasati, B.P. Duncker, D. Li. Continuous Cell Characterization and Separation by Microfluidic Alternating Current Dielectrophoresis. Anal Chem. 2019;91(9):6304-6314.

[130] Piacentini, N., G. Mernier, R. Tornay, P. Renaud. Separation of platelets from other blood cells in continuous-flow by dielectrophoresis field-flow-fractionation. Biomicrofluidics. 2011;5(3):034122-034122-8

[131] Sun, M., P. Agarwal, S. Zhao, Y. Zhao, X. Lu, X. He. Continuous on-chip cell separation based on conductivity-induced dielectrophoresis with 3D self-assembled ionic liquid electrodes. Anal Chem. 2016; 88(16):8264-8271.

[132] Zhang, J., D. Yuan, Q. Zhao, S. Yan, S.-Y. Tang, S.H. Tan, J. Guo, H. Xia, N.-T. Nguyen, W. Li. Tunable particle separation in a hybrid dielectrophoresis (DEP)-inertial microfluidic device. Sens Actuators B Chem. 2018; 267:14-25.

[133] Rohani, A., J.H. Moore, J.A. Kashatus, H. Sesaki, D.F. Kashatus, N.S. Swami. Label-free quantification of intracellular mitochondrial dynamics using dielectrophoresis. Anal Chem. 2017;89(11):5757-5764.

[134] Su, Y.-H., C.A. Warren, R.L. Guerrant, N.S. Swami. Dielectrophoretic monitoring and interstrain separation of intact Clostridium difficile based on their S (Surface)-layers. Anal Chem. 2014; 86(21):10855-10863.

[135] Cottet, J., O. Fabregue, C. Berger, F. Buret, P. Renaud, M. Frénéa-Robin. MyDEP: a new computational tool for dielectric modeling of particles and cells. Biophys J. 2019;116(1):12-18.

[136] Wang, L., L.A. Flanagan, N.L. Jeon, E. Monuki, A.P. Lee. Dielectrophoresis switching with vertical sidewall electrodes for microfluidic flow cytometry. Lab Chip. 2007;7(9):1114-1120.

[137] Huang, X.; Torres-Castro, K.; Varhue, W.; Salahi, A.; Rasin, A.; Honrado, C.; Brown, A.; Guler, J.; Swami, N. S., Self-aligned sequential lateral field non-uniformities over channel depth for high throughput dielectrophoretic cell deflection. Lab on a Chip 2021, 21 (5), 835-843.

[138] Rohani, A.; Moore, J. H.; Kashatus, J. A.; Sesaki, H.; Kashatus, D. F.; Swami, N. S., Label-free quantification of intracellular mitochondrial dynamics using dielectrophoresis. Analytical chemistry, 2017, 89 (11), 5757-5764

[139] Mittal, N.; Rosenthal, A.; Voldman, J., nDEP microwells for single-cell patterning in

physiological media. Lab on a Chip, 2007, 7 (9), 1146-1153

[140] Teerapanich, P., Pugniere, M., Henriquet, C., Lin, Y.-L., Naillon, A., Joseph, P., Chou, C.-F., Leichle, T., Sensors and Actuators B: Chemical 2018, 274, 338-342.

[141] Wan, H., Yin, H., Sensors and Actuators B: Chemical 2018, 274, 682-688.

[142] Gossett, D.R., Tse, H.T.K., Dudani, J.S., Goda, K., Woods, T.A., Graves, S.W. and Di Carlo, D., Small 2012, 8(17), pp.2757-2764.

[143] Augustsson, P., Åberg, L.B., Swärd-Nilsson, A.M.K., Laurell, T., Microchimica Acta 2009, 164(3), pp.269-277.

[144] Ma, Z., Zhao, H., Shi, L., Yu, D., Guo, X., Electrophoresis 2021, 42, 1507–1515.

[145] Farmehini, V., Kiendzior, S., Landers, J.P. and Swami, N.S., ACS Sensors 2021, 6(10), 3765-3772.

[146] Huang, X., Torres-Castro, K., Varhue, W., Salahi, A., Rasin, A., Honrado, C., Brown, A., Guler, J., Swami, N. S., Lab Chip 2021, 21 (5), 835-843.

[147] Farmehini, V., Varhue, W.B., Salahi, A., Hyler, A. R., Čemažar, J., Davalos, R. V., Swami, N. S., IEEE Transactions on Biomedical Engineering 2019, 67 (6), 1664-1671.

[148] Farmehini, V., Rohani, A., Su, Y.-H., Swami, N. S., Lab Chip 2014, 14 (21), 4183-4187.

[149] Huang, X., Torres-Castro, K., Varhue, W., Salahi, A., Rasin, A., Honrado, C., Brown, A., Guler, J., Swami, N. S., Lab Chip 2021, 21 (5), 835-843.

Appendix

A.1 Confidence Ellipses for h-islets with ADSC co-culturing time points.

Confidence ellipses for controls and h-islets co-cultured with ADSC for 24h, 48h and 72h.

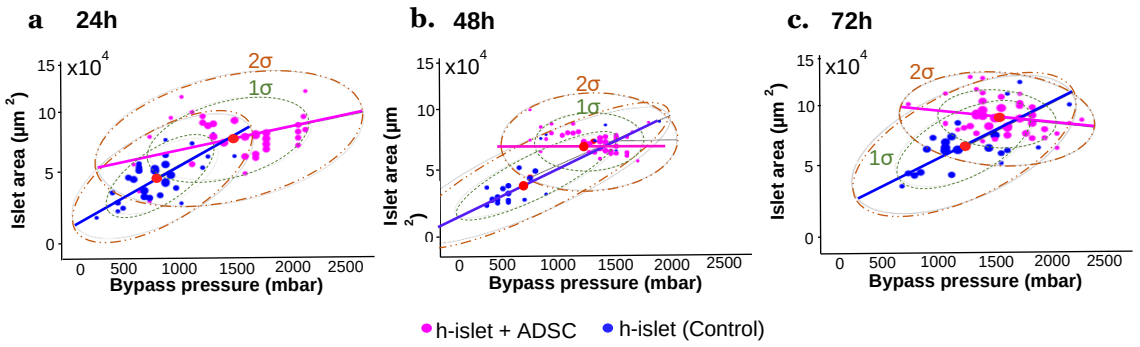

Figure A.1 Bypass pressure of individual co-cultured h-islet + ADSC and h-islet controls. (a) at 24h, (b) at 48h and (c) at 72h of co-culturing time.

A principal component analysis (PCA) was performed to correlate the bypass pressure needed to deform the h-islets through the device constriction, and their changes in area during the co-culturing time with ADSC (Fig. A.1). The h-islet aggregates were measured over the course of 3 days of co-culture with ADSCs at 24h, 48h and 72h time points. The confidence ellipses show how the controls maintain a positive slope across the 3 time points (as expected), whereas the h-islet + ADSC slope moves from a positive slope to an almost invariant slope (close to zero) in the 72h measurement. The respective slope at the 48h timepoint shows transition from a wider distribution of bypass pressures to a more compact distribution for the h-islet aggregates co-cultured with ADSCs. We attribute these alterations to the shape reorganization of the aggregates occurring during h-islet co-culture with ADSCs.

A.2 Quantifying shift in streamlines of RBCs based on DEP response

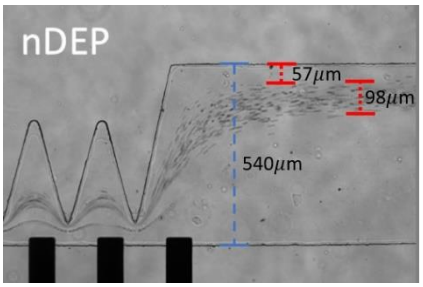

a. RBCs experiencing a negative DEP response

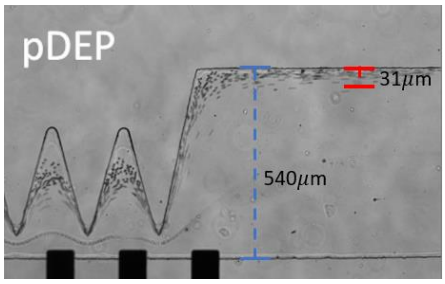

b. RBCs experiencing a positive DEP response

Fig. A.2: Quantitative limits are set for distance of RBC streamlines from the channel wall edge based on DEP response.

A.3 Validating experimental measurements on device based on membrane capacitance of RBCs:

The membrane capacitance values were calculated based on obtained crossover frequencies using [1,2]:

$$C_{mem} = \frac{\sigma_s}{2^{\frac{1}{2}} * \pi * r * f_{CO}} \qquad (1)$$

The membrane capacitance C_{mem} (mF/m^2) for the different media conductivities were calculated using Eq. 1 and are presented in Table A.3:

Table A.3 Membrane capacitance calculations of RBCs for the different media conductivity tested

Medium conductivity ($\mu S/cm$)	**Membrane capacitance - C_{mem} (mF/m^2)**
17	13
154	12
525	10
Mean	**11.7**
Standard deviation	**1.2**

Based on the calculation in Table A.3, the estimated C_{mem} of RBCs is 11.7 ± 1.2 mF/m^2.

A.4 Computation of the real part of the Clausius-Mossotti (CM(f)) for RBCs for the three chosen media conductivities to validate experimentally obtained crossover frequencies.

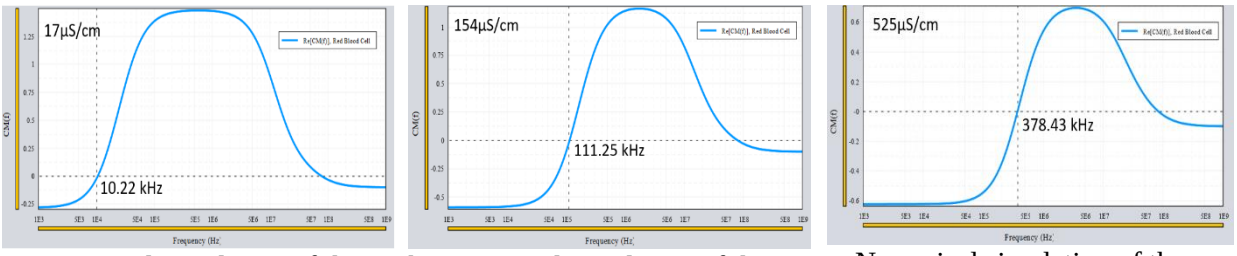

a. Numerical simulation of the CM(f) real part for RBCs at 17µS/cm. Theoretical crossover frequency ≈ 10.22 kHz

b. Numerical simulation of the CM(f) real part for RBCs at 154µS/cm. Theoretical crossover frequency ≈ 111.25 kHz

c. Numerical simulation of the CM(f) real part for RBCs at 525µS/cm. Theoretical crossover frequency ≈ 378.43 kHz

Fig. A.4 Real-part of the C-M factor computed based on established dielectric properties of RBCs to validate the crossover frequencies obtained for RBCs in the dynamic dielectrophoresis (Dy-DEP) device.

A.5 Experimental setup of the connected BSD device and the DEP one

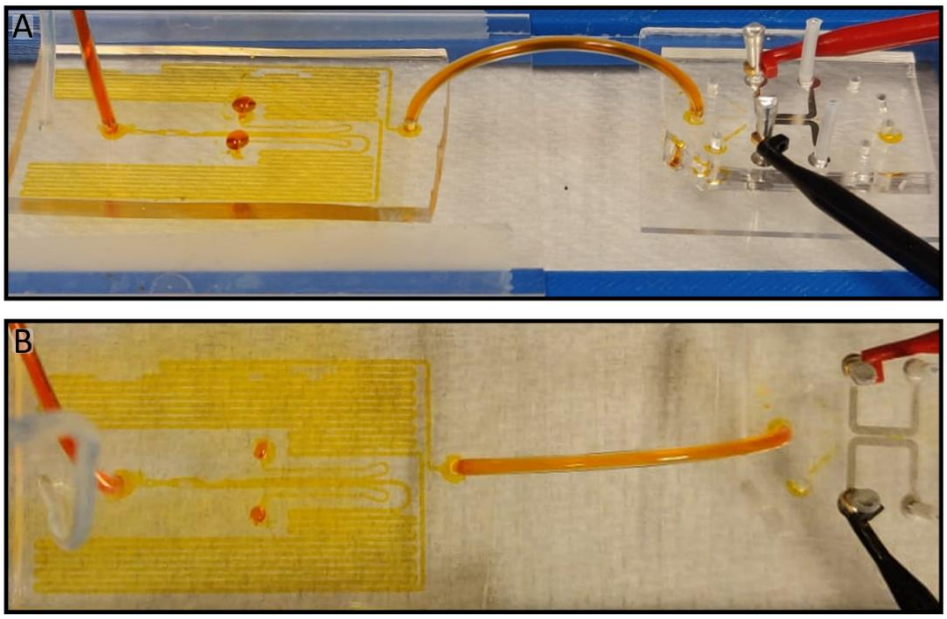

Fig. A.5 Side view (A) and top view (B) of the buffer swap device connected downstream with the DEP device. Food dye was used to highlight fluidic channels.